Reflection of diffuse light from two-dimensional rough surfaces & The light scattering properties of Gaussian-cosine correlated surfaces

Nils Petter Jørstad

June 15, 2021

MASTER THESIS

Department of Physics
Norwegian University of Science and Technology

Supervisor: Ingve Simonsen

Abstract

In this thesis the reflectance of 2D randomly rough surfaces illuminated by diffuse light, along with the scattering and polametric properties of Gaussian-cosine correlated surfaces, is studied through results obtained from rigorous numerical simulations. The simulations were based on a non-perturbational direct solution of the two-dimensional reduced Rayleigh equation for reflection.

The reflectivity and reflectance for both the directional and diffuse illumination of Gaussian correlated glass surfaces is presented and compared to previously obtained results for 1D surfaces. The reflectance for s-polarized, p-polarized and unpolarized diffuse illumination is found to either increase or decrease, depending on the nature of the surface roughness. Several differences are found in the behavior of the reflectance between 1D and 2D surfaces, depending on the characteristic length of the irregularities, when the roughness is systematically increased.

The full angular distribution of the mean differential reflection coefficient and the Mueller matrix for light scattering from both isotropic and anisotropic Gaussian-cosine correlated silver surfaces is presented and discussed in detail. These quantities describe the scattering and polarizing behavior of the randomly rough surfaces. The results are contrasted with the same quantities obtained for Gaussian correlated surfaces, which represent the classically studied example of a rough surface. It is observed that the Gaussian-cosine correlated surfaces have interesting scattering properties, such as an enhancement of p-polarized scattered light, a near specular suppression and a high reflectance. Some of the properties are shown to depend strongly on the characteristic size of the irregularities and the presence of surface plasmon polaritons. These findings could be of interest in various industries, such as the solar cell industry, where these properties are sought after.

Preface

This thesis is a part of two year Master of Science degree in physic at the Department of Physics of the Norwegian University of Science and Technology (NTNU, Trondheim). The thesis corresponds to 60 out of a total 120 ECTS credits and was carried out from August 2020 to June 2021. This project was carried out under the supervision of Professor Ingve Simonsen, who also proposed the research topic.

In this thesis the scattering of electromagnetic waves from two-dimensional randomly rough surfaces is studied through rigorous computer simulations. The computations were performed on resources provided by UNINETT Sigma2 - the National Infrastructure for High Performance Computing and data Storage in Norway, in addition to the NTNU IDUN/EPIC computing cluster [1].

This thesis is the culmination of a 5-year long journey to satisfy my curiosity and desire for understanding how the natural world works. It has been challenging yet educational and rewarding. Through many days of frustrations sprinkled with glowing moments of happiness, I have learned more than I could have imagined. However, if there is one thing I have learned, that I wish to single out, it is that I never want to stop being curious and that in some way or another I will continue my journey.

I would like to thank Ingve Simonsen for the opportunity to work on such a challenging and exciting project, which I have found both engaging and rewarding. I would also like to thank him for his excellent guidance, helpful advice and all the fruitful discussions we had.

Gratitude's are also extended to my lovely girlfriend Therese and my dear friend Victoria for proofreading and giving valuable feedback. Finally, many thanks go to my family and friends for support and encouragement.

Nils Petter Jørstad
June 15, 2021
Trondheim, Norway

Contents

List of Figures

List of Tables

1 Introduction

The light scattering properties of surfaces acting as interfaces between two media with different refractive indices, are frequently introduced through studying the Fresnel equations. These equations assume that the incident light can be described by plane-waves coming in from a single direction, and that the surface is perfectly flat. However, in nature these assumptions are not always valid. All surfaces display roughness at some length scale, and light interacting with surfaces is often coming from multiple sources and directions. Often these two assumptions yield good approximations, nonetheless, for very rough surfaces and strongly diffuse light they do not. Therefore, it is important that we have a good understanding of the interactions between diffuse light and the rough surfaces which surround our world.

It should be noted that what constitutes a rough or smooth surface is not strictly defined, since it is relative to the length scale it is observed at. Therefore, roughness is not an intrinsic property of a surface, it is instead characterized by the wavelength of the light interacting with it. If the rough features of a surface are on a scale much smaller than the wavelength of the incident light, then the surface can be considered smooth or approximately flat. If the roughness is on a scale much larger than the wavelength then the surface could still be considered smooth locally on the scale of the wavelength. However, if the characteristic roughness is on the same scale as the wavelength, the surface is considered to be rough. When the surface is smooth with respect to the wavelength of the incident light, the light is scattered coherently in the specular direction, i.e., mirror-like reflection. When the degree of surface roughness is increased, then a progressively larger fraction of the light will scatter into different non-specular directions. This scattering, is called diffuse scattering or incoherent scattering. When the surface is strongly rough then the coherent component can even be negligible compared to the incoherent one. Since the coherent component of the scattered light is trivially understood, it is the incoherent one which has gained the most attention in modern scientific literature [2][3][4][5].

Since roughness is predominantly the result of a random process, it is difficult to approach the problem in a analytical manner. Therefore, many researchers have turned to numerical tools and methods to study the light scattering properties of randomly rough surfaces. In this work two dimensional simulations based on solving the reduced Rayleigh equation (RRE) numerically were used to calculate the angular distribution of the scattered electric field. The numerical implementation of this approach is the same as the one presented in Ref. [6]. Various quantities of interest can be obtained from results, such as the mean differential reflection coefficient, the Mueller matrix, the reflectivity and the reflectance of the surface. The aim of this work is to study two special cases of light scattering from randomly rough surfaces.

In most research on this topic, the surface is illuminated by directional light. However, there are many cases where the light incident on a surface is diffuse, i.e., it comes from many directions with different phases. This problem has only been addressed for one dimensional surfaces [7], where several interesting trends manifest when the irregularities of the surface are systematically increased. The authors of Ref. [7] expect the 1D results to hold in the 2D case as well. Furthermore, they emphasize the importance of performing the calculations for two-dimensional surfaces, since such surfaces are more abundant in nature; in addition, there are many practical situations where the reflectance of a diffusely illuminated two-dimensional surface is of interest. In this work numerical results of the

reflectance for 2D surfaces illuminated by diffuse light will be presented, discussed and contrasted with what was found in the 1D case.

Randomly rough surfaces can be characterized by an auto-correlation function, which describes the degree of correlation between two points on the surface. Most rough surfaces profiles studied in literature are described by a Gaussian correlation function, since they are easier to perform calculations with and real surfaces have been experimentally shown to posses similar correlation. In this work the light scattering properties of surfaces characterized by a *Gaussian-cosine* correlation function [8], will be studied and compared to results for Gaussian-correlated surfaces. This correlation function is expected to yield interesting scattering results, since it is negative in certain intervals, i.e., points on the surface can be anti-correlated. In addition, certain polished optical surfaces have been shown to posses correlation which to some degree can be described by a Gaussian-cosine function [9].

The results shown in this work are relevant for various fields of science and engineering. The reflectance of diffusely illuminated rough surfaces is of interest in the paint and coating industry, where the reflectance is often calculated without taking the surface texture into account and has to be correcter later [10]. Another example is in medical imaging, where diffuse light reflected by tissue is incident onto a rough skin interface. The rapid developments in nano-technology over the past few decades has made it possible to design surfaces with a certain roughness in mind, for specific application where it is desired to take advantage of the light scattering properties. Designed rough surfaces have been studied in the solar cell industry, where it has been shown several times that a rough interfaces can increase the efficiency in thin photo voltaic cells [11]. In order to optimize these surfaces for potential applications, it is important to have a good fundamental understanding of how light interacts with them.

The next section, Sec. 2, introduces the theoretical framework required to describe the scattering of electromagnetic waves from randomly rough surfaces. This includes a statistical description of randomly rough surfaces, the origin of the reduced Rayleigh equation for reflection and the quantities one can obtain by solving it. In the following section, Sec. 3, the numerical approach to solving the RRE is explained along with the methods used to obtain quantifies of interest from the resulting reflection amplitudes. Then, the results are discussed and presented in Sec. 4. First, the results for Gaussian-correlated surfaces are presented; followed by, isotropic and anisotropic Gaussian-cosine correlated surfaces.

2 Theory

In this section the theoretical framework needed for evaluating scattering of electromagnetic waves, i.e. light, from randomly rough surfaces is introduced, along with the quantities we wish to study in this work.

First, we introduce the plane wave solution to Maxwell's equation. Then, the geometry of the physical system we consider is established, followed by the statistical description of a randomly rough surface. Next, the electric field in the vicinity of the surface is presented, along with the Rayleigh hypothesis and the boundary conditions the field has to satisfy when assuming the hypothesis is correct. Following, the reduced Rayleigh equation is introduced along with the mean differential reflection coefficient and the Mueller matrix elements. Afterwards, the expressions for the reflectivity and reflectance, for both incident plane waves and diffuse illumination are given. Finally, the conservation of the incident energy in the scattering process is discussed.

2.1 Electromagnetic waves

The Maxwell's equations have wave solutions and such solutions are thus called electromagnetic waves [12]. In a non-magnetic ($\mu = 1$), source free ($\boldsymbol{J} = 0$, $\rho = 0$), homogeneous, isotropic and dispersive medium the wave equation can be obtained in the following way. First, we take the curl of Faraday's law and substitute the curl of the magnetic field with Ampère's law, resulting in

$$\boldsymbol{\nabla} \times \boldsymbol{\nabla} \times \boldsymbol{E}(\boldsymbol{x}, t) = -\mu_0 \frac{\partial^2 \boldsymbol{D}(\boldsymbol{x}, t)}{\partial t^2}, \tag{1}$$

where μ_0 is the *vacuum permeability*. We assume that wave solutions for the field have a harmonic time dependence of $\exp(-i\omega t)$ with the angular frequency $\omega = 2\pi c/\lambda$, where λ is the corresponding wavelength in vacuum and c is the speed of light in vacuum. By taking the Fourier transform with respect to time on both sides and using the constitutive relation $\boldsymbol{D}(\boldsymbol{x}|\omega) = \varepsilon_0 \varepsilon(\omega) \boldsymbol{E}(\boldsymbol{x}|\omega)$, we obtain

$$\boldsymbol{\nabla} \times \boldsymbol{\nabla} \times \boldsymbol{E}(\boldsymbol{x}|\omega) = \mu_0 \varepsilon_0 \omega^2 \varepsilon(\omega) \boldsymbol{E}(\boldsymbol{x}|\omega), \tag{2}$$

where $\varepsilon(\omega)$ is the dielectric function of the medium the wave is propagating through and ε_0 is the *vacuum permittivity*. Applying the vector identity $\boldsymbol{\nabla} \times \boldsymbol{\nabla} \times \boldsymbol{E} = \boldsymbol{\nabla}(\boldsymbol{\nabla} \cdot \boldsymbol{E}) - \nabla^2 \boldsymbol{E}$ and Gauss's law $\boldsymbol{\nabla} \cdot \boldsymbol{D} = \varepsilon_0 \varepsilon(\omega) \boldsymbol{\nabla} \cdot \boldsymbol{E} = 0$, results in the *Helmholtz wave equation* for the electric field [13, p. 296]:

$$\left[\nabla^2 + \varepsilon(\omega) \frac{\omega^2}{c^2} \right] \boldsymbol{E}(\boldsymbol{x}|\omega) = 0, \tag{3}$$

where $c = 1/\sqrt{\mu_0 \varepsilon_0}$ was used. The Helmholtz equation has the following plane wave solution

$$\boldsymbol{E}(\boldsymbol{x}|\omega) = \boldsymbol{E}_0 \exp(i\boldsymbol{k} \cdot \boldsymbol{x}), \tag{4}$$

if and only if the dispersion relation given by

$$|\boldsymbol{k}|^2 = \varepsilon(\omega) \left(\frac{\omega}{c} \right)^2, \tag{5}$$

and $\boldsymbol{k} \cdot \boldsymbol{E}_0 = 0$ is satisfied. Here the vector $\boldsymbol{k} = k\hat{\boldsymbol{k}}$ is the wave vector, $\hat{\boldsymbol{k}}$ is the direction of propagation for the plane wave of the electric field. From here onwards, a caret "$\hat{}$" above

a vector denotes that it is a unit vector. Both the amplitude and direction of the field is described by the vector $\boldsymbol{E}_0$. The *polarization* of the electromagnetic wave is defined as the direction of the field. The full time dependent field is then given by

$$\boldsymbol{E}(\boldsymbol{x}, t) = \boldsymbol{E}(\boldsymbol{x}|\omega) \exp(-i\omega t). \tag{6}$$

When considering electromagnetic waves scattering from a surface, located in e.g. the x_1x_2-plane, it is convenient to separate wave vectors into two components, one parallel ($\boldsymbol{k}_\parallel$) and one perpendicular ($\boldsymbol{k}_\perp$) to the surface. The wave vector can then be written as

$$\boldsymbol{k} = \boldsymbol{k}_\parallel + \boldsymbol{k}_\perp. \tag{7}$$

With Eqs. (5) and (7) we can express the perpendicular component as a function of the parallel component, i.e.

$$\boldsymbol{k}_\perp = \pm\alpha_i(k_\parallel|\omega)\hat{\boldsymbol{x}}_{\boldsymbol{3}}, \tag{8}$$

where

$$\alpha_i(k_\parallel|\omega) = \sqrt{\varepsilon_i(\omega)\left(\frac{\omega}{c}\right)^2 - k_\parallel^2}, \ i = 1, 2\ . \tag{9}$$

Here i denoted the medium in which the wave is traveling, which is either above ($i = 1$) or below ($i = 2$) the surface. We can now rewrite the wave vector as

$$\boldsymbol{k} = \boldsymbol{k}_\parallel \pm \alpha_i(k_\parallel|\omega)\hat{\boldsymbol{x}}_3, \tag{10}$$

where $+$ and $-$ signify if the wave is propagating in the positive or negative $\hat{\boldsymbol{x}}_3$ direction, respectively. Note that as long as $\alpha_i(k_\parallel|\omega)$ given by Eq. (9) is real and $\boldsymbol{k} \cdot \boldsymbol{E}_0 = 0$, the dispersion relation (5) is satisfied and Eq. (4) describes a propagating plane wave. On the other hand, if $\alpha_i(k_\parallel|\omega)$ becomes purely imaginary, then Eq. (4) will be exponentially decaying in the x_3 direction and describing an *evanescent wave* [14, pp. 419–420].

2.2 Electromagnetic surface waves

Another solution of the wave equation for the electric field are so-called surface plasmon polaritons (SPPs). Shortly described, SPPs are electromagnetic wave modes confined to a surface separating a dielectric medium from a metal. SPPs can be excited by light incident onto such a surface, for futher details see [3, pp. 18–20]. The dispersion relation of SPPs reads [3, p. 19]

$$k_{spp}(\omega) = |\boldsymbol{k}_{spp}(\omega)| = \sqrt{\frac{\varepsilon_1(\omega)\varepsilon_2(\omega)}{\varepsilon_1(\omega) + \varepsilon_2(\omega)}}\frac{\omega}{c}, \tag{11}$$

where $k_{spp}(\omega)$ is the length of the parallel wave vector component of a SPP modes, $\varepsilon_1(\omega)$ and $\varepsilon_2(\omega)$ are the dielectric functions of the media the light is incident from and onto, respectively. The excitation of surface plasmon polarities requires $\varepsilon_1(\omega)$ and $\varepsilon_2(\omega)$ to have opposite signs so that $k_{spp} > \sqrt{\varepsilon_1}\omega/c$.

SPPs play an important role in the scattering of electromagnetic waves from randomly rough surfaces; for weakly rough surfaces their excitation is the reason behind various multiple scattering phenomena.

2.3 Scattering geometry

The scattering geometry we consider in this work is presented in Fig. 1, where two wave vectors $\boldsymbol{k}$, $\boldsymbol{q}$ are showing the direction of light incident on and scattered by a randomly rough surface.

The randomly rough surface is described by a surface profile function $x_3 = \zeta(\boldsymbol{x}_\parallel)$, which is a single-valued function of $\boldsymbol{x}_\parallel = (x_1, x_2, 0)$, that acts as the interface between two different media. We assume that the media in the two regions $x_3 > \zeta(\boldsymbol{x}_\parallel)$ and $x_3 < \zeta(\boldsymbol{x}_\parallel)$ are non-magnetic dielectrics or metals described by their individual dielectric functions $\varepsilon_1(\omega)$ and $\varepsilon_2(\omega)$, respectively.

The wave vector of the plane wave of light incident on the surface from the region $x_3 > \zeta(\boldsymbol{x}_\parallel)$ is denoted by $\boldsymbol{k}$. The component of $\boldsymbol{k}$ parallel to the x_1x_2-plane is defined by

$$\boldsymbol{k}_\parallel = \sqrt{\varepsilon_1}\frac{\omega}{c}\sin\theta_0\,(\cos\phi_0,\ \sin\phi_0,\ 0)\,, \tag{12}$$

where (θ_0, ϕ_0) are the polar and azimuthal angles of incidence, respectively. The plane spanned by $\boldsymbol{k}_\parallel$ and $\hat{\boldsymbol{x}}_3$ is called *the plane of incidence*, if the electric field is parallel to this plane the light is said to be *p-polarized*, conversely, if the field is perpendicular to the plane of incidence the light is *s-polarized*.

The wave vectors for the scattered light are denoted by $\boldsymbol{q}$, their lateral components are given by

$$\boldsymbol{q}_\parallel = \sqrt{\varepsilon_1}\frac{\omega}{c}\sin\theta_s\,(\cos\phi_s,\ \sin\phi_s,\ 0)\,, \tag{13}$$

where (θ_s, ϕ_s) are polar and azimuthal angles of scattering, respectively. Note that this relation is only correct for propagating scattered waves, i.e. $|\boldsymbol{q}_\parallel| < \sqrt{\varepsilon_1}\omega/c$. The positive directions for the angles of incidence and scattering are defined according to the convention given in Fig 1.

2.4 Statistical properties of randomly rough surfaces

We assume that the surface profile function $\zeta(\boldsymbol{x}_\parallel)$ constitutes a stationary, zero-mean, Gaussian random process. The choice of Gaussian height statistics is quite convenient, as moments up to any order can be related to the first two moments [15]. In addition, real surfaces are often found to posses Gaussian statistics [16, 17]. The process $x_3 = \zeta(\boldsymbol{x}_\parallel)$ is then completely characterized by

$$\begin{aligned} \langle\zeta(\boldsymbol{x}_\parallel)\rangle &= 0 \\ \langle\zeta(\boldsymbol{x}_\parallel)\zeta(\boldsymbol{x}'_\parallel)\rangle &= \delta^2 W(\boldsymbol{x}_\parallel - \boldsymbol{x}'_\parallel), \end{aligned} \tag{14}$$

where $\delta = \langle\zeta^2(\boldsymbol{x}_\parallel)\rangle^{1/2}$ is the root-mean-square (RMS) height of the surface and $W(\boldsymbol{x}_\parallel - \boldsymbol{x}'_\parallel)$ is the height auto-correlation function of the surface. The correlation function is normalized such that $W(\boldsymbol{0}) = 1$ and it can be shown that $-1 \leq W(\boldsymbol{x}_\parallel) \leq 1$. In the case of perfect correlation $W(\boldsymbol{x}_\parallel) = 1$, oppositely $W(\boldsymbol{x}_\parallel) = -1$ describes perfect anti-correlation. Here the angle brackets denote the spatial average over a large region. We will assume that the surface is *ergodic* [18]. Under this assumption, the spatial average is equal to the average over an ensemble of surface realizations. From here onwards the angle brackets denote an ensemble average, unless stated otherwise.

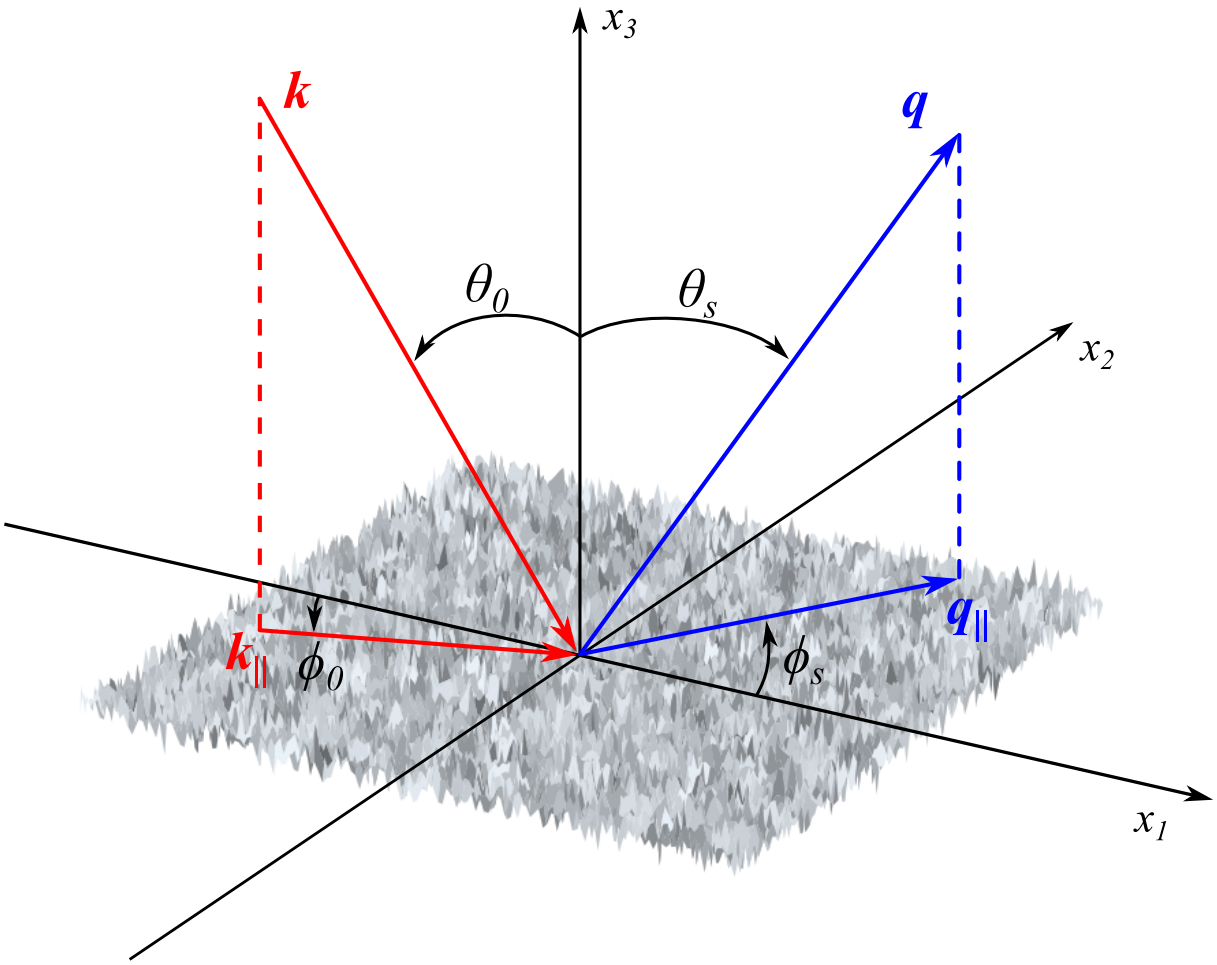

Figure 1: A drawing showing the scattering geometry considered in this work, along with the coordinate system used; the angles of incidence (θ_0, ϕ_0) and scattering (θ_s, ϕ_s); the incident and scattered wave vector $\boldsymbol{k}$ and $\boldsymbol{q}$; with their in-plane components $\boldsymbol{k}_{\parallel}$ and $\boldsymbol{q}_{\parallel}$, respectively.

According to the Wiener-Khinchin theorem [15], the power spectrum of the surface is given by the Fourier transform of the auto-correlation function, i.e.

$$g(\boldsymbol{k}_\parallel) = \int \mathrm{d}^2 x_\parallel W(\boldsymbol{x}_\parallel) \exp\left[-i\boldsymbol{k}_\parallel \cdot \boldsymbol{x}_\parallel\right]. \tag{15}$$

The power spectrum is a more useful quantity to use in calculations than the correlation function, since calculations involving the randomly rough surfaces are easier to perform in the Fourier domain. In this work we will be dealing with two forms of the power spectrum, the Gaussian and Gaussian-cosine power spectrum. The two-dimensional Gaussian power spectrum, which is often considered in literature, reads

$$g(\boldsymbol{k}_\parallel) = \pi a_1 a_2 \exp\left(-\frac{a_1^2 k_1^2 + a_2^2 k_2^2}{4}\right), \tag{16}$$

where a_1 and a_2 are the transverse correlation lengths in the x_1 and x_2 direction, respectively. The corresponding correlation function is given by

$$W(\boldsymbol{x}_\parallel) = \exp\left(-\frac{x_1^2}{a_1^2} - \frac{x_2^2}{a_2^2}\right). \tag{17}$$

In the isotropic case $a_1 = a_2 = a$. The isotropic two-dimensional Gaussian-cosine auto-correlation is defined as [8]

$$W(|\boldsymbol{x}_\parallel|) = \exp\left(-\frac{x_\parallel^2}{a^2}\right)\cos\left(\frac{x_\parallel}{b}\right), \tag{18}$$

where b is a positive parameter of dimension length. In the anisotropic case, we choose to define it as

$$W(\boldsymbol{x}_\parallel) = \exp\left(-\frac{x_1^2}{a_1^2} - \frac{x_2^2}{a_2^2}\right)\cos\left(\frac{x_\parallel}{b}\right). \tag{19}$$

The two-dimensional Fourier transforms of Eqs. (18) and (19) are not known analytically, and must therefore be evaluated numerically in order to obtain the power spectra.

2.5 Scattering theory

We consider an incident electromagnetic plane wave propagating towards the surface through the upper medium, with the electric field described by

$$\boldsymbol{E}_{inc}(\boldsymbol{x}|\omega) = \boldsymbol{E}_0(\boldsymbol{k}_\parallel)\exp\left(i\boldsymbol{k}_\parallel \cdot \boldsymbol{x}_\parallel - i\alpha_1(k_\parallel|\omega)x_3\right), \tag{20}$$

where the amplitude $\boldsymbol{E}_0(\boldsymbol{k}_\parallel)$ is given by

$$\boldsymbol{E}_0(\boldsymbol{k}_\parallel) = -\frac{c}{\sqrt{\varepsilon_1(\omega)}\omega}\left[\hat{\boldsymbol{k}}_\parallel \alpha_1(k_\parallel|\omega) + \hat{\boldsymbol{x}}_3 k_\parallel\right] E_{0p} + \left(\hat{\boldsymbol{x}}_3 \times \hat{\boldsymbol{k}}_\parallel\right) E_{0s}. \tag{21}$$

Here E_{0p} and E_{0s} denote the magnitude of the p-polarized and s-polarized components of the incoming electric field. If the field is entirely p-polarized then $E_{0s} = 0$ and vice versa.

A harmonic time dependence of $\exp[-i\omega t]$ has been assumed for all field expressions from here onward, but has not been indicated explicitly since future calculations are time

independent. It can easily be confirmed by the reader that the field (20) multiplied by $\exp[-i\omega t]$ satisfies the wave equation (3).

The asymptotic, far-field behavior of the field scattered by the randomly rough surface can be expressed as the integral over all possible scattering wave vectors $\boldsymbol{q}_\parallel$ of upwards propagating plane waves weighted by the scattered field amplitude $\boldsymbol{\mathcal{A}}(\boldsymbol{q}_\parallel)$,

$$\boldsymbol{E}_{sca}(\boldsymbol{x}|\omega) = \int \frac{\mathrm{d}^2 q_\parallel}{(2\pi)^2} \boldsymbol{\mathcal{A}}(\boldsymbol{q}_\parallel) \exp\left(i\boldsymbol{q}_\parallel \cdot \boldsymbol{x}_\parallel + i\alpha_1(q_\parallel|\omega)x_3\right). \tag{22}$$

The scattered field amplitude is given by

$$\boldsymbol{\mathcal{A}}(\boldsymbol{q}_\parallel) = \frac{c}{\sqrt{\varepsilon_1(\omega)}\omega}\left[\hat{\boldsymbol{q}}_\parallel \alpha_1(q_\parallel|\omega) - \hat{\boldsymbol{x}}_3 q_\parallel\right] \mathcal{A}_p(\boldsymbol{q}_\parallel) + \left(\hat{\boldsymbol{x}}_3 \times \hat{\boldsymbol{q}}_\parallel\right) \mathcal{A}_s(\boldsymbol{q}_\parallel). \tag{23}$$

Similarly to the incident field the scattered field is described by its p-polarized and s-polarized components $\mathcal{A}_p(\boldsymbol{q}_\parallel)$ and $\mathcal{A}_s(\boldsymbol{q}_\parallel)$, respectively.

We will assume that there is a linear relationship between the incident and scattered field amplitudes given by,

$$\mathcal{A}_\alpha\left(\boldsymbol{q}_\parallel\right) = \sum_{\beta=\mathrm{p,s}} R_{\alpha\beta}\left(\boldsymbol{q}_\parallel \mid \boldsymbol{k}_\parallel\right) E_{0\beta}\left(\boldsymbol{k}_\parallel\right), \tag{24}$$

where the subscript $\alpha = p, s$ denotes the polarization. Here $R_{\alpha\beta}(\boldsymbol{q}_\parallel \mid \boldsymbol{k}_\parallel)$ are unknown reflection amplitudes that we wish to determine, they describe how incident β-polarized light of lateral wave vector $\boldsymbol{k}_\parallel$ is scattered by the rough surface into α-polarized light of lateral wave vector $\boldsymbol{q}_\parallel$. Scattered light with the same polarization as the incident light is said to be *co-polarized*, while light which is polarized oppositely with respect to the incident light is said to be *cross-polarized*. Note that the integral in the expression for the scattered field (22) is over the whole spectrum of $\boldsymbol{q}_\parallel$, which includes contributions from both *propagating* and *evanescent* modes.

The total electromagnetic field above the maximum height of the surface $x_3 > \max\zeta(\boldsymbol{x}_\parallel)$ can then be expressed as the sum of the incident field and the scattered field,

$$\boldsymbol{E}^+(\boldsymbol{x}|\omega) = \boldsymbol{E}_{inc}(\boldsymbol{x}|\omega) + \boldsymbol{E}_{sca}(\boldsymbol{x}|\omega). \tag{25}$$

Similarly the asymptotic, far-field behavior of the transmitted field in the second region $x_3 < \min\zeta(\boldsymbol{x}_\parallel)$ can be written as

$$\boldsymbol{E}^-(\boldsymbol{x}|\omega) = \int \frac{\mathrm{d}^2 p_\parallel}{(2\pi)^2} \boldsymbol{\mathcal{B}}(\boldsymbol{p}_\parallel) \exp\left(i\boldsymbol{p}_\parallel \cdot \boldsymbol{x}_\parallel - i\alpha_2(p_\parallel|\omega)x_3\right). \tag{26}$$

Here $\boldsymbol{p}_\parallel$ is the lateral component of the wave vector of a transmitted plane wave and the field amplitude is given by

$$\boldsymbol{\mathcal{B}}(\boldsymbol{p}_\parallel) = -\frac{c}{\sqrt{\varepsilon_2(\omega)}\omega}\left[\hat{\boldsymbol{p}}_\parallel \alpha_2(p_\parallel|\omega) + \hat{\boldsymbol{x}}_3 p_\parallel\right] \mathcal{B}_p(\boldsymbol{q}_\parallel) + \left(\hat{\boldsymbol{x}}_3 \times \hat{\boldsymbol{p}}_\parallel\right) \mathcal{B}_s(\boldsymbol{q}_\parallel). \tag{27}$$

The p- and s-polarized components of the transmitted electric field have the following linear relation with the incident field ($\alpha = p, s$)

$$\mathcal{B}_\alpha\left(\boldsymbol{q}_\parallel\right) = \sum_{\beta=\mathrm{p,s}} T_{\alpha\beta}\left(\boldsymbol{p}_\parallel \mid \boldsymbol{k}_\parallel\right) E_{0\beta}\left(\boldsymbol{k}_\parallel\right), \tag{28}$$

where $T_{\alpha\beta}(\boldsymbol{p}_\parallel \mid \boldsymbol{k}_\parallel)$ are unknown transmission amplitudes analogous to the reflection amplitudes in (24), describing how β-polarized incident light with wave vector $\boldsymbol{k}$ is transmitted into α-polarized light of wave vector $\boldsymbol{p}$. Again, the integration is taken over the whole spectrum.

For a complete description of the fields, the time dependence can be reintroduced by multiplying (25) and (26) with $\exp[-i\omega t]$.

2.6 The Rayleigh hypothesis

Equations (25) and (26) describe the electric field above the maximum height and below the minimum height of the surface, respectively. In order to determine the reflection and transmission amplitudes, one has to account for the boundary conditions for the field at $x_3 = \zeta(\boldsymbol{x}_\parallel)$. The form of the field in the surface region $\min \zeta(\boldsymbol{x}_\parallel) < \zeta(\boldsymbol{x}_\parallel) < \max \zeta(\boldsymbol{x}_\parallel)$ is however not known as the above mentioned forms are generally not valid in this region, since downwards propagating scattered waves and upwards propagating transmitted waves are not accounted for.

If the surface is not too rough and the local slopes are sufficiently small, the unaccounted for modes should then have a less significant contribution to the scattering process. The asymptotic expansions of the field above and below the surface region should then serve as a good approximation for the field in the surface region. Under this assumption the boundary conditions for the field at the interface $\zeta(\boldsymbol{x}_\parallel)$ can be solved exactly. This assumption is known as the *Rayleigh Hypothesis* [19] and was first postulated by Lord Rayleigh when he was studying scattering of acoustic waves from sinusoidal surfaces at the end of the 19th century [20].

It is however difficult to quantify the limit of roughness where the approximation is no longer valid. For a one-dimensional sinusoidal surface $x_3 = \zeta_0 \sin(\Lambda x_1)$, the hypothesis is formally valid when $\zeta_0 \Lambda < 0.448$ [21]. For randomly rough surfaces there is no known formal criterion of validity, however, there seems to be a consensus in the literature for the following criterion [22]

$$\frac{\delta}{a} \ll 1, \tag{29}$$

where a and δ is the correlation length and rms-height of the random surface, respectively.

2.7 Boundary conditions

Assuming the Rayleigh hypothesis is valid, the total field in the region $\min \zeta(\boldsymbol{x}_\parallel) < \zeta(\boldsymbol{x}_\parallel) < \max \zeta(\boldsymbol{x}_\parallel)$ can be expressed by the asymptotic forms of the field above and below the surface, given by equations (25) and (26). These equations are then required to satisfy the usual boundary conditions for the transition of the field across the interface between the two dielectric media [13, p. 304].

The boundary conditions needed to be satisfied at $x_3 = \zeta(\boldsymbol{x}_\parallel)$, consist of the continuity of the normal component of the magnetic flux density and electric displacement, in addition to the continuity of the tangential components of the electric and magnetic field. Assuming non magnetic media ($\mu = 1$) above and below the interface, no surface current and no surface charge, the boundary conditions expressed with the electric field $\boldsymbol{E}$ and

the magnetic field $\boldsymbol{H}$, read

$$\hat{\boldsymbol{n}} \cdot \left[\boldsymbol{H}^{-}(\boldsymbol{x}|\omega) - \boldsymbol{H}^{+}(\boldsymbol{x}|\omega)\right]_{x_3=\zeta(\boldsymbol{x}_\parallel)} = 0, \tag{30a}$$

$$\hat{\boldsymbol{n}} \cdot \left[\varepsilon_2 \boldsymbol{E}^{-}(\boldsymbol{x}|\omega) - \varepsilon_1 \boldsymbol{E}^{+}(\boldsymbol{x}|\omega)\right]_{x_3=\zeta(\boldsymbol{x}_\parallel)} = 0, \tag{30b}$$

$$\hat{\boldsymbol{n}} \times \left[\boldsymbol{E}^{-}(\boldsymbol{x}|\omega) - \boldsymbol{E}^{+}(\boldsymbol{x}|\omega)\right]_{x_3=\zeta(\boldsymbol{x}_\parallel)} = 0, \tag{30c}$$

$$\hat{\boldsymbol{n}} \times \left[\boldsymbol{H}^{-}(\boldsymbol{x}|\omega) - \boldsymbol{H}^{+}(\boldsymbol{x}|\omega)\right]_{x_3=\zeta(\boldsymbol{x}_\parallel)} = 0. \tag{30d}$$

The magnetic fields below and above the surface are given by

$$\boldsymbol{H}^{-}(\boldsymbol{x}|\omega) = \frac{1}{\mu_0 \omega} \int \frac{\mathrm{d}^2 p_\parallel}{(2\pi)^2} \left[\boldsymbol{p}_\parallel - \alpha_2(p_\parallel|\omega)\hat{\boldsymbol{x}}_{\boldsymbol{3}}\right] \times \boldsymbol{\mathcal{B}}(\boldsymbol{p}_\parallel) \times \exp\left(i\boldsymbol{p}_\parallel \cdot \boldsymbol{x}_\parallel - i\alpha_2(p_\parallel|\omega)x_3\right) \tag{31}$$

and

$$\begin{aligned} \boldsymbol{H}^{+}(\boldsymbol{x}|\omega) = \frac{1}{\mu_0 \omega} \Bigg[& \left[\boldsymbol{k}_\parallel - \alpha_1(k_\parallel|\omega)\hat{\boldsymbol{x}}_{\boldsymbol{3}}\right] \times \boldsymbol{E}_{inc}(\boldsymbol{x}|\omega) \\ & + \int \frac{\mathrm{d}^2 q_\parallel}{(2\pi)^2} \left[\boldsymbol{q}_\parallel + \alpha_1(q_\parallel|\omega)\hat{\boldsymbol{x}}_{\boldsymbol{3}}\right] \times \boldsymbol{\mathcal{A}}(\boldsymbol{q}_\parallel) \exp\left(i\boldsymbol{q}_\parallel \cdot \boldsymbol{x}_\parallel + i\alpha_1(q_\parallel|\omega)x_3\right) \Bigg], \end{aligned} \tag{32}$$

respectively. Here $\hat{\boldsymbol{n}} \equiv \hat{\boldsymbol{n}}(\boldsymbol{x}_\parallel)$ is a unit vector normal to the surface profile at every point $\boldsymbol{x}_\parallel$, directed from medium 2 to 1, given by

$$\hat{\boldsymbol{n}}(\boldsymbol{x}_\parallel) = \frac{-\frac{\partial\zeta(\boldsymbol{x}_\parallel)}{\partial x_1}\hat{\boldsymbol{x}}_1 - \frac{\partial\zeta(\boldsymbol{x}_\parallel)}{\partial x_2}\hat{\boldsymbol{x}}_2 + \hat{\boldsymbol{x}}_3}{\sqrt{\left(\frac{\partial\zeta(\boldsymbol{x}_\parallel)}{\partial x_1}\right)^2 + \left(\frac{\partial\zeta(\boldsymbol{x}_\parallel)}{\partial x_2}\right)^2 + 1}}. \tag{33}$$

2.8 The reduced Rayleigh equation

The reflection amplitudes $R_{\alpha\beta}$ are obtained by solving the *reduced Rayleigh equation* (RRE) for reflection, the derivation of this equation is shortly described below. By using the Rayleigh hypothesis and applying the boundary conditions (30) for the field above (25) and below (26), one generates a set of inhomogeneous integral equations called the *Rayleigh equations*. These equations couple the unknown reflection and transmission amplitudes to each other, they are the starting point for deriving the reduced Rayleigh equation for both reflection and transmission.

The goal is to uncouple these equations in order to obtain an equation involving only the reflection amplitudes $R_{\alpha\beta}$. This is accomplished by using the *extinction theorem* [23] to eliminate the field below the interface in the Rayleigh equations, resulting in an integral equation containing only the reflection amplitudes. Similarly one can derive the RRE for transmission, where one eliminates the scattered field instead. The derivation of the RRE for a single rough interface was shown by Brown in 1984 [24]; where the details of the derivation are presented.

The resulting RRE for reflection, for a randomly rough, penetrable two-dimensional surface, reads

$$\int \frac{\mathrm{d}^2 q_\parallel}{(2\pi)^2} \boldsymbol{M}^{+}(\boldsymbol{p}_\parallel|\boldsymbol{q}_\parallel)\boldsymbol{R}(\boldsymbol{q}_\parallel|\boldsymbol{k}_\parallel) = -\boldsymbol{M}^{-}(\boldsymbol{p}_\parallel|\boldsymbol{k}_\parallel), \tag{34}$$

where the reflection amplitudes are the elements of the 2×2 matrix given by

$$\boldsymbol{R}(\boldsymbol{q}_\parallel|\boldsymbol{k}_\parallel) = \begin{pmatrix} R_{pp}(\boldsymbol{q}_\parallel|\boldsymbol{k}_\parallel) & R_{ps}(\boldsymbol{q}_\parallel|\boldsymbol{k}_\parallel) \\ R_{sp}(\boldsymbol{q}_\parallel|\boldsymbol{k}_\parallel) & R_{ss}(\boldsymbol{q}_\parallel|\boldsymbol{k}_\parallel) \end{pmatrix}, \tag{35}$$

and

$$\begin{aligned} \boldsymbol{M}^{\pm}(\boldsymbol{p}_\parallel|\boldsymbol{q}_\parallel) = & \frac{I\left(\alpha_2\left(p_\parallel\right) \mp \alpha_1\left(q_\parallel\right)|\boldsymbol{p}_\parallel - \boldsymbol{q}_\parallel\right)}{\alpha_2\left(p_\parallel\right) \mp \alpha_1\left(q_\parallel\right)} \\ & \times \begin{pmatrix} p_\parallel q_\parallel \pm \alpha_2(p_\parallel|\omega)\hat{\boldsymbol{p}}_\parallel \cdot \hat{\boldsymbol{q}}_\parallel \alpha_1(q_\parallel|\omega) & -\frac{\omega}{c}\alpha_2(p_\parallel|\omega)[\hat{\boldsymbol{p}}_\parallel \times \hat{\boldsymbol{q}}_\parallel]_3 \\ \pm\frac{\omega}{c}\alpha_1(q_\parallel|\omega)[\hat{\boldsymbol{p}}_\parallel \times \hat{\boldsymbol{q}}_\parallel]_3 & \frac{\omega^2}{c^2}\hat{\boldsymbol{p}}_\parallel \cdot \hat{\boldsymbol{q}}_\parallel \end{pmatrix}, \end{aligned} \tag{36}$$

with

$$I(\gamma \mid \boldsymbol{Q}_\parallel) = \int \mathrm{d}^2 x_\parallel \exp\left[-\mathrm{i}\gamma\zeta\left(\boldsymbol{x}_\parallel\right)\right] \exp(-\mathrm{i}\boldsymbol{Q}_\parallel \cdot \boldsymbol{x}_\parallel). \tag{37}$$

The integral in Eq. (34) is taken over the whole spectrum of lateral wave vectors $\boldsymbol{q}_\parallel$ and the integral in Eq. (37) is taken over the whole x_1x_2-plane.

The RRE is the starting point for many perturbation theories, however, non-perturbative results can be obtained by solving it directly using numerical techniques.

2.9 The mean differential reflection coefficient

The reflection amplitudes $R_{\alpha\beta}$ can now be determined by solving the RRE for reflection (34), which allows us to fully specify the field above the surface. The ultimate objective is to be able to compare the results with experiments, however, the reflection amplitudes are not directly measurable in experiments.

A more convenient quantity that is accessible in experiments and fully specifies the scattering, is the *mean differential reflection coefficient* (MDRC). The MDRC is defined as the fraction of the incident power scattered by the surface into the solid angle $d\Omega_s$ about the scattering angles (θ_s, ϕ_s), averaged over an ensemble of surface realizations. For an incident plane wave the MDRC is given by [5]

$$\left\langle \frac{\partial R_{\alpha\beta}}{\partial \Omega_s} \right\rangle = \frac{\varepsilon_1}{S} \frac{\omega^2}{4\pi^2 c^2} \frac{\cos^2\theta_s}{\cos\theta_0} \left\langle \left| R_{\alpha\beta}\left(\boldsymbol{q}_\parallel \mid \boldsymbol{k}_\parallel\right)\right|^2 \right\rangle, \tag{38}$$

where $S = L^2$ and L is the length and width of the quadratic surface realizations we average over.

If the reflection amplitude $R_{\alpha\beta}(\boldsymbol{q}_\parallel \mid \boldsymbol{k}_\parallel)$ is expressed as the sum of the mean and the fluctuation from its mean

$$R_{\alpha\beta}\left(\boldsymbol{q}_\parallel \mid \boldsymbol{k}_\parallel\right) = \left\langle R_{\alpha\beta}\left(\boldsymbol{q}_\parallel \mid \boldsymbol{k}_\parallel\right)\right\rangle + \left[R_{\alpha\beta}\left(\boldsymbol{q}_\parallel \mid \boldsymbol{k}_\parallel\right) - \left\langle R_{\alpha\beta}\left(\boldsymbol{q}_\parallel \mid \boldsymbol{k}_\parallel\right)\right\rangle\right], \tag{39}$$

then the MDRC can be separated into the contribution from the coherent (specular) and the incoherent (diffuse) component of the scattered light, i.e.

$$\left\langle \frac{\partial R_{\alpha\beta}}{\partial \Omega_s} \right\rangle = \left\langle \frac{\partial R_{\alpha\beta}}{\partial \Omega_s} \right\rangle_{\mathrm{coh}} + \left\langle \frac{\partial R_{\alpha\beta}}{\partial \Omega_s} \right\rangle_{\mathrm{incoh}}, \tag{40}$$

where

$$\left\langle \frac{\partial R_{\alpha\beta}}{\partial \Omega_s} \right\rangle_{\mathrm{coh}} = \frac{\varepsilon_1}{S} \frac{\omega^2}{4\pi^2 c^2} \frac{\cos^2\theta_s}{\cos\theta_0} \left|\left\langle R_{\alpha\beta}\left(\boldsymbol{q}_\parallel \mid \boldsymbol{k}_\parallel\right)\right\rangle\right|^2 \tag{41}$$

and

$$\left\langle \frac{\partial R_{\alpha\beta}}{\partial \Omega_s} \right\rangle_{\text{incoh}} = \frac{\varepsilon_1}{S} \frac{\omega^2}{4\pi^2 c^2} \frac{\cos^2 \theta_s}{\cos \theta_0} \times \left[\left\langle \left| R_{\alpha\beta} \left(\boldsymbol{q}_{\parallel} \mid \boldsymbol{k}_{\parallel} \right) \right|^2 \right\rangle - \left| \left\langle R_{\alpha\beta} \left(\boldsymbol{q}_{\parallel} \mid \boldsymbol{k}_{\parallel} \right) \right\rangle \right|^2 \right]. \tag{42}$$

Similarly the transmitted field can can be specified by the experimentally measurable *mean differential transmission coefficient* (MDTC), which can be obtained in a analogous way to the MDRC, see [25] for details.

Both coherent (specular) and incoherent (diffuse) scattering processes will occur when studying scattering from rough surfaces. For surfaces with roughness parameters which satisfy the validity criterion for the Rayleigh hypothesis (29), the coherent part which consists of the majority of specular scattering will dominate. With this in mind it is often found useful to separate these components when studying the MDRC, even though such separation is not possible to perform experimentally.

2.10 The Mueller matrix elements

Another measurable quantity that is of interest is the Mueller matrix of the randomly rough surface. The Mueller matrix contains a complete description of the polarization response of the rough surface, including co- and cross-polarization for any polarization state of the incident light. The polarization of the incident light can be described by the Stokes vector defined by [26]

$$\boldsymbol{S} = \begin{bmatrix} I \\ Q \\ U \\ V \end{bmatrix} = \begin{bmatrix} |E_p|^2 + |E_s|^2 \\ |E_p|^2 - |E_s|^2 \\ 2Re(E_p E_s^*) \\ 2Im(E_p E_s^*) \end{bmatrix}. \tag{43}$$

Here and in the rest of this work "$*$" denotes the complex conjugate. The elements of the Stokes vector are called the Stokes parameters. The first parameter I describes the intensity of the incoming light, the second Q describes the degree of vertical (p) and horizontal (s) polarization, U describes the degree of 45° and −45° polarization, while V describes the degree of left and right circular polarization. For example, if the Stokes vector is normalized with respect to the intensity, purely horizontally or vertically polarized light gives $Q = 1$ or $Q = -1$, respectively. Likewise, the same is true for other types of polarizations. Multiplying a Stokes vector of the incident light with the Mueller Matrix of the surface for a scattering direction described by $\boldsymbol{q}_{\parallel}$, results in a Stokes vector describing the polarization of the light scattered in that direction.

The reflection amplitudes that appear in in Eq. (24) are central for determining the

16 elements of the 4×4 Mueller matrix. The elements are given by [27]

$$
\begin{aligned}
M_{11} &= C(|R_{pp}|^2 + |R_{sp}|^2 + |R_{ps}|^2 + |R_{ss}|^2), \\
M_{12} &= C(|R_{pp}|^2 + |R_{sp}|^2 - |R_{ps}|^2 - |R_{ss}|^2), \\
M_{13} &= C(R_{pp}R_{ps}^* + R_{sp}R_{ss}^* + R_{ps}R_{pp}^* + R_{ss}R_{sp}^*), \\
M_{14} &= iC(R_{pp}R_{ps}^* + R_{sp}R_{ss}^* - R_{ps}R_{pp}^* - R_{ss}R_{sp}^*), \\
M_{21} &= C(|R_{pp}|^2 - |R_{sp}|^2 + |R_{ps}|^2 - |R_{ss}|^2), \\
M_{22} &= C(|R_{pp}|^2 - |R_{sp}|^2 - |R_{ps}|^2 + |R_{ss}|^2), \\
M_{23} &= C(R_{pp}R_{ps}^* - R_{sp}R_{ss}^* + R_{ps}R_{pp}^* - R_{ss}R_{sp}^*), \\
M_{24} &= iC(R_{pp}R_{ps}^* - R_{sp}R_{ss}^* - R_{ps}R_{pp}^* + R_{ss}R_{sp}^*), \\
M_{31} &= C(R_{pp}R_{sp}^* + R_{sp}R_{pp}^* + R_{ps}R_{ss}^* + R_{ss}R_{ps}^*), \\
M_{32} &= C(R_{pp}R_{sp}^* + R_{sp}R_{pp}^* - R_{ps}R_{ss}^* - R_{ss}R_{ps}^*), \\
M_{33} &= C(R_{pp}R_{ss}^* + R_{sp}R_{ps}^* + R_{ps}R_{sp}^* + R_{ss}R_{pp}^*), \\
M_{34} &= iC(R_{pp}R_{ss}^* + R_{sp}R_{ps}^* - R_{ps}R_{sp}^* - R_{ss}R_{pp}^*), \\
M_{41} &= -iC(R_{pp}R_{sp}^* - R_{sp}R_{pp}^* + R_{ps}R_{ss}^* - R_{ss}R_{ps}^*), \\
M_{42} &= -iC(R_{pp}R_{sp}^* - R_{sp}R_{pp}^* - R_{ps}R_{ss}^* + R_{ss}R_{ps}^*), \\
M_{43} &= -iC(R_{pp}R_{ss}^* - R_{sp}R_{ps}^* + R_{ps}R_{sp}^* - R_{ss}R_{pp}^*), \\
M_{44} &= C(R_{pp}R_{ss}^* - R_{sp}R_{ps}^* - R_{ps}R_{sp}^* + R_{ss}R_{pp}^*),
\end{aligned}
\tag{44}
$$

where

$$
C = \frac{\varepsilon_1}{2S}\left(\frac{\omega}{2\pi c}\right)^2 \frac{\cos^2\theta_s}{\cos\theta_0}. \tag{45}
$$

It is often useful when studying the Mueller matrix to normalize the elements of the Mueller matrix M_{ij} with respect to its first element M_{11}, i.e.

$$
m_{ij} = \frac{M_{ij}}{M_{11}}, \tag{46}
$$

since the first element only contains information about the intensity distribution of the scattered field.

Because we are dealing with randomly rough surfaces, we are interested in the Mueller matrix averaged over an ensemble of surface realizations $\langle M \rangle$. By repeating the same steps as we did for the MDRC [see Eq. (39) and (40)], we can separate the $\langle R_{\alpha\beta}R_{\alpha\beta}^* \rangle$ into a coherent (specular) and an incoherent (diffuse) component

$$
\begin{aligned}
\langle R_{\alpha\beta}R_{\delta\gamma}^* \rangle &= \langle R_{\alpha\beta} \rangle \langle R_{\delta\gamma}^* \rangle + (\langle R_{\alpha\beta}R_{\delta\gamma}^* \rangle - \langle R_{\alpha\beta} \rangle \langle R_{\delta\gamma}^* \rangle) \\
&= \langle R_{\alpha\beta}R_{\delta\gamma}^* \rangle_{coh} + \langle R_{\alpha\beta}R_{\delta\gamma}^* \rangle_{incoh}.
\end{aligned}
\tag{47}
$$

Applying this to the expressions in Eq. (44) allows us to decompose the Mueller matrix into a coherent and an incoherent component $\langle M \rangle_{coh}$ and $\langle M \rangle_{incoh}$.

2.11 The reflectivity for a plane wave source

The reflectivity is a measure of the fraction of power flux incident on a surface that is reflected coherently (specularly) by it. The reflectivity for incident β-polarized light is

defined by

$$\begin{aligned}\mathcal{R}_\beta(\theta_0) &= \sum_{\alpha=p,s}\int \mathrm{d}\Omega_s \left\langle \frac{\partial R_{\alpha\beta}(\boldsymbol{q}_\parallel|\boldsymbol{k}_\parallel)}{\partial\Omega_s}\right\rangle_{coh} \\ &= \sum_{\alpha=p,s}\int_0^{\pi/2} \mathrm{d}\theta_s \sin\theta_s \int_{-\pi}^{\pi} \mathrm{d}\phi_s \left\langle \frac{\partial R_{\alpha\beta}(\boldsymbol{q}_\parallel|\boldsymbol{k}_\parallel)}{\partial\Omega_s}\right\rangle_{coh}.\end{aligned} \tag{48}$$

In order to obtain the reflectivity of a two-dimensional randomly rough surface we need to begin with the following result,

$$\langle R_{\alpha\beta}(\boldsymbol{q}_\parallel|\boldsymbol{k}_\parallel)\rangle = (2\pi)^2\delta(\boldsymbol{q}_\parallel-\boldsymbol{k}_\parallel)\delta_{\alpha\beta}R_\alpha(k_\parallel), \tag{49}$$

where the Kronecker delta ensures the conservation of angular momentum and the delta function arises from the stationarity of the surface. We assume the roughness to be isotropic, which is why the function $R_\alpha(k_\parallel)$ only depends on the magnitude of the incident lateral wave vector $\boldsymbol{k}_\parallel$ and not on its direction. Using Eq. (49) along with the relation $(2\pi)^2\delta(\mathbf{0}) = S$, we can get an expression for the function $R_\alpha(k_\parallel)$ by setting $\boldsymbol{q}_\parallel = \boldsymbol{k}_\parallel$, resulting in

$$R_\alpha(k_\parallel) = \frac{1}{S}\langle R_{\alpha\beta}(\boldsymbol{k}_\parallel|\boldsymbol{k}_\parallel)\rangle. \tag{50}$$

Applying Eq. (49) to Eq. (41) yields the following expression for the coherent component of the MDRC

$$\left\langle \frac{\partial R_{\alpha\beta}(\boldsymbol{q}_\parallel|\boldsymbol{k}_\parallel)}{\partial\Omega_s}\right\rangle_{coh} = \varepsilon_1\left(\frac{\omega}{c}\right)^2\frac{\cos^2\theta_s}{\cos\theta_0}\left|R_\alpha(k_\parallel)\right|^2\delta(\boldsymbol{q}_\parallel-\boldsymbol{k}_\parallel)\delta_{\alpha\beta}, \tag{51}$$

where we have used

$$\begin{aligned}[(2\pi)^2\delta(\boldsymbol{q}_\parallel-\boldsymbol{k}_\parallel)\delta_{\alpha\beta}]^2 &= (2\pi)^4\delta(\mathbf{0})\delta(\boldsymbol{q}_\parallel-\boldsymbol{k}_\parallel)\delta_{\alpha\beta}^2 \\ &= (2\pi)^2 S\delta(\boldsymbol{q}_\parallel-\boldsymbol{k}_\parallel)\delta_{\alpha\beta}.\end{aligned} \tag{52}$$

With the identities

$$\delta(\boldsymbol{q}_\parallel-\boldsymbol{k}_\parallel) = \frac{1}{k_\parallel}\delta(q_\parallel-k_\parallel)\delta(\phi_s-\phi_0), \tag{53}$$

$$q_\parallel = \sqrt{\varepsilon_1}\frac{\omega}{c}\sin\theta_s \tag{54}$$

and

$$k_\parallel = \sqrt{\varepsilon_1}\frac{\omega}{c}\sin\theta_0, \tag{55}$$

we can rewrite Eq. (51) in the following manner

$$\begin{aligned}\left\langle \frac{\partial R_{\beta\beta}(\boldsymbol{q}_\parallel|\boldsymbol{k}_\parallel)}{\partial\Omega_s}\right\rangle_{coh} &= \sqrt{\varepsilon_1}\frac{\omega}{c}\frac{\cos^2\theta_s}{\cos\theta_0}\left|R_\beta(k_\parallel)\right|^2\frac{\delta(\sin\theta_s-\sin\theta_0)\delta(\phi_s-\phi_0)}{k_\parallel} \\ &= \frac{\cos^2\theta_s}{\cos^2\theta_0}\left|R_\beta(k_\parallel)\right|^2\frac{\delta(\theta_s-\theta_0)\delta(\phi_s-\phi_0)}{\sin\theta_0} \\ &= \left|R_\beta(k_\parallel)\right|^2\frac{\delta(\theta_s-\theta_0)\delta(\phi_s-\phi_0)}{\sin\theta_0}.\end{aligned} \tag{56}$$

Inserting this result into Eq. (48), followed by a summation over the outgoing polarization states α and integration over $d\Omega_s$, one arrives at the following expression for the reflectivity when the incident light is β-polarized

$$\begin{aligned}\mathcal{R}_\beta(\theta_0) &= \sum_{\alpha=p,s} \int \mathrm{d}\Omega_s \left\langle \frac{\partial R_{\alpha\beta}(\boldsymbol{q}_\parallel|\boldsymbol{k}_\parallel)}{\partial \Omega_s} \right\rangle_{coh} \\ &= \int_0^{\frac{\pi}{2}} d\theta_s \sin\theta_s \int_{-\pi}^{\pi} \mathrm{d}\phi_s \left\langle \frac{\partial R_{\beta\beta}(\boldsymbol{q}_\parallel|\boldsymbol{k}_\parallel)}{\partial \Omega_s} \right\rangle_{coh} = \left|R_\beta(k_\parallel)\right|^2 .\end{aligned} \tag{57}$$

If the light is unpolarized, the reflectivity is given by the sum over the reflectivity of both linear polarization states divided by two, i.e.

$$\mathcal{R}(\theta_0) = \frac{1}{2}\sum_{\beta=p,s} \mathcal{R}_\beta(\theta_0) = \frac{1}{2}\left[\left|R_p(k_\parallel)\right|^2 + \left|R_s(k_\parallel)\right|^2\right] \tag{58}$$

2.12 The reflectance for a plane wave source

In contrast with the reflectivity, the reflectance is a measure of the fraction of power flux incident on a surface which is reflected both coherently (specularly) and incoherently (diffusely) by the surface. Note that if the surface is planar, the reflectivity and reflectance are equal, since the light is only reflected coherently. The reflectance of β-polarized light is defined as

$$\mathscr{R}_\beta(\theta_0) = \sum_{\alpha=p,s} \mathscr{R}_{\alpha\beta}(\theta_0), \tag{59}$$

where

$$\mathscr{R}_{\alpha\beta}(\theta_0) = \int \mathrm{d}\Omega_s \left\langle \frac{\partial R_{\alpha\beta}(\boldsymbol{q}_\parallel|\boldsymbol{k}_\parallel)}{\partial \Omega_s} \right\rangle . \tag{60}$$

If the incident plane wave is unpolarized, then the average over both linear polarization states needs to be taken in order to obtain the reflectance. The reflectance of unpolarized directional illumination is then given by

$$\mathscr{R}(\theta_0) = \frac{1}{2}\sum_{\beta=p,s}\sum_{\alpha=p,s} \int \mathrm{d}\Omega_s \left\langle \frac{\partial R_{\alpha\beta}(\boldsymbol{q}_\parallel|\boldsymbol{k}_\parallel)}{\partial \Omega_s} \right\rangle . \tag{61}$$

Taking into account that the coherent contribution to the reflectance of β-polarized light is the reflectivity, one can write

$$\mathscr{R}_\beta(\theta_0) = \mathcal{R}_\beta(\theta_0) + \sum_{\alpha=p,s} \mathscr{R}_{\alpha\beta}(\theta_0)_{incoh}, \tag{62}$$

where

$$\mathscr{R}_{\alpha\beta}(\theta_0)_{incoh} = \int \mathrm{d}\Omega_s \left\langle \frac{\partial R_{\alpha\beta}(\boldsymbol{q}_\parallel|\boldsymbol{k}_\parallel)}{\partial \Omega_s} \right\rangle_{incoh} . \tag{63}$$

The reflectance of unpolarized light then reads

$$\mathscr{R}(\theta_0) = \frac{1}{2}\sum_{\beta=p,s} \mathscr{R}_\beta(\theta_0) = \mathcal{R}(\theta_0) + \sum_{\beta=p,s}\sum_{\alpha=p,s} \mathscr{R}_{\alpha\beta}(\theta_0)_{incoh}. \tag{64}$$

The transmittance can trivially be obtained by the relation

$$\mathscr{T}(\theta_0) = 1 - \mathscr{R}(\theta_0). \tag{65}$$

2.13 The reflectivity and reflectance for a diffuse source

If the randomly rough surface is illuminated by a incoherent (diffuse) source and not a coherent plane wave, the expressions for the reflectivty and reflectance in the two previous subsections are no longer valid. We assume that the incident light can then be described by a superposition of plane waves coming in from multiple directions with a random phase (incoherent superposition), i.e.

$$\mathbf{E}(\mathbf{x} \mid \omega) = \int\limits_{k_\parallel < \sqrt{\varepsilon_1}\frac{\omega}{c}} \mathrm{d}^2 k_\parallel \mathbf{E}_0\left(\boldsymbol{k}_\parallel\right) \exp\left[i\boldsymbol{k}_\parallel \cdot \boldsymbol{x}_\parallel - \mathrm{i}\alpha_1\left(k_\parallel \mid \omega\right) x_3\right] \tag{66}$$

Here $\mathbf{E}_0\left(\boldsymbol{k}_\parallel\right)$ is a random, complex amplitude function for a plane wave incident from the direction $[\boldsymbol{k}_\parallel - i\alpha_1(k_\parallel \mid \omega)\hat{\boldsymbol{x}}_3]$ onto the surface. The amplitude function $\mathbf{E}_0\left(\boldsymbol{k}_\parallel\right)$ constitutes an uncorrelated, complex stochastic process defined by the following properties

$$\left\langle \mathbf{E}_0\left(\boldsymbol{k}_\parallel\right)\right\rangle = 0, \tag{67a}$$

$$\left\langle \mathbf{E}_0\left(\boldsymbol{k}_\parallel\right)\mathbf{E}_0^*\left(\boldsymbol{k}'_\parallel\right)\right\rangle = \left|\mathbf{E}_0\left(\boldsymbol{k}_\parallel\right)\right|^2 \delta\left(\boldsymbol{k}_\parallel - \boldsymbol{k}'_\parallel\right), \tag{67b}$$

$$\left\langle \mathbf{E}_0\left(\boldsymbol{k}_\parallel\right)\mathbf{E}_0\left(\boldsymbol{k}'_\parallel\right)\right\rangle = 0. \tag{67c}$$

Note that Eqs. (67) are not satisfied for a purely real or imaginary stochastic process. The intensity of each beam given by $\boldsymbol{k}_\parallel$ is proportional to

$$I \propto \left\langle \left|\mathbf{E}_0\left(\boldsymbol{k}_\parallel\right)\right|^2 \right\rangle. \tag{68}$$

Diffuse illumination involves illumination from multiple angles of incidence, and in the limit of Lambertian illumination from all possible angles of incidence, with equal amplitude and probability. The amount of irradiance that the surface receives from each angle of incidence θ_0 can then be specified by an angular distribution $\ell(\theta_0)$, with the following property

$$\int \mathrm{d}\Omega_0 \ell(\theta_0) = 1. \tag{69}$$

The reflectance for illumination from a diffuse source is then given by the integral of the reflectance from plane wave illumination, weighted by $\ell(\theta_0)$, taken over all angles of incidence, resulting in

$$\begin{aligned} \mathscr{R} &= \int \mathrm{d}\Omega_0 \ell(\theta_0) \sum_{\beta=p,s}\sum_{\alpha=p,s} \int d\Omega_s \left\langle \frac{\partial R_{\alpha\beta}}{\partial \Omega_s} \right\rangle \\ &= \int \mathrm{d}\Omega_0 \ell(\theta_0) \mathscr{R}(\theta_0). \end{aligned} \tag{70}$$

For β-polarized incident light the reflectance from diffuse illumination reads

$$\mathscr{R}_\beta = \int \mathrm{d}\Omega_0 \ell(\theta_0) \mathscr{R}_\beta(\theta_0). \tag{71}$$

The reflectance of diffusely illuminated surfaces is sometimes referred to as the *diffuse-diffuse reflectance* and will occasionally be referred as such throughout this work. Note

that the transmittance $\mathscr{T}$ for diffuse illumination, can also be obtained from the diffuse-diffuse reflectance with the familiar relation $\mathscr{T} = 1 - \mathscr{R}$. In the case of Lambertian illumination [14, pp. 11–12], $\ell(\theta_0)$ is given by

$$\ell(\theta_0) = \frac{\cos(\theta_0)}{\pi}. \tag{72}$$

The reflectivity will then by definition be given by integrating the coherent component of the MDRC and taking the sum over the polarizations in the following way

$$\begin{aligned} \mathcal{R} &= \int \mathrm{d}\Omega_0 \ell(\theta_0) \sum_{\beta=p,s} \sum_{\alpha=p,s} \int d\Omega_s \left\langle \frac{\partial R_{\alpha\beta}}{\partial \Omega_s} \right\rangle_{coh} \\ &= \int \mathrm{d}\Omega_0 \ell(\theta_0) \mathcal{R}(\theta_0). \end{aligned} \tag{73}$$

For β-polarized incident light the reflectivity from diffuse illumination is given by

$$\mathcal{R}_\beta = \int \mathrm{d}\Omega_0 \ell(\theta_0) \mathcal{R}_\beta(\theta_0). \tag{74}$$

2.14 Conservation of energy

If we assume the two media to be non-absorbing ($Im[\varepsilon_i(\omega)] = 0$) for $i = 1, 2$), then the sum of the transmitted and scattered power should equal the incident power. The fraction of the incident power of a $\beta-$polarized beam which is reflected and transmitted into $\alpha-$polarized light is defined by

$$\mathcal{U}^{sc}_{\alpha\beta} = \int \mathrm{d}\Omega_s \left\langle \frac{\partial R_{\alpha\beta}}{\partial \Omega_s} \right\rangle \tag{75}$$

and

$$\mathcal{U}^{tr}_{\alpha\beta} = \int \mathrm{d}\Omega_t \left\langle \frac{\partial T_{\alpha\beta}}{\partial \Omega_t} \right\rangle, \tag{76}$$

respectively, where $\langle \partial T_{\alpha\beta}/\partial\Omega_t \rangle$ is the MDTC and $d\Omega_t$ is a solid angle about which light transmitted at the angles (θ_t, ϕ_t) passes through.

The sum over all outgoing polarizations states, should then equal unity since there is no loss of energy

$$\mathcal{U} = \sum_{\alpha=p,s} \mathcal{U}^{sc}_{\alpha\beta} + \mathcal{U}^{tr}_{\alpha\beta} = 1. \tag{77}$$

For absorbing media ($Im[\varepsilon_i(\omega)] \neq 0$ for $i = 1, 2$) Eq. (77) can be modified by adding an absorption term to the left side, however this term is difficult to calculate and will not be considered in this work.

These equations are frequently used as a starting point for confirming the accuracy of numerical simulations, and it is a very useful test for verifying if the criterion for the Rayleigh hypothesis (29) is satisfied.

3 Method

In this section the various computational methods required for calculating the quantities presented in the theory section are presented and described.

First, the use of dimensionless variables is explained along with the process of generating randomly rough surfaces. Then, the numerical methods used to solve the RRE for reflection are presented. Next, the calculation of the MDRC and Mueller matrix is described. Following, the technique used for determining the reflectivity and reflectance for both plane-wave and diffuse illumination is detailed. Finally, a test for assessing the quality of the simulations, using the law of energy conservation is presented.

3.1 Dimensionless variables

To reduce potential loss of numerical precision when performing operations on numbers of varying orders of magnitude, all variables are made dimensionless. The dispersion relation in vacuum reads

$$k = \omega/c = 2\pi/\lambda \tag{78}$$

By dividing all wave vectors by ω/c, and multiplying all lengths by ω/c, they are made dimensionless. All wave vectors are now measured in units ω/c, and all lengths are now effectively measured in units of $\lambda/2\pi$.

3.2 Generation of randomly rough surfaces

Each realization of a randomly rough surface was generated using a Fourier filtering method. The method consists of generating a set of uncorrelated Gaussian distributed random numbers on a grid, with a zero mean and a standard deviation of unity. The grid of random numbers is then Fourier transformed using a fast Fourier transform (FFT) algorithm and filtered by the square root of the power spectrum $\sqrt{g(\boldsymbol{k}_\parallel)}$. The filtered numbers are then scaled with the desired RMS height δ and inverse Fourier transformed; this results in correlated surfaces with the desired properties sampled on a grid. For further details about this method the reader is directed to Ref. [28].

This method requires that the analytical form of the power spectrum is known. However, in some cases the analytical Fourier transform of a correlation function is not know; for example, the Gaussian-cosine correlation function given by Eq. (18). To overcome this limitation in such cases, the power spectrum used in the Fourier filtering method was instead numerically generated by a complex FFT of the correlation function.

3.3 Discretization of the surfaces

The surfaces used in the scattering calculations were spatially limited and discretized. Each surface realization is spatially truncated to a finite quadratic area of $L \times L$, where L is the length of the surface along the each axis and $L \gg \lambda$. The randomly rough surfaces were generated using the Fourier filtering method and sampled on a grid of $N_x \times N_x$ points. The sampling intervals for this surface are then given by

$$\Delta x = \frac{L}{N_x}, \tag{79}$$

where N_x is the number of discretization points along one of the lateral axes x_i, $i = 1, 2$. The position of each point on the $\boldsymbol{x}_\parallel$ grid is then given by

$$\boldsymbol{x}_{\parallel_{\mathrm{i,j}}} = \left(-\frac{L}{2} + (i - 1/2)\Delta x, -\frac{L}{2} + (j - 1/2)\Delta x, 0 \right), \tag{80}$$

where $i, j = 1, 2, \ldots, N_x$. Note that this discretization scheme does not resolve the origin ($x_i = 0, i = 1, 2$) or the edges of the surface ($x_i = \pm L/2, i = 1, 2$).

3.4 Solving the reduced Rayleigh equation numerically

The RRE for scattering is solved by first truncating and discretizing the integral equation, this results in a matrix equation, where the scattering amplitudes are the elements of the unknown the equation is solved for. The equation can then be solved for the scattering amplitudes using a linear system solving scheme of choice. The details are presented below.

3.4.1 Discretization of the reduced Rayleigh equation integral

The initial step is to convert the integral in the RRE (34) into a sum over discretely sampled values. Note that the integral in the RRE is taken over the whole spectrum of scattering wave vectors $\boldsymbol{q}_\parallel$. Since it is not possible to calculate a numerical integral over an infinite spectrum, unless it converges, it is assumed that the contribution to the scattering process decreases as $q_\parallel \to \infty$. Under this assumption, a truncation of the integration to a finite interval should serve as a good approximation. The integration is then limited to the quadratic domain $\mathcal{Q} \times \mathcal{Q}$, where $\mathcal{Q}$ is the length of the domain along each component of the lateral wave vector.

The lateral scattering wave vector $\boldsymbol{q}_\parallel$ is then discretized on a quadratic grid of $N_q \times N_q$ points, with the separation distance Δq between each point in the $\hat{\boldsymbol{q}}_1$ and $\hat{\boldsymbol{q}}_2$ directions. The length can then be expressed as $\mathcal{Q} = \Delta q(N_q - 1)$. The position of each point on the $\boldsymbol{q}_\parallel$ grid is then given by

$$\boldsymbol{q}_{\parallel_{\mathrm{i,j}}} = \left(-\frac{\mathcal{Q}}{2} + i\Delta q, -\frac{\mathcal{Q}}{2} + j\Delta q, 0 \right), \tag{81}$$

where $i, j = 0, 1, 2, \ldots, N_q - 1$.

The integral in the RRE can now be converted into a sum over i and j by using a two-dimensional standard midpoint quadrature scheme, resulting in

$$\left(\frac{\Delta q}{2\pi} \right)^2 \sum_{\left|\boldsymbol{q}_{\parallel_{\mathrm{ij}}}\right| \leq \mathcal{Q}/2} \boldsymbol{M}^+(\boldsymbol{p}_\parallel | \boldsymbol{q}_{\parallel_{\mathrm{ij}}}) \boldsymbol{R}(\boldsymbol{q}_{\parallel_{\mathrm{ij}}} | \boldsymbol{k}_\parallel) = \boldsymbol{M}^-(\boldsymbol{p}_\parallel | \boldsymbol{k}_\parallel), \tag{82}$$

where $\boldsymbol{M}^+(\boldsymbol{p}_\parallel | \boldsymbol{q}_{\parallel_{\mathrm{ij}}})$ and $\boldsymbol{M}^-(\boldsymbol{p}_\parallel | \boldsymbol{k}_\parallel)$ were defined by Eq. (36) and the four components of $\boldsymbol{R}(\boldsymbol{q}_{\parallel_{\mathrm{ij}}} | \boldsymbol{k}_\parallel)$ are the unknowns that the equation is later solved for. The contribution to the sum from the corners of the quadratic domain is assumed to be insignificant; to further reduce computational costs, the integral is therefore limited to the circular domain $q_\parallel \leq \mathcal{Q}/2$. The number of values $\boldsymbol{q}_{\parallel_{\mathrm{i,j}}}$ in the circular area of integration can then be approximated to $\pi(N_q/2)^2$, the exact number depends on the choice of N_q and $\mathcal{Q}$.

3.4.2 Evaluating the $I(\gamma|\boldsymbol{Q}_\parallel)$ntegrals

Before solving the discretized RRE equation for scattering, the $I(\gamma|\boldsymbol{Q}_\parallel)$ integrals which appear in Eq. (36) and are defined in Eq. (37), have to be evaluated. Here $\boldsymbol{Q}_\parallel = \boldsymbol{p}_\parallel - \boldsymbol{q}_\parallel$ or $\boldsymbol{Q}_\parallel = \boldsymbol{p}_\parallel - \boldsymbol{k}_\parallel$, for $\gamma = \alpha_1(p_\parallel) \pm \alpha_2(q_\parallel)$ or $\gamma = \alpha_1(p_\parallel) \pm \alpha_2(k_\parallel)$, respectively. It should be noted that these integrals are Fourier transforms of the functions $\exp(-i\gamma\zeta(\boldsymbol{x}_\parallel))$. Solving these integrals numerically by either direct integration or using various FFT techniques is however very time consuming, since they have to be calculated for all possible values of the γ arguments.

An often used, more computationally efficient method [29, 30, 6], consists of Taylor expanding the exponential function $\exp(-i\gamma\zeta(\boldsymbol{x}_\parallel))$ and evaluating the resulting Fourier transforms of each power of the surface profile function $\zeta(\boldsymbol{x}_\parallel)$. The Taylor expansion gives

$$I(\gamma|\boldsymbol{Q}_\parallel) = \int \mathrm{d}^2 x_\parallel \left(\sum_{n=0}^{\infty} \frac{(-i\gamma\zeta^n(\boldsymbol{x}_\parallel))^n}{n!} \right) \exp(-i\boldsymbol{Q}_\parallel \cdot \boldsymbol{x}_\parallel). \tag{83}$$

We can rewrite the equation above in the following way

$$I(\gamma|\boldsymbol{Q}_\parallel) = \sum_{n=0}^{\infty} \frac{(-i\gamma)^n}{n!} \hat{\zeta}^{(n)}(\boldsymbol{Q}_\parallel), \tag{84}$$

where $\hat{\zeta}^{(n)}(\boldsymbol{Q}_\parallel)$ denotes the Fourier transform of $\zeta^n(\boldsymbol{x}_\parallel)$, as expressed below

$$\hat{\zeta}^{(n)}(\boldsymbol{Q}_\parallel) = \int \mathrm{d}^2 x_\parallel \zeta^n(\boldsymbol{x}_\parallel) \exp(-i\boldsymbol{Q}_\parallel \cdot \boldsymbol{x}_\parallel). \tag{85}$$

If $\left|\gamma\zeta(\boldsymbol{x}_\parallel)\right| \ll 1$, the Taylor expansion will converge sufficiently fast for a truncation of the sum in (84), at a finite value N, to serve as a reasonable approximation. Note that the oscillatory nature of the Taylor expansion can make it numerically unstable when $\left|\gamma\zeta(\boldsymbol{x}_\parallel)\right|$ is large; this places additional constraints on the RMS height of the surface profile function, which are more restrictive than the ones given by the Rayleigh criterion (29). The advantage of this method is that the Fourier transforms $\hat{\zeta}^{(n)}(\boldsymbol{q}_\parallel)$ only have to be calculated once for each exponent of power $n = 0, 1, \ldots, N$, since they are independent of the values of γ. Therefore, it is not necessary to recalculate the Fourier transforms for each value of γ, which reduces the computation time of the $I(\gamma|\boldsymbol{Q}_\parallel)$ integrals considerably.

Note that this method requires that all values of $\boldsymbol{p}_\parallel - \boldsymbol{q}_\parallel$ and $\boldsymbol{p}_\parallel - \boldsymbol{k}_\parallel$ lie on the same grid as the grid of wave vectors $\boldsymbol{Q}_\parallel$ resolved by the Fourier transforms in Eq. (85). To ensure this, we choose to resolve both $\boldsymbol{p}_\parallel$, $\boldsymbol{k}_\parallel$ and consequently $\boldsymbol{Q}_\parallel$ on the same grid as the one we used for $\boldsymbol{q}_\parallel$. However, this means that we can only calculate the reflection amplitudes for incident wave vectors $\boldsymbol{k}_{\parallel_{\mathrm{m,n}}}$ which lie on the grid $\boldsymbol{q}_{\parallel_{\mathrm{i,j}}}$. If we desire some specific angles of incidence (θ_0, ϕ_0), we have to adjust N_q and $\mathcal{Q}$ such that $\boldsymbol{k}_\parallel$ lies on the sampling grid.

3.4.3 Determining the sampling parameters

The Fourier transforms given by Eq. (85) can then be evaluated numerically with a FFT, using the surface realizations discretized on the grid given by Eq. (80). From Eqs. (85) and (82) it follows that we require the two wave number components of $\boldsymbol{Q}_\parallel$ to lie within the range $[-\mathcal{Q}, \mathcal{Q}]$ to evaluate all the $I(\gamma|\boldsymbol{Q}_\parallel)$ integrals. The highest possible wave number

we can resolve with the FFT is given by the *Nyquist frequency* π/Δ_x [31, pp. 500-501], the wave number limits $\mathcal{Q}$ must then satisfy the following inequality

$$\frac{\pi}{\Delta_x} \geq \mathcal{Q} = \Delta_q(N_q - 1). \tag{86}$$

From the theory of discrete Fourier transforms, it is know that the discretization intervals in real and wave number space are related by [31, pp. 501-504]

$$\Delta_q = \frac{2\pi}{L} = \frac{2\pi}{N_x \Delta_x}. \tag{87}$$

Applying this to the inequality in Eq. (86), we get the following relation for the number of discretization points along each axis in the $\boldsymbol{x}_{\parallel_{\mathrm{i,j}}}$ and $\boldsymbol{q}_{\parallel_{\mathrm{i,j}}}$ grids

$$N_x \geq 2(N_q - 1). \tag{88}$$

When $\boldsymbol{p}_\parallel$ and $\boldsymbol{q}_\parallel$ are discretized on the same grid, the number of possible values $\boldsymbol{p}_\parallel - \boldsymbol{q}_\parallel$ is $2N_q - 1$, where the number of possible values for each lateral wave vector is N_q. To ensure that enough points are resolved by the FFT, we choose a N_q such that $2N_q - 1$ is equal to the number of elements along each axis of the $\boldsymbol{x}_\parallel$ grid we calculate the FFT over. Note that the FFT always resolves the zero frequency, and the Fourier transform of a real function is symmetric around the zero frequency under complex conjugation. The number of elements which are possible to resolve with the FFT will then always be odd. The number of discretization points along each axis of the $\boldsymbol{q}_{\parallel_{\mathrm{i,j}}}$ grid is then given by

$$N_q = \left\lfloor \frac{N_x + 2}{2} \right\rfloor. \tag{89}$$

Here $\lfloor x \rfloor$ denotes the floor function of x, which rounds x to the largest integer less than or equal to x. This means $\mathcal{Q}$ is effectively set to the highest wave number resolvable by the FFT, i.e

$$\mathcal{Q} = \Delta_q \left\lfloor \frac{N_x}{2} \right\rfloor. \tag{90}$$

3.4.4 Solving the linear RRE system

Discretizing $\boldsymbol{p}_\parallel$ and $\boldsymbol{k}_\parallel$ on the same grid as $\boldsymbol{q}_\parallel$, results in (82) forming a closed set of linear equations. The resulting matrix equation is given by

$$\left(\frac{\Delta q}{2\pi}\right)^2 \sum_{\left|\boldsymbol{q}_{\parallel_{\mathrm{ij}}}\right| \leq \mathcal{Q}/2} \boldsymbol{M}^+(\boldsymbol{p}_{\parallel_{\mathrm{kl}}} | \boldsymbol{q}_{\parallel_{\mathrm{ij}}}) \boldsymbol{R}(\boldsymbol{q}_{\parallel_{\mathrm{ij}}} | \boldsymbol{k}_{\parallel_{\mathrm{mn}}}) = \boldsymbol{M}^-(\boldsymbol{p}_{\parallel_{\mathrm{kl}}} | \boldsymbol{k}_{\parallel_{\mathrm{mn}}}). \tag{91}$$

According to Eq. (24) we only need two components of $\boldsymbol{R}(\boldsymbol{q}_\parallel | \boldsymbol{k}_\parallel)$ to fully determine the scattered field for a given polarization. Therefore we only need to solve for $R_{p\beta}$ and $R_{s\beta}$ if the incident light is β-polarized, which makes the total number of unknown elements twice the number of values of $\boldsymbol{q}_{\parallel_{\mathrm{i,j}}}$. Note that only the right hand side of the matrix equation is dependent on $\boldsymbol{k}_\parallel$ and the polarization, while the left hand side is the same for both polarizations and all incident angles.

The linear system of equations can then be solved using a linear system solving scheme of choice. In this work the systems was solved using a LU decomposition scheme, which consists of writing the system matrix (A) as the product of a lower triangular matrix (L) with a upper triangular matrix (U), i.e.

$$Ax = (LU)x = b, \tag{92}$$

where A is a square system matrix and x is the unknown we need to solve for. The system is then solved by first solving

$$Ly = b \tag{93}$$

for y, and next solving the system

$$Ux = y \tag{94}$$

for x. The two equations above are solved by using the iterative processes called forward and back substitution. There are several variations of this method, which often includes an additional permutation matrix P, for further details the reader is directed to Ref. [32].

The most time consuming part of solving the RRE is to calculate the system matrix and performing the LU decomposition. Calculating the right hand side, along with the forward and back substitution requires considerably less time. Since only the right hand side is dependent on the incident wave vector $\boldsymbol{k}_\parallel$, it is possible to perform the forward and back substitution for multiple polar angles of incidence θ_0 resolved on the grid of lateral wave vectors, for relatively little additional computational cost.

3.5 Calculation of the MDRC and the Mueller matrix elements

Solving the RRE numerically yields the four scattering amplitudes $R_{\alpha\beta}(\boldsymbol{k}_\parallel, \boldsymbol{q}_\parallel)$ for incident α-polarized light with lateral wave vector $\boldsymbol{k}_\parallel$, scattered by the surface into β-polarized light with lateral wave vector $\boldsymbol{q}_\parallel$. The resulting amplitudes are discretized on the grid given by (81) and limited to the circular domain of propagating modes ($\operatorname{Im}\alpha(q_\parallel) = 0$) with radius $\sqrt{\varepsilon_1}\omega/c$. Numerically the amplitudes are given by matrices of size $N \times N$, where N is the number of points along one axis such that $|q_i| \leq \sqrt{\varepsilon_1}\omega/c, i = 1, 2$. Note that since the amplitudes are defined on a circular domain and discretized on a square grid, the points outside the circle do not contribute and are therefore set to zero.

The MDRC including it's coherent and incoherent component can be calculated directly using Eqs. (38), (41) and (42), repecively. Since the MDRC is a function of $\boldsymbol{q}_\parallel$, which depends on θ_s, we need to express θ_s as a function of $\boldsymbol{q}_\parallel$. By using Eq. (54) we get

$$\theta_s(\boldsymbol{q}_\parallel) = \sin^{-1}\left(\sqrt{\varepsilon_1}\frac{c}{\omega}\left|\boldsymbol{q}_\parallel\right|\right), \tag{95}$$

which is only valid in the circular region $\boldsymbol{q}_\parallel \leq \sqrt{\varepsilon_1}\omega/c$, where $\boldsymbol{q}$ is a wave vector which satisfies the dispersion relation (5) and describes propagating modes.

The Mueller matrix elements are directly obtained from Eq. (44) along with Eq. (95), no additional numerical methods are required. The coherent and incoherent components are obtained by using Eq. (47). The normalized matrix elements are given by Eq. (46), since each Mueller matrix element is numerically given by a $N \times N$ matrix, the normalization requires element-wise matrix division.

3.6 Numerical calculation of the reflectivity and reflectance

After solving the RRE for the scattering amplitudes and calculating the MDRC, the reflectivity and reflectance of the randomly rough surface for both plane-wave and diffuse illumination can be obtained in the following way.

3.6.1 Plane-wave illumination

The reflectivity of a randomly rough surface illuminated by plane-waves is given by (57) and (58) for polarized and unpolarized incident light, respectively. The reflectivity is acquired by calculating the squared norms of the scattering amplitudes for $\boldsymbol{q}_\parallel = \boldsymbol{k}_\parallel$, no further numerical techniques are required.

The reflectance of the surface for plane-wave illumination is given by Eqs. (59) and (64) for polarized and unpolarized incident light, respectively. As shown in Sec. 2.12 the reflectance can be separated into the sum of the reflectivity and the incoherent component of the reflectance. Since the reflectivity is easily determined from the scattering amplitudes, we only need to determine the incoherent contribution to the reflectivity given by

$$\mathscr{R}_\beta(\theta_0)_{incoh} = \sum_{\alpha=p,s} \mathscr{R}_{\alpha\beta}(\theta_0)_{incoh}, \tag{96}$$

where

$$\mathscr{R}_{\alpha\beta}(\theta_0)_{incoh} = \int \mathrm{d}\Omega_s \left\langle \frac{\partial R_{\alpha\beta}(\boldsymbol{q}_\parallel|\boldsymbol{k}_\parallel)}{\partial \Omega_s} \right\rangle_{incoh}. \tag{97}$$

Here the integration is over all possible scattering angles (θ_s, ϕ_s), and has to be evaluated numerically. Since the MDRC is a numerical function of $\boldsymbol{q}_\parallel$ we need to convert the integral over $\mathrm{d}\Omega_s$ into an integral over $\mathrm{d}\boldsymbol{q}_\parallel$. First, we write out the integral above using the identity for a solid angle element in three dimensions $\mathrm{d}\Omega_s = \sin\theta_s \, \mathrm{d}\theta_s \, \mathrm{d}\phi_s$, this gives us

$$\mathscr{R}_{\alpha\beta}(\theta_0)_{incoh} = \int_0^{\frac{\pi}{2}} \mathrm{d}\theta_s \sin\theta_s \int_{-\frac{\pi}{2}}^{\frac{\pi}{2}} \mathrm{d}\phi_s \left\langle \frac{\partial R_{\alpha\beta}(\boldsymbol{q}_\parallel|\boldsymbol{k}_\parallel)}{\partial \Omega_s} \right\rangle_{incoh}. \tag{98}$$

By applying the relation $\mathrm{d}\theta_s = \mathrm{d}(\sin\theta_s)/\cos\theta_s$, we get

$$= \int_0^1 \mathrm{d}(\sin\theta_s) \sin\theta_s \int_{-\frac{\pi}{2}}^{\frac{\pi}{2}} \mathrm{d}\phi_s \frac{1}{\cos\theta_s} \left\langle \frac{\partial R_{\alpha\beta}(\boldsymbol{q}_\parallel|\boldsymbol{k}_\parallel)}{\partial \Omega_s} \right\rangle_{incoh}. \tag{99}$$

Next, we use that $q_\parallel = \sqrt{\varepsilon_1}(\omega/c)\sin\theta_s$,

$$\begin{aligned} &= \int_0^{\sqrt{\varepsilon_1}\frac{\omega}{c}} \mathrm{d}\left(\sqrt{\varepsilon_1}\frac{\omega}{c}\sin\theta_s\right) \sqrt{\varepsilon_1}\frac{\omega}{c}\sin\theta_s \int_{-\frac{\pi}{2}}^{\frac{\pi}{2}} \mathrm{d}\phi_s \frac{c^2}{\varepsilon_1\omega^2\cos\theta_s} \left\langle \frac{\partial R_{\alpha\beta}(\boldsymbol{q}_\parallel|\boldsymbol{k}_\parallel)}{\partial \Omega_s} \right\rangle_{incoh} \\ &= \int_0^{\frac{\omega}{c}} \mathrm{d}q_\parallel q_\parallel \int_{-\frac{\pi}{2}}^{\frac{\pi}{2}} \mathrm{d}\phi_s \frac{c^2}{\varepsilon_1\omega^2\cos\theta_s} \left\langle \frac{\partial R_{\alpha\beta}(\boldsymbol{q}_\parallel|\boldsymbol{k}_\parallel)}{\partial \Omega_s} \right\rangle_{incoh}. \end{aligned} \tag{100}$$

Finally, we can simplify the integral with the relation $\mathrm{d}\boldsymbol{q}_\parallel = q_\parallel \, \mathrm{d}q_\parallel \, \mathrm{d}\phi_s$, resulting in

$$\mathscr{R}_\beta(\theta_0)_{incoh} = \sum_{\alpha=p,s} \int \mathrm{d}\boldsymbol{q}_\parallel \frac{c^2}{\omega^2\cos\theta_s} \left\langle \frac{\partial R_{\alpha\beta}(\boldsymbol{q}_\parallel|\boldsymbol{k}_\parallel)}{\partial \Omega_s} \right\rangle_{incoh}. \tag{101}$$

Since the lateral scattering wave vector depends on the polar scattering angle, we need to express $\cos\theta_s$ as a function of $\boldsymbol{q}_\parallel$, when integrating over $\boldsymbol{q}_\parallel$. The reflectance can then be obtained by using a numerical integration scheme on Eq. (101), i.e.

$$\mathscr{R}_\beta(\theta_0)_{incoh} = \sum_{\alpha=p,s}\sum_{i,j} w_{i,j}\frac{c^2}{\omega^2\cos\theta_s(\boldsymbol{q}_{\parallel_{\mathrm{i,j}}})}\left\langle\frac{\partial R_{\alpha\beta}(\boldsymbol{q}_{\parallel_{\mathrm{i,j}}}|\boldsymbol{k}_{\parallel_{\mathrm{m,n}}})}{\partial\Omega_s}\right\rangle_{incoh}, \tag{102}$$

where $w_{i,j}$ are weights given by a quadrature scheme of choice and $\theta_s(\boldsymbol{q}_\parallel)$ is given by (95). For the best precision an integration scheme for a circular disk domain is recommended.

To further improve the accuracy of the numerical integration, we can increase the resolution by adding more points along the edge of the circular integration domain. Since the edge of the domain contains only the contribution from grazing angles, the added points can be set to zero. This results in a set of unevenly distributed points, which can then be interpolated with an interpolation scheme to create a function of the integrand. The function can then be integrated at a higher precision than what was achievable before.

3.6.2 Diffuse illumination

The reflectivity and reflectance of a randomly rough surface illuminated by a diffuse light source is given by Eqs. (73) and (70), respectively. Both calculations require the reflectivity and reflectance for plane-wave illumination to be known for all polar incident angles resolvable on the grid $\boldsymbol{q}_{\parallel_{\mathrm{i,j}}}$, in the circular domain $q_\parallel \leq \sqrt{\varepsilon_1}\omega/c$. The two resulting functions of θ_0 then have to be multiplied by the weight function $\ell(\theta_0)$ and integrated over θ_0, resulting in the reflectivity and reflectance of the randomly rough surface illuminated by a diffuse source. In this work we will only consider diffuse illumination from a Lambertian source, with the weight function $\ell(\theta_0)$ given by (72). The integrals can then be evaluated with a standard quadrature scheme.

For the integration to yield precise enough results, it is important to have enough resolvable polar angles. The number of angles can be increased by adjusting the side lengths of the system L along with the number of discretization points N_q. By only increasing N_q the resolution of the grid $\boldsymbol{q}_{\parallel_{\mathrm{i,j}}}$ increases, however, the length of the grid Q increases linearly with N_q which results in fewer points inside the region $\boldsymbol{q}_\parallel \leq \sqrt{\varepsilon_1}\omega/c$ and in turn fewer angles can be resolved. In addition, increasing the number of points raises the computational cost dramatically. The highest resolvable wave-number Q is inversely proportional with the length of the system L, therefore one has to increase the system size along with the number of grid points to attain more resolvable incident angles. The system size and number of discretization points have to be balanced with the limitations of the computational infrastructure used, the details of the values and systems used to attain the results in this work will be presented in the results and discussion section Sec. 4. Since increasing N_q raises the computational demand, a lower resolution can be used together with an interpolation scheme instead, using the fact that the reflectance and reflectivity should tend to unity for grazing angles.

3.7 The energy conservation test

A simple test frequently used to measure the quality of electromagnetic wave scattering simulations [2, 4, 22], is to confirm if the incident power is conserved by the scattering process. This method can be used to verify the validity of the Rayleigh hypothesis, for the

roughness parameters of the surface one wishes to study. Ultimately, this test is used for controlling that the results are not incorrect by considering the conservation of energy.

Through the interaction with the surface the incident power will be split into a scattered, transmitted and absorbed part. Since the absorbed part is hard to calculate, absorbing materials were not considered when the surface parameters used in this work were tested.

The method consists of calculating the fraction of incident power which is reflected and transmitted, the sum of these two parts should then equal unity. If the substrate used in this test is metallic ($\mathrm{Re}\,\varepsilon_2 < 0$), all of the incident light is reflected and only the reflected part needs to be considered.

Using Eqs. (75) and (76), we can calculate the fraction of the incident power flux of $\beta-$polarized light scattered by and transmitted through the surface into α-polarized light, respectively. Note that this requires the calculation of the MDTC in addition to the MDRC, which can be time-consuming to acquire. When testing the surface roughness parameters, it is therefore more efficient to set the substrate to be a non-absorbing metal and only calculate the reflected fraction of the power flux, since all of the incident light should be reflected. Taking the sum of the power fractions for all polarizations should then result in unity, due to the conservation of the incident energy, i.e. Eq. (77).

Because of loss of significance in such numerical calculations, small deviation from unity should be expected. It should be emphasized that the conservation of the incident power flux is a necessary condition, however, it does not automatically guarantee that the simulations are correct when it is satisfied.

The energy conservation and the quality of the simulations for the roughness parameters used in this work, will be discussed in Sec. 4.

4 Results and Discussion

Following the approach outlined in the method section, simulations solving the reduced Rayleigh equation for reflection were performed for various systems consisting of two media separated by a two-dimensional randomly rough interface. The simulations were conducted on high performance computing (HPC) clusters using parallel processing. The results obtained from the computer simulations are presented and discussed in this section.

The quantities obtained from the simulation results, which will be discussed here, are the mean differential reflection coefficient, the Mueller matrix, and the reflectivity and reflectance of randomly rough surfaces. The results are presented in three subsections, one for each auto-correlation function studied in this work.

First, results for Gaussian-correlated (16) surfaces are presented and discussed. The surfaces separate vacuum in the upper region, from glass or silver in the lower region. The scattering of electromagnetic waves from randomly rough surfaces has for the past decades mainly been studied using Gaussian-correlated surfaces; they are therefore considered to represent the classical example of a randomly rough surface. Here, the MDRC and Mueller matrix will serve as a reference for comparison and contrasting with other surfaces studied in this work. The main result of this section is the numerically obtained reflectivity and reflectance of diffusely illuminated two dimensional randomly rough surfaces, which are presented here for the first time. The reflectance and reflectivity are only studied for Gaussian surfaces, since the computational demand was quite high. Moreover, only glass surfaces are studied, as the goal is to compare the results to the ones which were obtained in 2016 by González-Alcalde et al. for one-dimensional Gaussian-correlated glass surfaces [7].

Secondly, the full angular distribution of the MDRC and Mueller matrix of Gaussian-cosine correlated surfaces is presented and discussed in detail. Simulations were performed for two systems with different correlation lengths a and RMS heights δ. Both systems were characterized by the isotropic Gaussian-cosine correlation function (18), and consist of vacuum in the upper region and silver in the lower region. Here the MDRC and Mueller matrix will be studied and compared to the results for Gaussian-correlated surfaces.

Thirdly, to study how anisotropy in the Gaussian-cosine correlation function (19) affects the scattering, simulations were performed for two vacuum-silver interfaces with the correlation length doubled in the x_2-direction. To highlight the differences that arise due to anisotropy, the MDRC of the anisotropic Gaussian-cosine surfaces is compared to the results for the isotropic ones. Only the MDRC is shown and discussed for these surfaces due to time constraints.

The incident light is described by its wavelength λ, which was set to the operating wavelength of a He-Ne laser $\lambda = 0.6328\,\mu\text{m}$ in all the simulations. The direction of the incident light is given by the polar and azimuthal angles of incidence , θ_0 and ϕ_0, respectively. To reduce the noise and statistical fluctuations, a large number of surface realizations was used to obtain the average reflection amplitudes of the surfaces. The integrals $I(\gamma|\boldsymbol{Q}_{\parallel})$ required only 18 terms in the Taylor expansions to be sufficiently convergent for all simulations. The numerical parameters and the quality of the simulations will be presented along with the results.

4.1 Gaussian-correlated surfaces

Numerical simulations were performed for a Gaussian-correlated glass surface, with a high number of resolvable angles on the grid of lateral wave vectors. The high resolution of angles allowed the reflectivity and reflectance for diffuse illumination to be obtained with a high precision. The number of resolvable angles was halved for the Gaussian-correlated silver surface and later simulations to reduce the computational demand and run time.

The surface realizations were generated using the Fourier filtering method outlined in Sec. 3.2, with the Gaussian power spectrum given by Eq. (16). A square segment of a numerical realization of the Gaussian-correlated surface can be seen in Fig. 2.

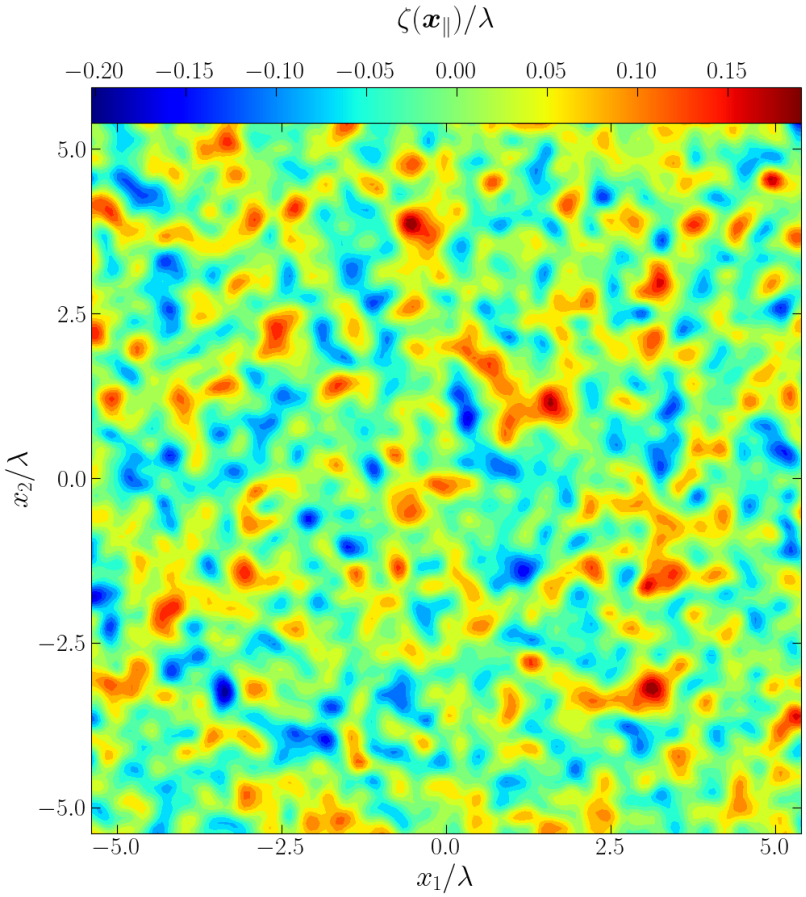

Figure 2: Square segment of a numerically generated realization of the surface profile function $\zeta(\boldsymbol{x}_\parallel)$, characterized by an isotropic Gaussian power spectrum (16). The surface has a correlation length of $a = \lambda/4$ and RMS height of $\delta = \lambda/20$, where λ is the wavelength of the light incident on the surface.

The correlation lengths of the glass surface were $a_1 = a_2 = a = 0.25\lambda$ and the RMS height was $\delta = 0.05\lambda$. The surface in Fig. 2 is characterized by the same parameters. The surface realizations were limited to a quadratic area of $L \times L$ with $L = 50\lambda$, and discretized onto a grid of $N_x \times N_x$ points with $N_x = 561$. This implies 281 points resolved along each axis of the $\boldsymbol{q}_{\parallel_{\mathrm{i,j}}}$ grid, and the integral in Eq. (91) to have a cutoff at $\pm\mathcal{Q}/2 = \pm 2.8\omega/c$. The number of polar angles resolved with these parameters was $N_\theta = 51$.

The surface acts as an interfaces between vacuum in the upper region (ambient), where the light is incident from, and glass in the lower region (substrate). The dielectric constant of vacuum is given by $\varepsilon_1 = 1$. Assuming a refraction index of $n = 1.5$ for the glass substrate at the wavelength $\lambda = 632.8\,\text{nm}$, the dielectric constant used for the substrate was $\varepsilon_2(\omega) = 2.25$. The simulation results were averaged over an ensemble of $N_s = 5586$ surface realizations. The quality of the simulations was evaluated for these parameters with the energy conservation test presented in the Sec. 3.7. Using Eq. (77), it was found for this system that $|\mathcal{U} - 1| \leq 2.3 \times 10^{-7}$, i.e., the criterion for energy conservation is satisfied within $2.3 \times 10^{-5}\%$.

The Gaussian-correlated silver surface was characterized by the correlation length $a = \lambda/4$ and RMS height $\delta = \lambda/40$. The dielectric function of silver at the wavelength $\lambda = 632.8\,\text{nm}$, is given by $\varepsilon_2(\omega) = -16.0 + i1.088$ [33]. The length of the surface realizations was $L = 25\lambda$ and the number of discretization points was $N_x = 321$. The energy conservation test was performed with non-absorbing silver ($\varepsilon_2(\omega) = -16.0$), the criterion was found to be satisfied within 0.2%. The results were averaged over an ensemble of 5021 surface realizations.

4.1.1 The mean differential reflection coefficient

Using the reflection amplitudes obtained from the simulations, the MDRC was calculated for light scattered incoherently (diffusely) by the Gaussian-correlated glass and silver surfaces using Eq. (42). Results are shown below for both normal and non-normal incidence.

Since the surfaces used in these simulations have an isotropic auto-correlation function, the following results should be identical for all azimuthal angles of incidence ϕ_0, except for an angular rotation of the distributions by the same angle. It should be noted that the plane of incidence was defined in the simulations as the plane spanned by $\hat{\boldsymbol{x}}_3$ and $\hat{\boldsymbol{\phi}}_0 = -\sin(\phi_0)\hat{\boldsymbol{q}}_1 + \cos(\phi_0)\hat{\boldsymbol{q}}_2$, which is well-defined, even for the normal-polar angle of incidence. The plane of incidence for the results presented here is, therefore, the x_1x_3-plane.

Figs. 3 and 4 show the in-plane scattering ($\phi_s = 0°$) MDRC as a function of the polar angle of scattering θ_s, for the vacuum-glass and vacuum-silver systems, respectively. The angles of incidence were: $(\theta_0, \phi_0) = (0.0°, 0.0°)$ in Figs. 3(a) and 4(a); $(\theta_0, \phi_0) = (34.05°, 0.0°)$ in Figs. 3(b) and 4(b). Here and in the rest of the work the notation $\beta \to \alpha$ denotes incident β polarized light scattered into α-polarized light. When $\beta = \alpha$ ($s \to s$ and $p \to p$) the scattered light is co-polarized, oppositely, when $\beta \neq \alpha$ ($s \to p$ and $p \to s$) the scattered light is cross-polarized.

From the vacuum-glass results presented in Fig. 3 it is clearly seen that the in-plane scattering is dominated by co-polarized scattering, while cross-polarized scattering hardly contributes. It is worth noting that in-plane cross-polarized scattering has no contribution from single-scattering and is therefore a pure multiple-scattering effect, the same holds for out-of-plane ($\phi_s = 90°$) co-polarized scattering. For weakly to moderately rough surfaces, such as the ones presented in this work, multiple-scattering is mainly caused by the excitation of surface plasmon polaritons (SPPs), which generally require a metal substrate (see Sec. 2.2). Therefore, it is not surprising that the in-plane contribution from cross-polarized light is not present for a vacuum-glass interface at this degree of roughness. For the vacuum-silver surface, shown in Fig. 4, SPPs can be excited and the multiple-scattering contribution is therefore present as expected.

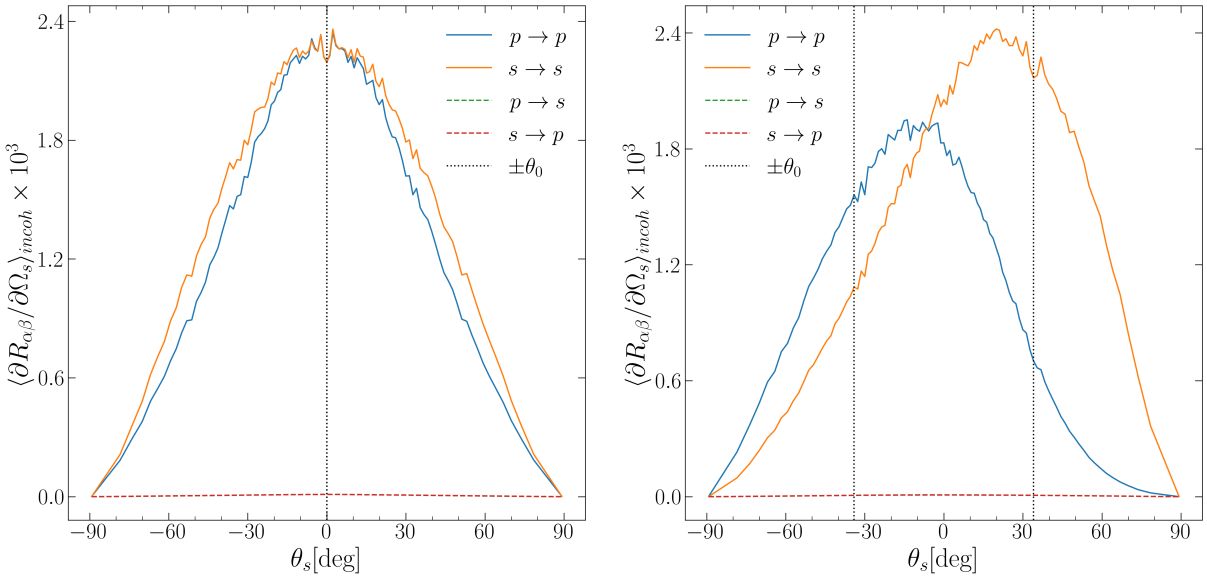

(a) $\theta_0 = 0.0°$ (b) $\theta_0 = 34.05°$

Figure 3: The incoherent component of the MDRC (42) for in-plane scattering from a randomly rough surface separating vacuum and glass as a function of the scattering angle θ_s. The wavelength of the incident light (in vacuum) was $\lambda = 632.8\,\text{nm}$ and the polar angle of incidence was in panel (a) $\theta_0 = 0.0°$; in panel (b) $\theta_0 = 34.05°$. The refractive index of glass at this wavelength is assumed to be $n = 1.5$, which corresponds to a dielectric function of $\varepsilon_2(\omega) = 2.25$. The surface realizations were limited to the area $50\lambda \times 50\lambda$ and discretized on grids of 561×561 points. The surface realizations were characterized by a Gaussian power spectrum with correlation length $a = \lambda/4$ and an RMS height of $\delta = \lambda/20$. The MDRC was averaged over an ensemble of $N_s = 5586$ surface realizations. Here $\alpha \to \beta$ denotes β-polarized incident light scattered into α-polarized light. The vertical dashed lines denote the angle of specular and retro-specular direction of scattering, $\pm\theta_0$, respectively.

The MDRC for normal incidence, seen in Fig. 3(a) for glass and Fig. 4(a) for silver, are near evenly distributed around $\theta_s = 0.0°$. For the polar angle of incidence $\theta_0 = 34.05°$, seen in Fig. 3(b) for glass and Fig. 4(b) for silver, we can see that the the $p \to p$ scattered light is more concentrated in the backscattering direction $\theta_s < 0°$, while the opposite is true for $s \to s$ scattering. This is a trend which continues and intensifies for increasing polar angles of incidence θ_0. In addition, it is observed for glass that s-polarized incident light is scattered more by the surface. Conversely, for the silver surface, $p \to p$ scattering contributes more than $s \to s$; this is suspected to be caused by interactions with SPPs. For flat surfaces s-polarized incident light cannot excite SPPs [3, pp. 18–20]; for rough surfaces this is possible, which the $s \to p$ presence in the in-plane scattering indicates. However, the coupling to SPP modes is much stronger for p-polarized light, which might result in an additional contribution to p-polarized scattered light.

For some angles of incidence, small pronounced peaks are observed in the retro-specular direction ($\theta_s = -\theta_0$) in the MDRC of vacuum-silver interface. These peaks are called *enhanced backscattering peaks* and they are the result of a multi scattering phenomenon which for weakly rough surfaces involves the excitation of SPP's [3, pp. 50–57]. Shortly summarized, it is a coherent effect where light scattered twice by the surface, interferes

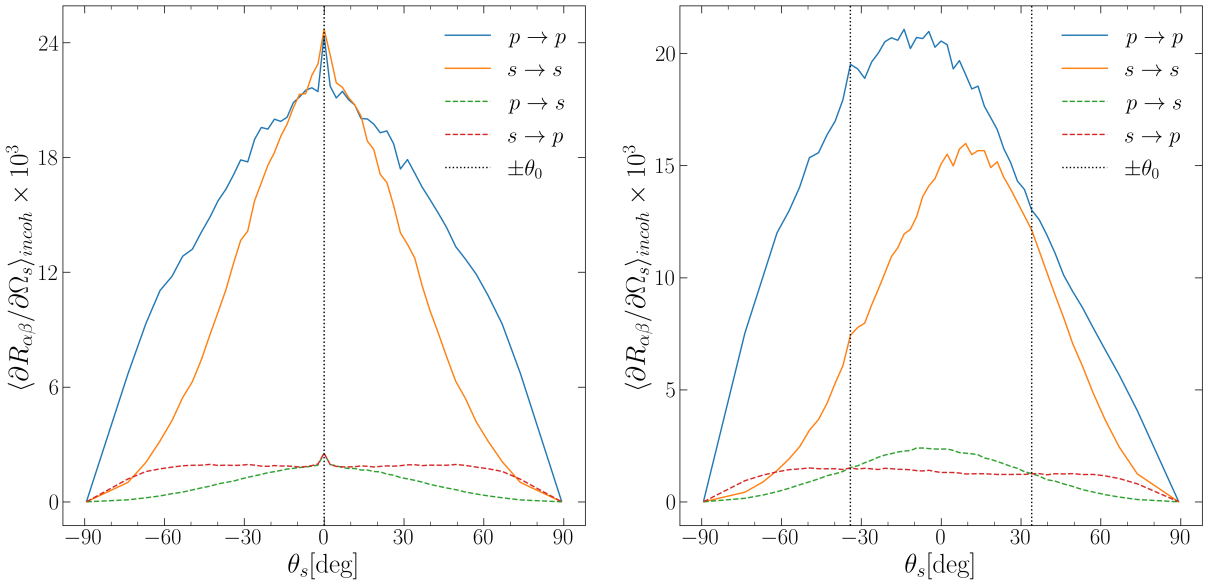

(a) $\theta_0 = 0.0°$ (b) $\theta_0 = 34.05°$

Figure 4: The incoherent component of the MDRC (42) for in-plane scattering from a randomly rough surface separating vacuum and silver as a function of the scattering angle θ_s. The wavelength of the incident light (in vacuum) was $\lambda = 632.8\,\text{nm}$ and the polar angle of incidence was in panel (a) $\theta_0 = 0.0°$; in panel (b) $\theta_0 = 34.05°$. The dielectric function of silver at this wavelength is given by $\varepsilon_2(\omega) = -16.0 + i1.088$. The surface realizations were limited to the area $25\lambda \times 25\lambda$ and discretized on grids of 321×321 points. The surface realizations were characterized by a Gaussian power spectrum with correlation length $a = \lambda/4$ and an RMS height of $\delta = \lambda/40$. The MDRC was averaged over an ensemble of $N_s = 5021$ surface realizations. Here $\alpha \to \beta$ denotes β-polarized incident light scattered into α-polarized light. The vertical dashed lines denote the angle of specular and retro-specular direction of scattering, $\pm\theta_0$, respectively.

constructively in the anti-specular direction with light scattered by a reciprocal process. This phenomenon was first predicted in 1985 by a theoretical perturbation study [34], and was shortly after confirmed experimentally in 1987 [35]. These peaks can be clearly discerned in Figs. 4(a) and 4(b) for $p \to p$ scattering, where the coupling to SPPs is stronger.

The full angular distribution of the incoherent component of the MDRC for the vacuum-glass interfaces as a function of $\boldsymbol{q}_\parallel$, is presented as color contour plots for the polar angle of incidence $\theta_0 = 0.0°$ in Fig. 5; $\theta_0 = 34.05°$ in Fig. 6 ($\phi_0 = 0.0°$ for both cases). Here and in the following contour plots, the origin corresponds to the polar angle of scattering $\theta_s = 0.0°$ and the edge, where $q_\parallel = \omega/c$, to $\theta_s = 90.0°$. The direction of specular reflection is shown as a white spot in the plots. For a visual geometrical reference of the directions and scattering angles $\boldsymbol{q}_\parallel$ corresponds to, the reader is directed to Fig. 1.

The figures contain 9 sub-figures labeled (a)–(i) which depict the MDRC for various polarizations of incident and scattered light. The first and second column from the left (Figs. 5(a),(d),(g) and 5(b),(e),(h), respectively), the incident light is p- and s-polarized, respectively. In the third column (Figs. 5(c),(f),(i)) the incident light is unpolarized, which is denoted by " $\circ$ ". In the first row from the top (Figs. 5(a)–(c)) the polarization of the scattered light is not recorded, which is indicated by " $\star$ ". In the second and third row

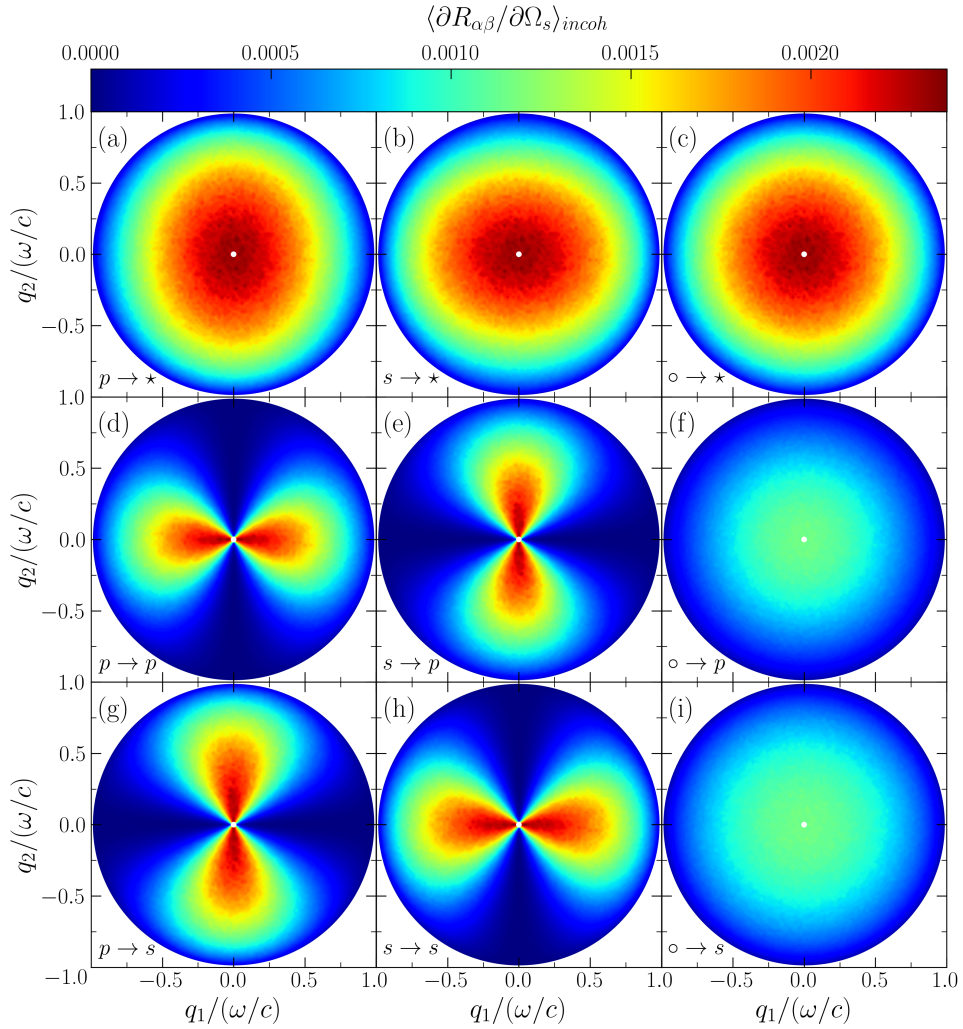

Figure 5: The full angular distribution of the incoherent component of the MDRC (42), for light scattered by a rough interface separating vacuum from glass, as functions of the lateral wave vector $\boldsymbol{q}_\parallel$. The angles of incidence are $(\theta_0, \phi_0) = (0.0°, 0.0°)$. The parameters are the same as for Fig. 3. In panels (c),(f) and (i) the "$\circ$" denotes that the incident light is unpolarized, while "$\star$" in panels (a)–(c) denotes that the polarization of the scattered light was not recorded. The white spot indicates the position of specular reflection ($\boldsymbol{q}_\parallel = \boldsymbol{k}_\parallel$).

from the top (Figs. 5(d)–(f) and 5(g)–(i), respectively), the light scattered into p and s-polarized light is shown, respectively.

The $\circ \to \alpha$ subplots were obtained by taking the sum of the co- and cross-polarized MDRC's for α polarized scattered light divided by 2. Similarly, the $\beta \to \star$ subplots were obtained by taking the sum of the co- and cross-polarized MDRC's for β polarized incident light. By combining the two methods described above, the $\circ \to \star$ subplots were obtained by summing the four MDRC's for $\alpha, \beta = p, s$ and dividing by 2. Simply put, the third column from the left is the sum of the two first columns divided by two, and the first row from the top is the sum of the second and third row.

A strong angular dependence is observed for both polar angles of incidence. All of the plots show that the light scattered incoherently is distributed symmetrically along the plane of incidence. For normal incidence, shown in Fig. 5, we observe that on average the

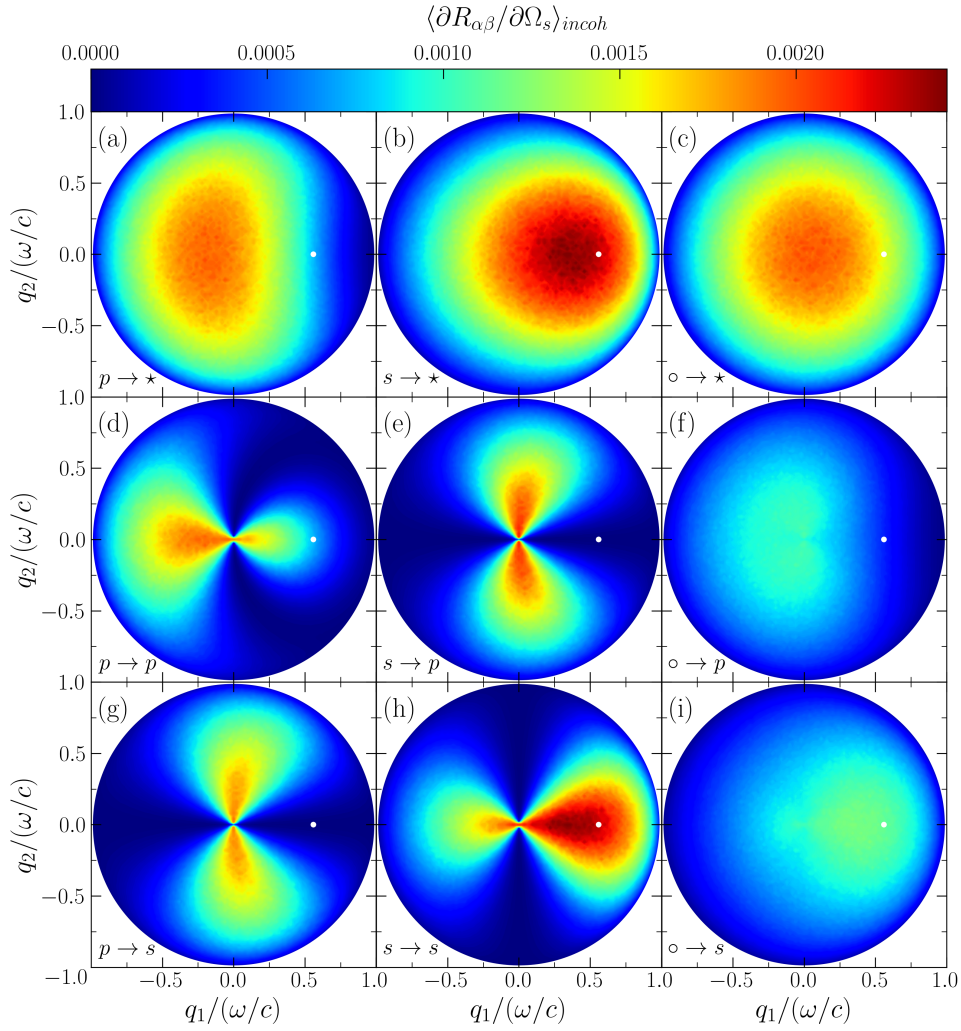

Figure 6: The same as in Fig. 9, except that $\theta_0 = 34.05°$.

co-polarized light (Figs. 5(d),(h)) is scattered in the plane of incidence, while the cross-polarized light (Figs. 5(e),(g)) is scattered predominantly perpendicular to the plane of incidence. Both the co- and cross-polarization distributions show a dipole-like pattern in the angular distribution. For co-polarization the dipole-like angular dependence is oriented along the q_1q_3-plane, while for cross-polarization it is oriented along the q_2q_3-plane. The angular distributions show mirror symmetries about the q_1q_3- and q_2q_3-plane for all polarization's of scattered and incident light. In Figs. 5(a)–(c), where the polarization of the scattered light is not recorded, it can be seen that the angle-dependent scattering is for the most part isotropic, except for a minor anisotropy along the q_2 and q_1 direction for $p-$ and $s-$polarized incident light, respectively. This anisotropy is a result of the intensity distribution being wider in the direction perpendicular to the direction of the incident electric field, in comparison to the distribution in the direction along it. When the incident light is unpolarized (Figs. 5(c),(f),(i)) the distributions are isotropic. It is observed that s-polarized scattered light is distributed over a wider range of scattering angles than the p-polarized light.

The patterns observed for normal incidence continue for higher angles of incidence, which is depicted in Fig. 6 for $\theta_0 = 34.05°$. Many of the symmetries observed in the

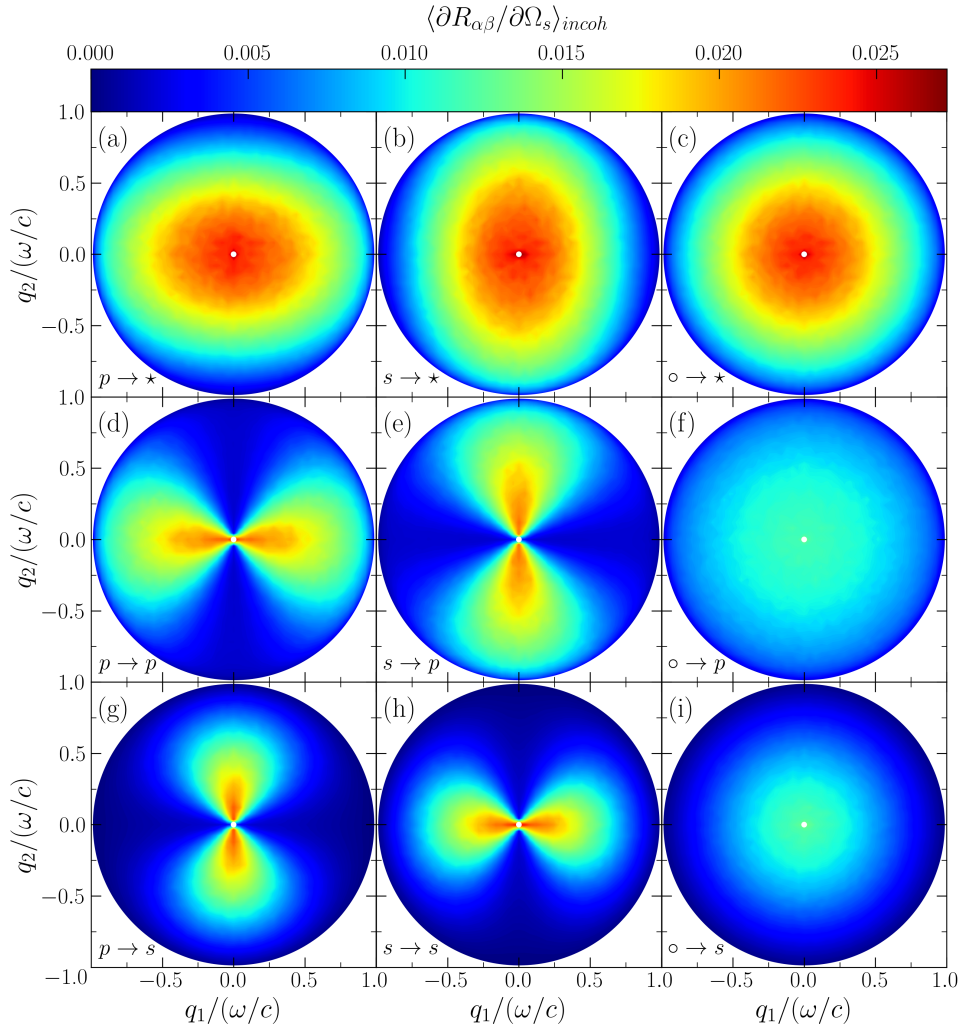

Figure 7: The full angular distribution of the incoherent component of the MDRC (42) for light scattering from a rough interface between vacuum and silver as a function of the lateral wave vector $\boldsymbol{q}_\parallel$. The angles of incidence are $(\theta_0, \phi_0) = (0.0°, 0.0°)$. The parameters are the same as for Fig. 4. In panels (c),(f) and (i) the "$\circ$" denotes that the incident light is unpolarized, while "$\star$" in panels (a)–(c) denotes that the polarization of the scattered light was not recorded. The white spot indicates the position of specular reflection ($\boldsymbol{q}_\parallel = \boldsymbol{k}_\parallel$).

distributions for normal incident light, no longer hold for non-normal incidence. Here, the only remaining symmetry is the mirror symmetry about the plane of incidence. The dipole pattern is still present, however, it is stronger in some directions and weaker in others. For instance, the co-polarized distribution for p-polarized incident light is more intense in the backwards scattering direction ($q_1 < 0$) and weaker in the opposite direction ($q_1 > 0$). The opposite behavior is observed for $s \to s$ polarization. For cross-polarization the distributions are stronger in the forwards scattering direction for both s- and p-polarized incident light; this trend escalates for even higher polar angles of incidence. The slight anisotropy observed for unrecorded polarization of scattered light is still present.

The full angular distribution of the MDRC for vacuum-silver interfaces is presented in Figs. 7 and 8 for normal and non-normal incidence, respectively. Most of the observations made for the vacuum-glass surface hold here as well and will therefore not be repeated.

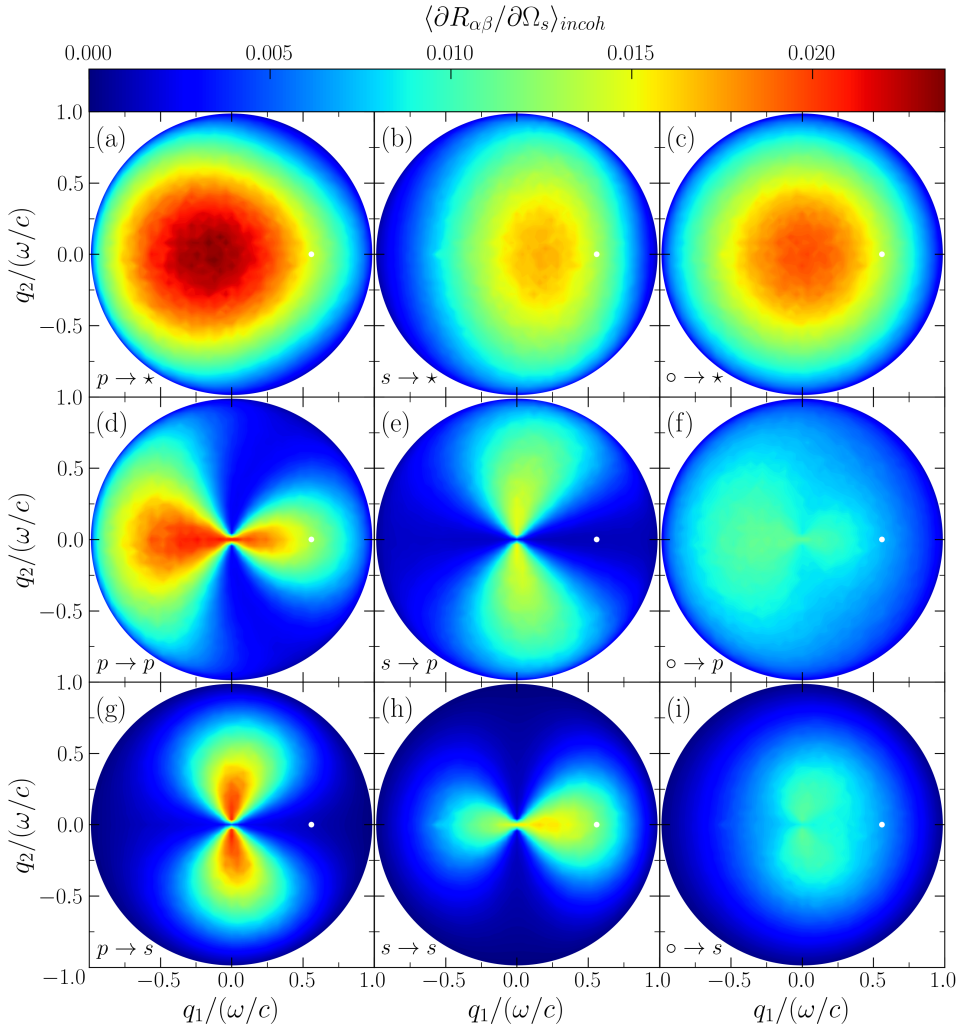

Figure 8: The same as in Fig. 11, except that $\theta_0 = 34.05°$.

The main difference between the distributions of the glass and silver surfaces, is that the anisotropy observed in the $\beta \to \star$ distributions is reversed for the silver surface. Here the intensity distributions are wider along the direction of the incident electric field, in comparison to the distribution in the direction perpendicular to it. It is also observed that the intensity is higher for p-polarized incident light than s-polarized incident light for non-normal incidence. Consequently, the distributions for unpolarized incident light, when the polarization of the scattered light is recorded ($\circ \to \alpha$), are different. The areas which had little to no contribution in the MDRC of the glass surface, have a noticeable contribution here from multiple-scattering. The enhanced backscattering peak can be discerned in Fig.8(h), where it has not been obscured by the background scattering.

4.1.2 The Mueller matrix

The Mueller matrix, for the light scattered incoherently by the vacuum-glass and vacuum-silver systems, was calculated from Eqs. (44) and (47) on the basis of the reflection amplitudes obtained from the simulations. The full angular distribution of the Mueller matrix for the glass surface can be seen as a function of $\boldsymbol{q}_{\parallel}$ in Figs. 9 and 10 for the angles of incidence $(\theta_0, \phi_0) = (0.0°, 0.0°)$ and $(\theta_0, \phi_0) = (34.05°, 0.0°)$, respectively.

To emphasize the polarization effects of the surface, the Mueller matrices have been normalized with respect to the first element M_{11}, using Eq. (46). Since M_{11} only contains the intensity distribution of the scattered light, which is available and has already been studied through the MDRC of the surface, no essential information has been lost. Consequently, the first element equals unity in all directions under this formalism. The elements are organized in the matrix format, where the first element m_{11} is located in the upper left corner (Fig. 9(a)), m_{12} is located in the first row and second column (Fig. 9(b)), etc.

For the glass surface under normal incidence, seen in Fig. 9, a strong angular dependence can be seen in some of the elements. It is observed that the elements $m_{31}, m_{41}, m_{42}, m_{43}, m_{14}, m_{24}$ and m_{34} are effectively zero. The contribution from m_{21}, m_{12}, m_{13} is weak, yet discernible. The elements in the first and last column are circularly symmetric, while the second and third column are symmetric under under 90° rotation and change of sign. The elements in the third column are identical to the ones on the same row in the second column when rotated by 45°. The symmetry relations observed above obey the ones predicted by Bruce [26], to be present in the Mueller matrix for light normally incident onto an isotropic rough surface. Additionally, it is observed that the first and last element m_{11} and m_{44}, respectively, appear to be equal under a change of sign.

The elements can be interpreted by studying Eqs. (44). For example, the m_{12} element, measures the difference between the intensity distributions of the scattered light when the incident light is either p- or s-polarized. By looking at the MDRC we can see that the $\beta \to \star$ distributions are quite similar for both polarizations, see Figs. 5(a) and 5(b). Consequently, this is why the contribution to this matrix element is so small, the contribution comes only from the anisotropies observed earlier between the two MDRC distribution for p- and s-polarized incident light. Conversely, the m_{21} element gives the difference between the intensities of unpolarized light scattered into either p or s polarized light, i.e the difference between Figs. 5(f) and 5(i). The m_{22} element, measures the difference between co- and cross-polarized light. When $m_{22} > 0$ most of the light is co-polarized, and vice versa. This is in perfect agreement with what was observed for the MDRC, the in-plane scattering consists mainly of co-polarization, while the out-of-plane scattering is mainly cross-polarized.

By comparing the Mueller matrix of the glass surface in certain direction to the matrices of known optical devices, we can get more insight into the polarimetric behavior of the surface. For normal incidence it is seen that the matrix has approximately the following form in the q_1q_3-plane:

$$M_R = \begin{bmatrix} 1 & 0 & 0 & 0 \\ 0 & 1 & 0 & 0 \\ 0 & 0 & -1 & 0 \\ 0 & 0 & 0 & -1 \end{bmatrix}, \tag{103}$$

which is the Mueller matrix of an ideal half-wave retarder [36, p. 161] (and an ideal mirror). From looking at the effect this has on the Stokes vector (43), we can interpret the effect it has on the polarization. For linearly polarized light, the quarter-wave plate conserves the polarization and gives the electric field a phase shift of $\Delta\phi = \pi$. It is observed that this matrix results in a 90° rotation of the polarization of the light scattered in-plane when the incident light is ±45° polarized, or a change of handedness if the incident light

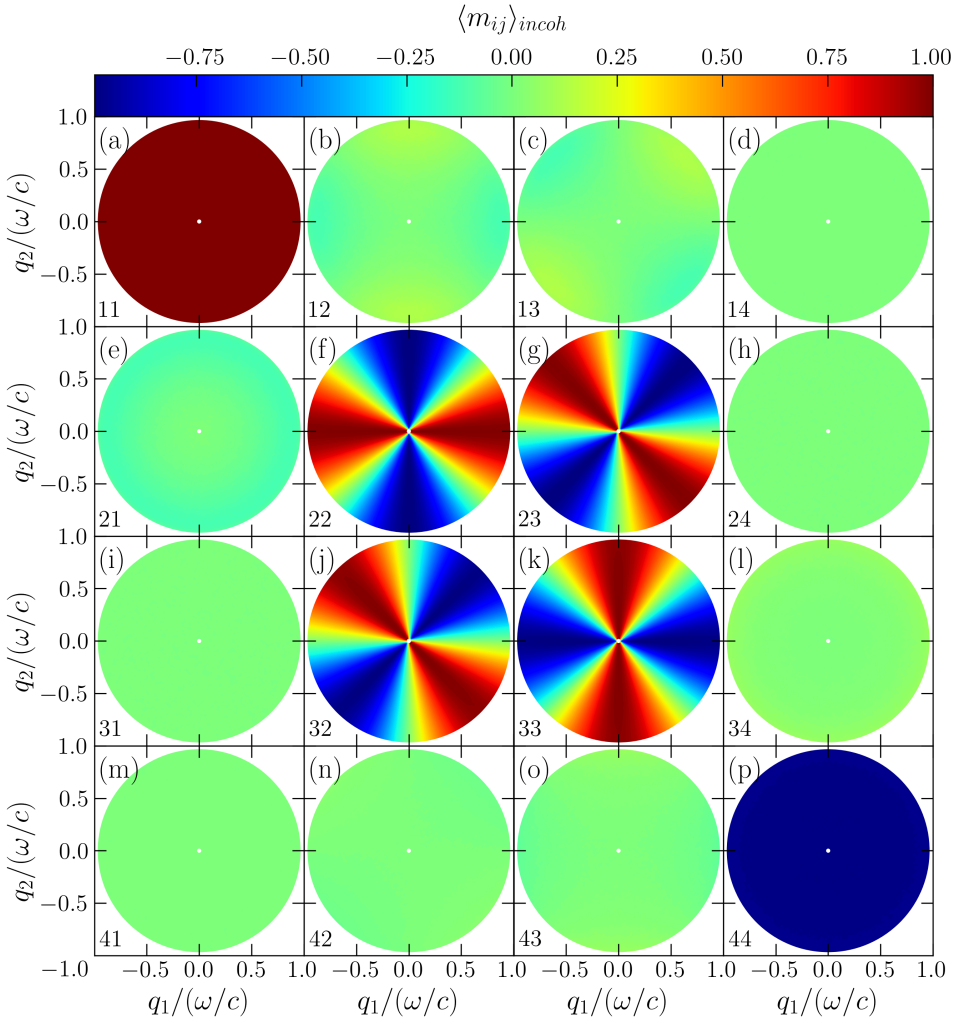

Figure 9: The full angular distribution of the 16 elements of the Mueller matrix (44) from light scattered incoherently by a randomly rough glass surface as a functions of q_1 and q_2. The angles of incidence are $(\theta_0, \phi_0) = (0.0°, 0.0°)$. The parameters are the same as for Fig. 5. The elements $\langle m_{i,j}\rangle$ (i,j = 1,2,3,4) are organized as a matrix, where i and j denote the row numbered from the top and the column numbered from the left, respectively. The elements are normalized with respect to the first element $\langle M_{1,1}\rangle$ (a). The white spots indicate the specular direction of reflection.

is circularly polarized. In the q_2q_3-plane the matrix reads approximately

$$M'_R = \begin{bmatrix} 1 & 0 & 0 & 0 \\ 0 & -1 & 0 & 0 \\ 0 & 0 & 1 & 0 \\ 0 & 0 & 0 & -1 \end{bmatrix}, \tag{104}$$

which is the product between an optical rotation Mueller matrix and a half-wave plate

[36, pp. 164–165], i.e.

$$M_R M_{rot}(\theta) = \begin{bmatrix} 1 & 0 & 0 & 0 \\ 0 & 1 & 0 & 0 \\ 0 & 0 & -1 & 0 \\ 0 & 0 & 0 & -1 \end{bmatrix} \begin{bmatrix} 1 & 0 & 0 & 0 \\ 0 & \cos(2\theta) & \sin(2\theta) & 0 \\ 0 & -\sin(2\theta) & \cos(2\theta) & 0 \\ 0 & 0 & 0 & 1 \end{bmatrix} = \begin{bmatrix} 1 & 0 & 0 & 0 \\ 0 & \cos(2\theta) & -\sin(2\theta) & 0 \\ 0 & -\sin(2) & -\cos(2\theta) & 0 \\ 0 & 0 & 0 & -1 \end{bmatrix}, \tag{105}$$

for $\theta = 90°$, i.e. the polarization is rotated 90° and the scattered electric field obtains a phase shift of π. The matrix describes that β-polarized incident light scattered out-of-plane will be cross-polarized, and that circular polarized light scattered out-of-plane will change handedness. It is observed that the Mueller matrix in Fig. 9 behaves very similarly to the matrix Eq. (105) for all $\theta = \phi_s$. To test this observation, Eq. (105) was calculated as a function of $\phi_s(q_1, q_2) = \arctan2(y, x)$, which can be seen in Appendix A, along with the definition of the $\arctan2(y, x)$ function. There it can be seen that the plot of Eq. (105) is almost identical to Fig. 9.

In the Mueller matrix of the glass surface for non-normal incidence, which can be seen in Fig. 10 for the polar angle of incidence $\theta_0 = 34.05°$, most of the symmetries disappear. The elements m_{23} and m_{32} appear to still be identical, while m_{22} and m_{33} no longer appear to be equal under a change of sign. The m_{13} and m_{31} elements are no longer zero, and in fact they are almost identical, both show significant contributions in different directions.

The contribution from the m_{21} and m_{12} elements is stronger than what was observed for normal incidence, they also appear to be near identical. The contribution is located mainly in the forward scattering direction and is negative. This is because the intensity of $s \to \star$ and $\circ \to s$ scattering dominates the forward scattering in the MDRC for non-normal incidence. The opposite is true for p-polarization, which is why we see a positive contribution in the backwards scattering direction.

The transpose of the first row is observed to be near identical to the first column, which was not the case for normal incidence. Additionally, it is observed that m_{44} no longer equals $-m_{11}$ in the forward scattering direction. All the elements except m_{44} in the last column and last row are still zero. Overall, the polarimetric behavior is observed to be more complex than the one described by Eq.(105), making the matrix much harder to decompose into simpler optical operations as was done for normal incidence.

The Mueller matrices of the vacuum-silver surface can be seen in Figs. 11 and 12 for normal and non-normal incidence, respectively. For normal incidence the same symmetry relations are observed , except that $m_{44} \neq -m_{11}$. The diagonal elements and the central block elements of the matrix are very similar to the ones for the glass surface. However, many of the elements which were zero for the glass surface have a noticeable contribution for the silver surface. In particular, the m_{21} element has a very strong contribution for very high polar scattering angles. Since this contribution is positive it means that there is a higher presence of p-polarized scattered light for large polar scattering angles according to Eq. (44).

The central 2×2 block of the Mueller matrix, which is related to rotations [36, pp. 165–166], is almost identical to what was observed in the Mueller matrix for the Gaussian-correlated glass surface. Additionally, the last row and column, shows visible contributions

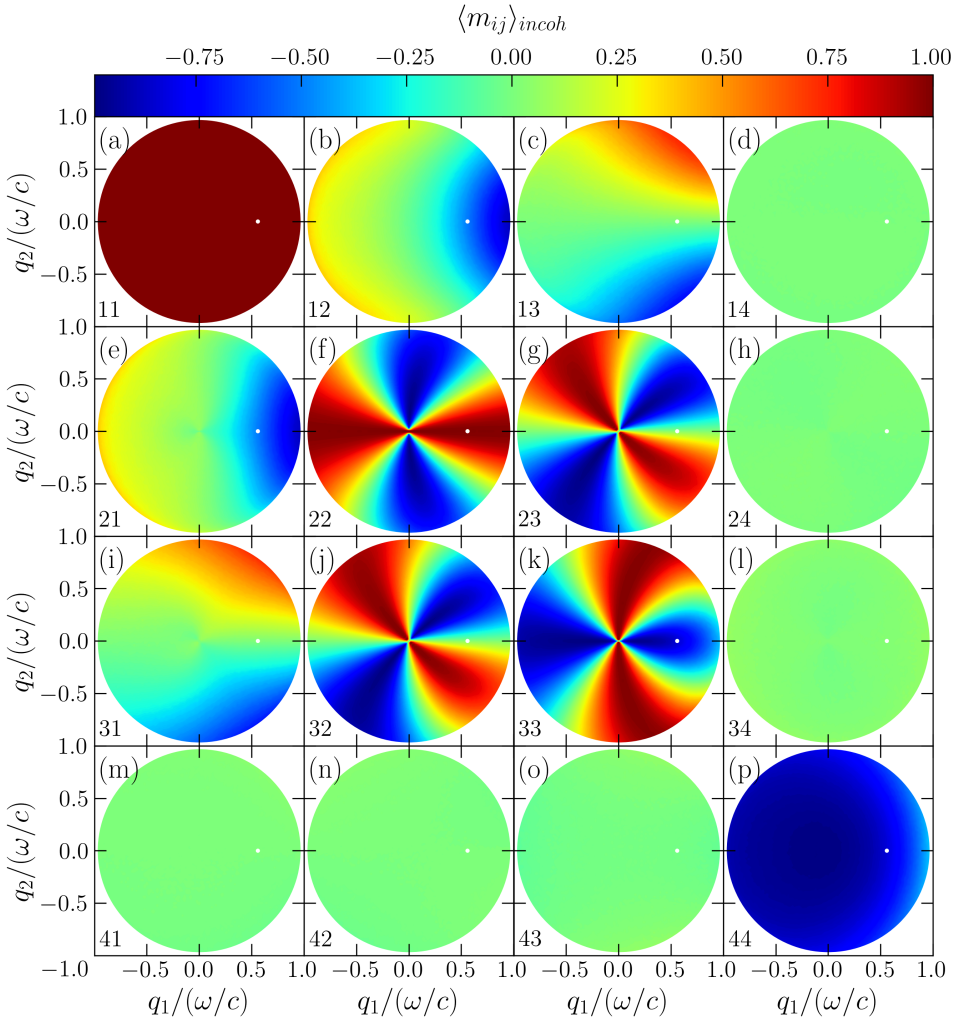

Figure 10: The same as in Fig.9, except that $\theta_0 = 34.05°$.

in some of the elements which was not present in the vacuum-glass case. This is especially visible in m_{34} and m_{43} in the lower right block of the matrix, which are related to retardation [36, pp. 165–166].

For non-normal incidence seen in Fig. 12, the symmetries disappear again. The central block and diagonal is still very similar to what was observed for glass. The other elements are still very different compared to the glass case. The transpose of the first row does not resemble the first column, as it did for the Gaussian-correlated glass surface. The contrast between normal and non-normal incidence is not as strong for the silver surface as it was for the glass surface. The distributions are very similar to the ones for normal incidence except for some distortions. However, noticeable contributions can be seen in the m_{31} and m_{24} elements which were not present under normal incidence.

By performing various decomposition's of the Mueller matrices it is possible to obtain a more phenomenological description of the scattering systems. Several effects can then be quantified such as the *diattenuation*, *retardance* and *depolarization* [36, pp. 178–192]. However, due to time constraints, a more detailed study of the Mueller matrices will not be included in this work.

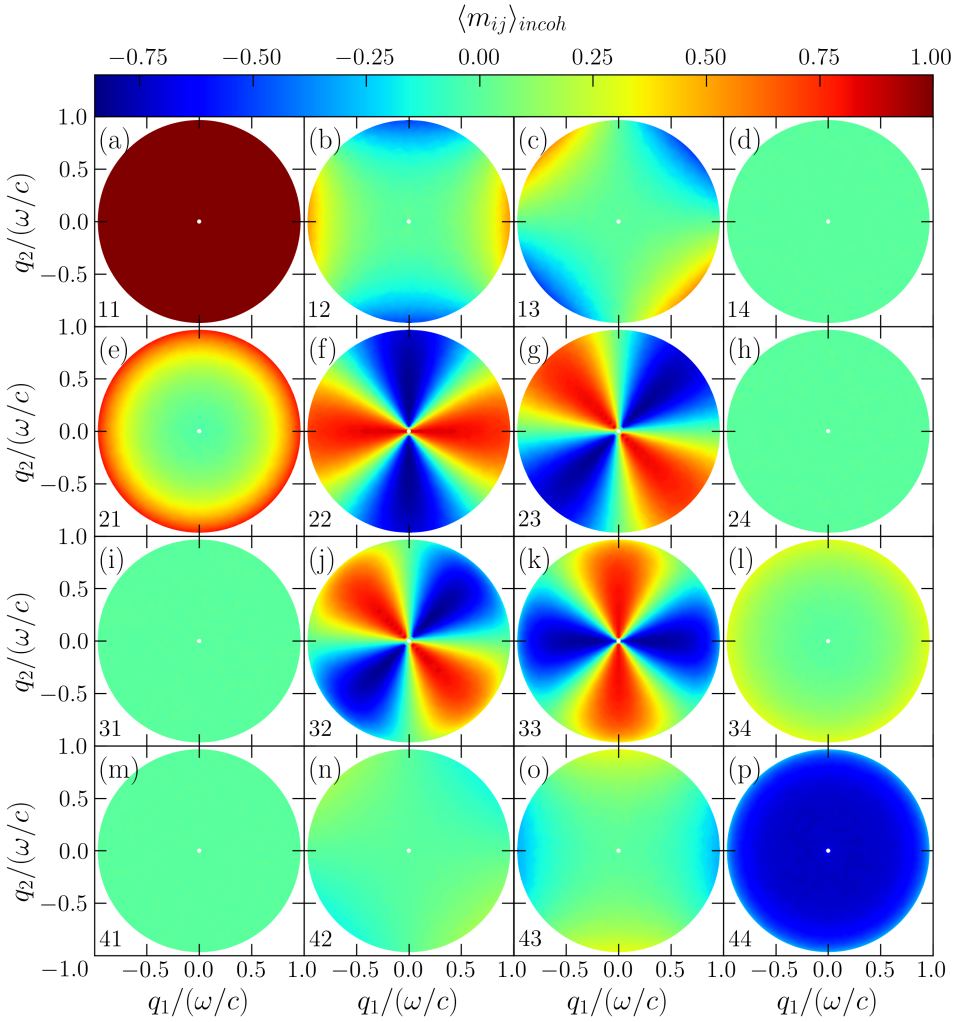

Figure 11: The full angular distribution of the 16 elements of the Mueller matrix (44) from light scattered incoherently by a randomly rough silver surface as a functions of $\boldsymbol{q}_\parallel$. The angles of incidence are $(\theta_0, \phi_0) = (0.0°, 0.0°)$. The parameters are the same as for Fig. 7. The elements $\langle m_{i,j}\rangle$ (i,j = 1,2,3,4) are organized as a matrix, where i and j denote the row numbered from the top and the column numbered from the left, respectively. The elements are normalized with respect to the first element $\langle M_{1,1}\rangle$. The white spots indicate the specular direction of reflection.

4.1.3 The reflectivity and reflectance for directional illumination

The reflectivity of the Gaussian-correlated glass surface was calculated as a function of the incident angle θ_0 and is presented in Fig. 13. Here we can see the reflectivity of both unpolarized and linearly polarized incident light, which were obtained from Eqs. (58) and (57), respectively. Note that the resolution becomes weaker with increasing angles, and that the reflectivity for $\theta_0 = 90°$ is not resolved. This is because $\boldsymbol{q}_\parallel$, which is evenly discretized along each axis, is proportional to $\sin\theta_s$. As expected the reflectivity for p-polarized incident light is zero at the Brewster angle $\theta_0 \approx 56°$, since only light scattered coherently contributes to the reflectivity.

The reflectance under directional plane wave illumination was obtained using Eq. (102) and can be seen as a function of the incident angle θ_0 in Fig. 14. Here the values for the

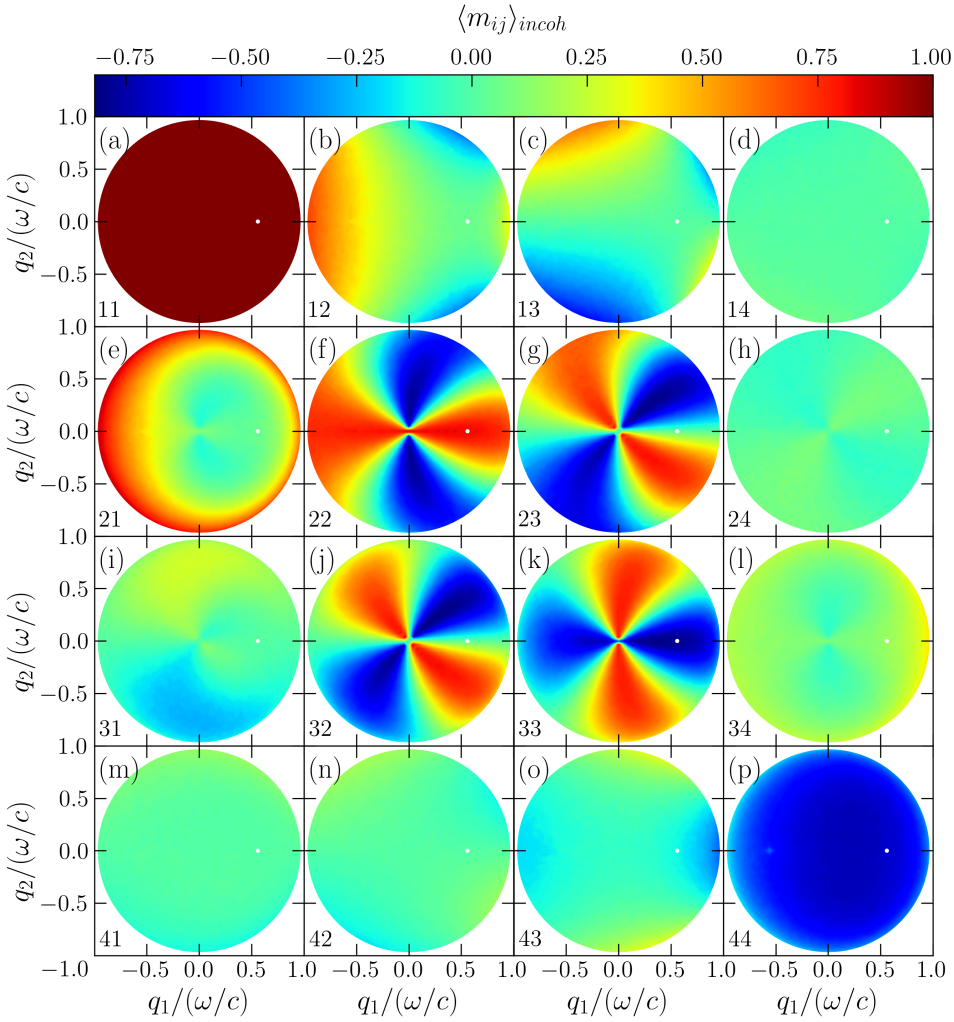

Figure 12: The same as in Fig.11, except that $\theta_0 = 34.05°$.

reflectance can be seen for each angle resolved on the $\boldsymbol{q}_{\parallel_{i,j}}$ grid, along with an interpolation which was calculated with the natural assumption that $\mathscr{R}_\beta(90°) = 1$. The weights $w_{i,j}$ in the discretized integral were obtained from a quadrature scheme for integration over a circular disk domain; for details see Ref. [37].

Here we see that the zero at the Brewster angle for p-polarization has been lifted and that there is a small contribution to the reflectance. This effect is purely caused by light scattered incoherently. Otherwise, the reflectance is almost identical to the reflectivity, which shows that the scattering is still dominated by specular (coherent) scattering; this is expected for weakly rough surfaces such as the one considered here. For a more rough surface, there would be a more prominent difference between the reflectivity and reflectance; to show this the reflectivity and reflectance of a moderately rough surface is displayed in Appendix B, where it can be seen that the differences are more pronounced.

To display the diffuse contribution to the reflectance, the incoherent component of the reflectance for directional illumination is shown in Fig. 15, for both p, s and unpolarized incident light. Here it is observed that the contribution from light scattered incoherently decreases when the angle of incidence θ_0 approaches 90°. The contribution is very weak for directional illumination.

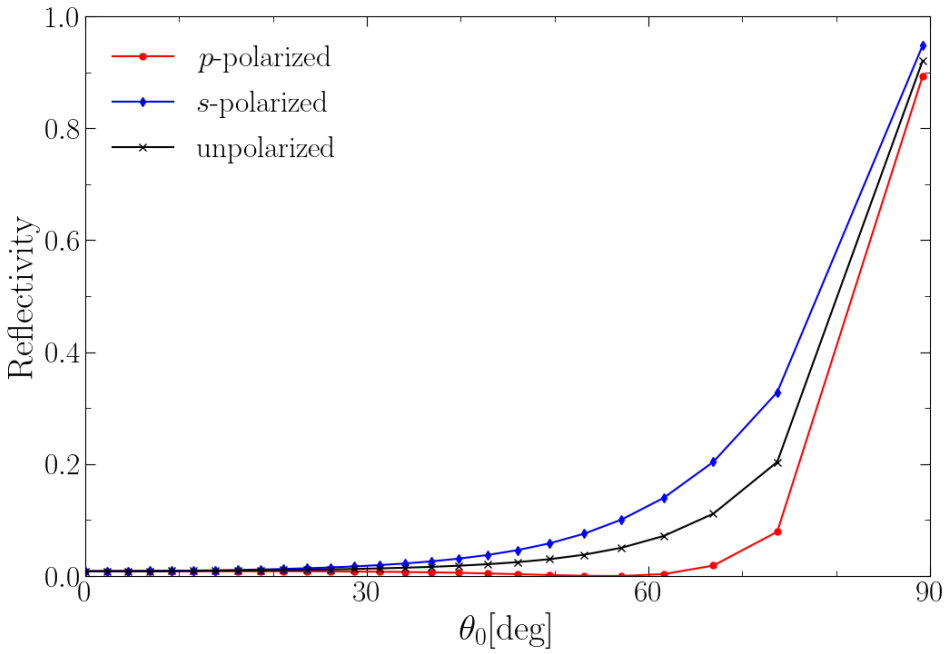

Figure 13: The reflectivity of a randomly rough glass surface as a function of the incident angle θ_0, under directional illumination. The surface is characterized by a Gaussian power spectrum (16) with $a = \lambda/4$ and have a RMS height of $\delta = \lambda/20$. The surface and numerical parameters used were the same as for Fig. 22.

4.1.4 The reflectivity and reflectance for diffuse illumination

To obtain the diffuse-diffuse reflectivity, the reflectivity for directional illumination was multiplied by a weight function $\ell(\theta_0)$ and integrated over all angles of incidence θ_0. The weight function considered in this work was the Lambertian weight function for ideal diffuse hemispherical illumination given by Eq. (72). More realistic weight functions would be easy to incorporate numerically, however, the focus of this work will be on the Lambertian limit as it was considered to be the most useful reference.

Despite that $\ell(\theta_0)$ tends to zero for increasingly higher angles of incidence, the reflectivity for these angles is relatively high. The polar angular region $60-90°$ has a significant contribution to the integration, therefore, a low resolution in this region is problematic. To mitigate the loss of resolution for the higher angles, the reflectivity had to be estimated for more angles of incidence near 90°. Using the fact that the reflectivity should be unity for $\theta_0 = 90°$, the reflectivity was interpolated using a 5th order spline interpolation from normal to 90° incidence. To ensure that the interpolation was well behaved a simple test was conducted; the Fresnel reflectance equations [14, pp. 411–412], were sampled at the same angles as the simulation results and interpolated; then the interpolation was compared to the analytical Fresnel reflectance as a function of θ_0, for both p- and s-polarized incident light. The resulting interpolations were found to be indistinguishable from the Fresnel functions. The interpolated reflectance of the rough surface is shown as a dotted line in Fig.14, where it can be seen that the interpolation is in good agreement with the data points.

The diffuse-diffuse reflectance (reflectivity) of a flat surface under hemispherical Lam-

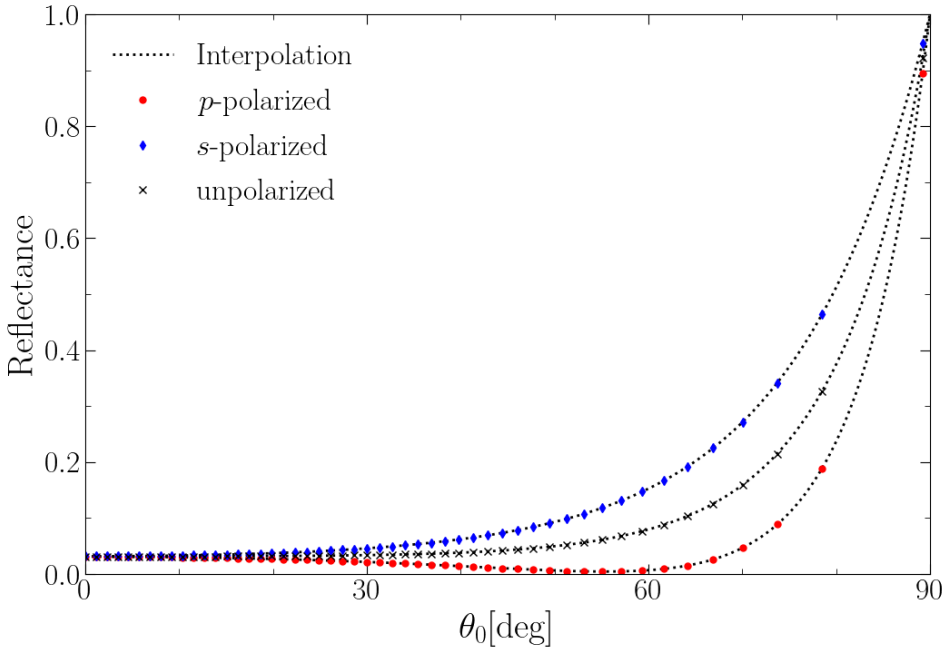

Figure 14: The reflectance of a randomly rough glass surface as a function of the incident angle θ_0, under directional illumination. The surface and numerical parameters used in the simulations are the same as for Fig. 13. The dotted line shows a 5th order spline interpolation of the reflectance results.

bertian illumination can be seen in Tab. 1. The values for s- and p-polarized incident light

$\mathscr{R}_s$	$\mathscr{R}_p$	$\mathscr{R}$
0.146667	0.036889	0.091778

Table 1: The diffuse-diffuse reflectance (reflectivity) of a flat glass surface, under hemispherical Lambertian illumination.

were obtained by numerically integrating the Fresnel equations [14, pp. 411–412], using $\ell(\theta_0)$ as a weighting factor, over all polar angles of incidence. For unpolarized incident light, the diffuse-diffuse reflectance was obtained from an analytical evaluation of the integral in Eq.(70) carried out by Walsh [38]; the resulting equation from this evaluation can be seen in Ref. [39]. Since the reflectivity and reflectance are the same for flat surfaces, the results for a flat surface will be used as a reference for comparison with both the reflectance and reflectivity of rough surfaces.

The interpolated reflectivity of the rough surface was integrated with a 95th degree augmented Gaussian quadrature scheme, for more details see Ref. [40]. The precision of the integration was tested by integrating the Fresnel reflectance, which was sampled at the same angles as the results and then interpolated. The numerical values obtained for $\mathscr{R}_s$ and $\mathscr{R}_p$ were then used to calculate the reflectance for unpolarized incident light using $\mathscr{R} = (\mathscr{R}_s + \mathscr{R}_p)/2$, which was compared to the analytically obtained value presented in Tab. 1. The resulting reflectance was found to deviate from the analytically obtained value

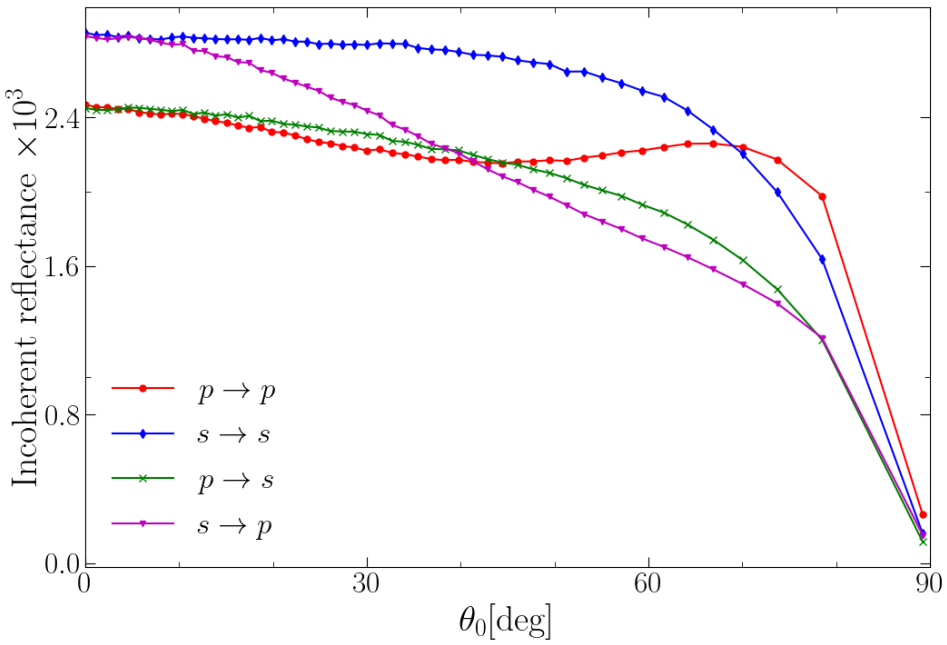

Figure 15: The incoherent component of the reflectance as a function of the incident angle (62) for a randomly rough glass surface, under directional plane wave illumination. The parameters are the same as for Fig. 14.

by only 0.001%.

The reflectivity for a randomly rough glass surface illuminated by hemispherical Lambertian illumination can be seen for s-, p- and unpolarized light in Tab. 2.

$\mathcal{R}_s$	$\mathcal{R}_p$	$\mathcal{R}$
0.124295	0.032497	0.078396

Table 2: The diffuse-diffuse reflectivity of a rough 2D glass surface, under diffuse Lambertian illumination (73). The characterization of the surface and the numerical parameters are the same as in Fig. 3(a).

By performing the same steps as for the reflectivity, the reflectance of a diffusely illuminated Gaussian-correlated glass surface was calculated, and is shown in Tab. 3 for p, s and unpolarized incident light.

$\mathscr{R}_s$	$\mathscr{R}_p$	$\mathscr{R}$
0.128928	0.036749	0.082839

Table 3: The diffuse-diffuse reflectance of a randomly rough 2D glass surface, under hemispherical Lambertian illumination (70). The characterization of the surface and the numerical parameters are the same as in Fig. 3(a).

Compared with the results for a flat surface, we can see a significant decrease in both

the reflectivity and reflectance. In the study for one-dimensional randomly rough surfaces [7], it was found that the reflectance can increase for rough glass surfaces with correlation lengths shorter than the wavelength of the incident light. However, here it is observed that the reflectance has decreased for the correlation length $a = \lambda/4$. The results presented here are more similar to the 1D results with $a \geq \lambda$, rather than $a < \lambda$. Why this is the case is currently not fully understood.

It was also shown for 1D surfaces [7], that the decrease in reflectance can be enhanced when the roughness is increased. To study how an increase in surface roughness affects the diffuse-diffuse reflectance of 2D surfaces, several simulations were performed using various roughness parameters. In Fig. 16 the reflectance of Gaussian-correlated glass surfaces can be seen as a function of the RMS-slope, δ_s, for different correlation lengths, a. For surfaces with isotropic Gaussian power spectra, the RMS-slope along each axis is given by [3, p. 8]

$$\delta_s = \sqrt{2}\frac{\delta}{a}, \tag{106}$$

where δ is the RMS-height of the surface. The RMS-slope will be used here as a measure of the degree of roughness. In Fig. 16 the correlation lengths were held constant while δ was increased.

The simulations presented here were all performed at a lower resolution to reduce the computational cost. The number of discretization points along each axis was $N_x = 321$ and the surface lengths were set to $L = 25\lambda$. The number of polar angles resolved with these parameters was $N_\theta = 26$; with these parameters the angles resolved were also resolved by the high resolution simulations. Each simulation was averaged over an ensemble of $N_s = 500$ surface realizations. The quality of the interpolation when using a low angular resolution was assessed in the following way; the high resolution reflectance results, see Fig. 14, were sampled at the same angles as the low resolution results; then the sampled reflectance was interpolated and used to obtain the diffuse-diffuse reflectance with Eqs. (70) and (102); the calculated reflectance was then compared to the results obtained with high resolution presented in Tab. 3. Performing the interpolation with fewer angles resulted in the final integration to be accurate to the third decimal point with respect to the high resolution results, which was deemed acceptable. The interpolated directional reflectance of one of the low resolution simulations can be seen in Fig. 38 in Appendix B, where it is shown that the interpolation is well behaved.

Correlation lengths larger than 2λ were not achievable, since they require very large surfaces with respect to the wavelength; this would require a considerable amount of discretization points and be too computationally demanding to simulate using the 2D Rayleigh method. Additionally, producing plots for higher correlation lengths would require surfaces with an RMS height above the limit for which the software can produce reliable results. The region of validity of the Rayleigh method for 2D randomly rough surfaces has been mapped for several values of a and δ in [22], which served as a useful guide for determining the right simulation parameters. The limit can be directly observed for several correlation lengths in Fig. 16, where the plots were truncated because the energy conservation criterion was not satisfied for higher values of δ_s. To achieve results for longer correlation lengths more research needs to be conducted using different approaches, for example ones based on the Kirchhoff approximation [41], which are valid when $a \gg \lambda$.

In Fig. 16, several trends are found to be opposite of what was observed for 1D randomly rough surfaces by González-Alcalde et al. [7]. It is observed that for $a > \lambda$ that

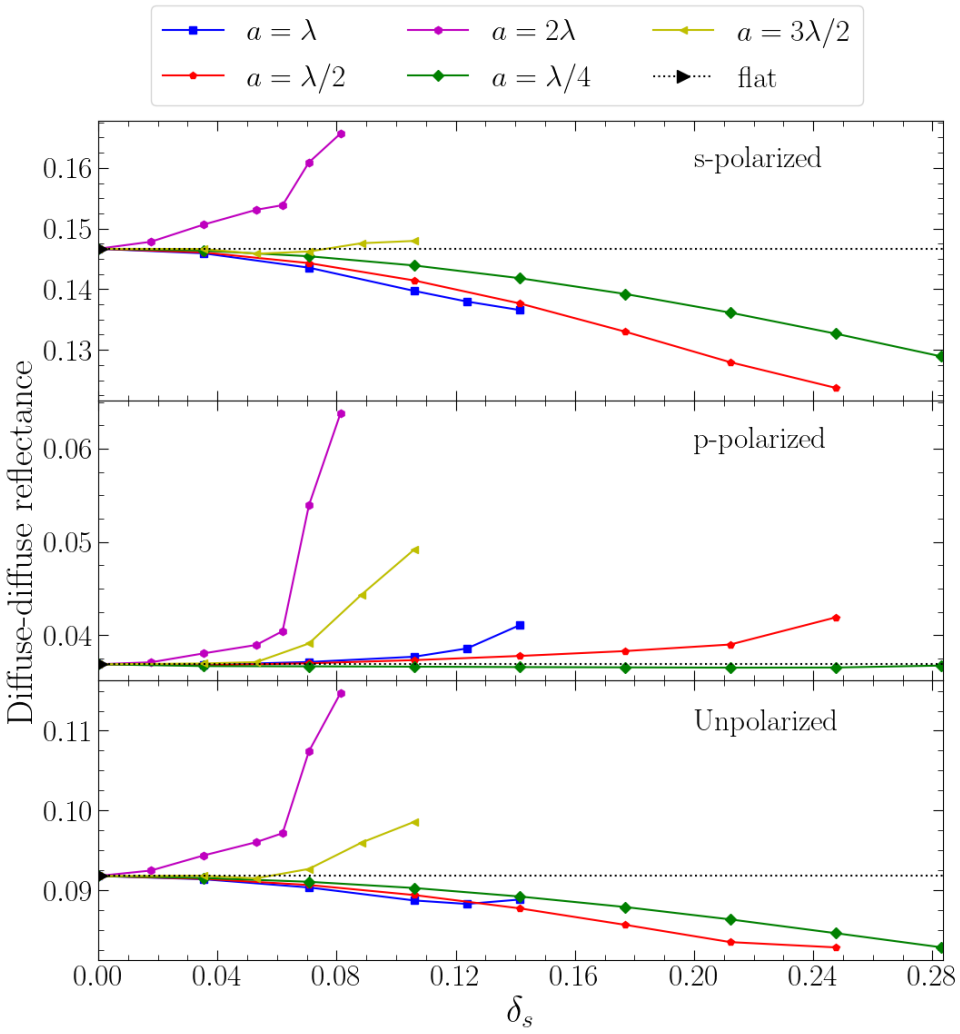

Figure 16: The reflectance of diffusely illuminated rough glass surfaces as a function of the RMS slope for different correlation lengths a. The surfaces were characterized by Gaussian correlation functions (16). The results for s-, p- and unpolarized incident light are shown in order from the top. The results for flat surfaces are denoted by the black triangles and dashed lines. The results were averaged over ensembles of $N_s = 500$ surface realizations.

the diffuse-diffuse reflectance for both s and p-polarized incident light increases along with the roughness, whereas for 1D surfaces it was found to steadily decrease for both polarizations. The exception to this trend is the small decrease at first in $\mathscr{R}_s$ for $a = 3\lambda/2$, which then reverses for higher δ_s. For $a = 2\lambda$ the increase is extreme for p-polarized incident light at the highest achievable RMS slopes. At these points the energy conservation criterion is satisfied within 1%. This small deviation from unity is expected to have an insignificant effect on the directional reflectance; however, the total contribution from integrating over all polar angles of incidence can be high enough to affect the results for the diffuse-diffuse reflectance. Therefore, the diffuse-diffuse reflectance should not be treated as exact for the highest achievable RMS slopes and one should keep in mind that there is a margin of uncertainty. Nonetheless, these results are still considered to be good indications of the expected trends.

For correlation lengths $a \leq \lambda$, the results for $\mathscr{R}_s$ decrease when the roughness is progressively increased. When the incident light is p-polarized, the correlation lengths $\lambda \geq a \geq \lambda/2$ yield an increase in the reflectance which was not observed for 1D surfaces; for $a = \lambda/4$ there is a negligible decrease when δ_s is increased. The diffuse-diffuse reflectance of 1D surfaces was found to have a tendency to increase for $a < \lambda$ and decrease for $a \geq \lambda$, for all polarizations; while for 2D surfaces the trends are observed to depends strongly on the polarization of the incident light when $a \leq \lambda$. The dependence of the diffuse-diffuse reflectance on δ_s is observed to be weaker for shorter correlation lengths, which was also observed for 1D surfaces.

To explain these differences observed between $1D$ and $2D$ scattering systems will require further research. Due to time constraints, it was unfortunately not possible to address this research within this M.Sc. thesis.

Thus, when the RMS-slope of two dimensional randomly rough glass surfaces is systematically increased, the diffuse-diffuse reflectance is expected to increase for all polarizations of the incident light, when the correlation length is greater than $3\lambda/2$; moreover, the trend is expected to reverse for s-polarized incident light for shorter correlation lengths.

4.2 Isotropic Gaussian-cosine correlated surfaces

In this work we consider two systems with randomly rough surfaces characterized by the Gaussian-cosine auto-correlation function (18). Both systems are isotropic, meaning $a_1 = a_2 = a$, and have a vacuum ambient and a silver substrate. The surface in the first system, denoted by 1, has a correlation length $a = 0.25\lambda$ and RMS height of $\delta = 0.025\lambda$; which is the same as the Gaussian-correlated silver surface presented earlier in Sec. 4.1. The surface in the second system, denoted by 2, has $a = \lambda$ and $\delta = 0.05\lambda$. Both systems have $b = a/2$. In Sec. 4.3 the MDRC for anisotropic Gaussian-cosine correlated surfaces is presented, for the same two systems presented here, except that the correlation lengths in the x_2 direction are doubled, i.e. $a_2 = 2a_1$.

Simulations solving the RRE for reflection were performed for both systems using the same numerical parameters as the Gaussian-correlated silver surface in presented earlier in Sec. 4.1; to remind the reader, the parameters will be repeated again here. The surface realizations were limited to square areas of $25\lambda \times 25\lambda$ and discretized on grids of 321×321 points. The number of discretization points along q_1 and q_2 was then consequently $N_q = 161$ and the upper cutoff in the numerical RRE integral was $\pm\mathcal{Q}/2 = \pm 3.2\omega/c$. The number of polar angles resolved by these parameters was $N_\theta = 26$. The wavelength of the incident light was again chosen to be $\lambda = 632.8\,\text{nm}$, the dielectric function of silver at this wavelength is given by $\varepsilon_2(\omega) = -16.0 + i1.088$ [33].

Demonstrations of the surface profile functions for all of the Gaussian-cosine correlated surfaces considered in this work, both isotropic and anisotropic, can be seen in Fig. 17. Here Figs. 17(a) and 17(b) are realizations of the surfaces used for System 1 and 2, respectively. To be able to compare directly, the anisotropic versions of System 1 and 2 with $a_1 = a$ and $a_2 = 2a$ are shown in Figs. 17(c) and 17(d), respectively.

As there is no known analytical form of the two-dimensional Gaussian-cosine power spectrum , the one used in the Fourier filtering method (see Sec. 3.2) was obtained by a 2D FFT of the auto-correlation function (18). To asses the quality of the Fourier filtering method when using a numerical power spectrum, the auto-correlation function was calculated with the definition given by Eq. (14), where the average was taken over an ensemble of $N_s = 10,000$ surface realizations, and then compared to the analytical form. The calculated correlation function was found to be near identical to the analytical one.

The quality of the simulations was tested for the two systems with the energy conservation test presented in the method section. For the first system it was found that $|\mathcal{U} - 1| \leq 0.004$, i.e., the energy is conserved to within 0.4%. For the second system it was found that $|\mathcal{U} - 1| \leq 0.015$. The RRE was solved for $N_s = 5000$ surface realizations of the Gaussian-cosine correlated surfaces, for both systems; the resulting reflection amplitudes were averaged over this ensemble.

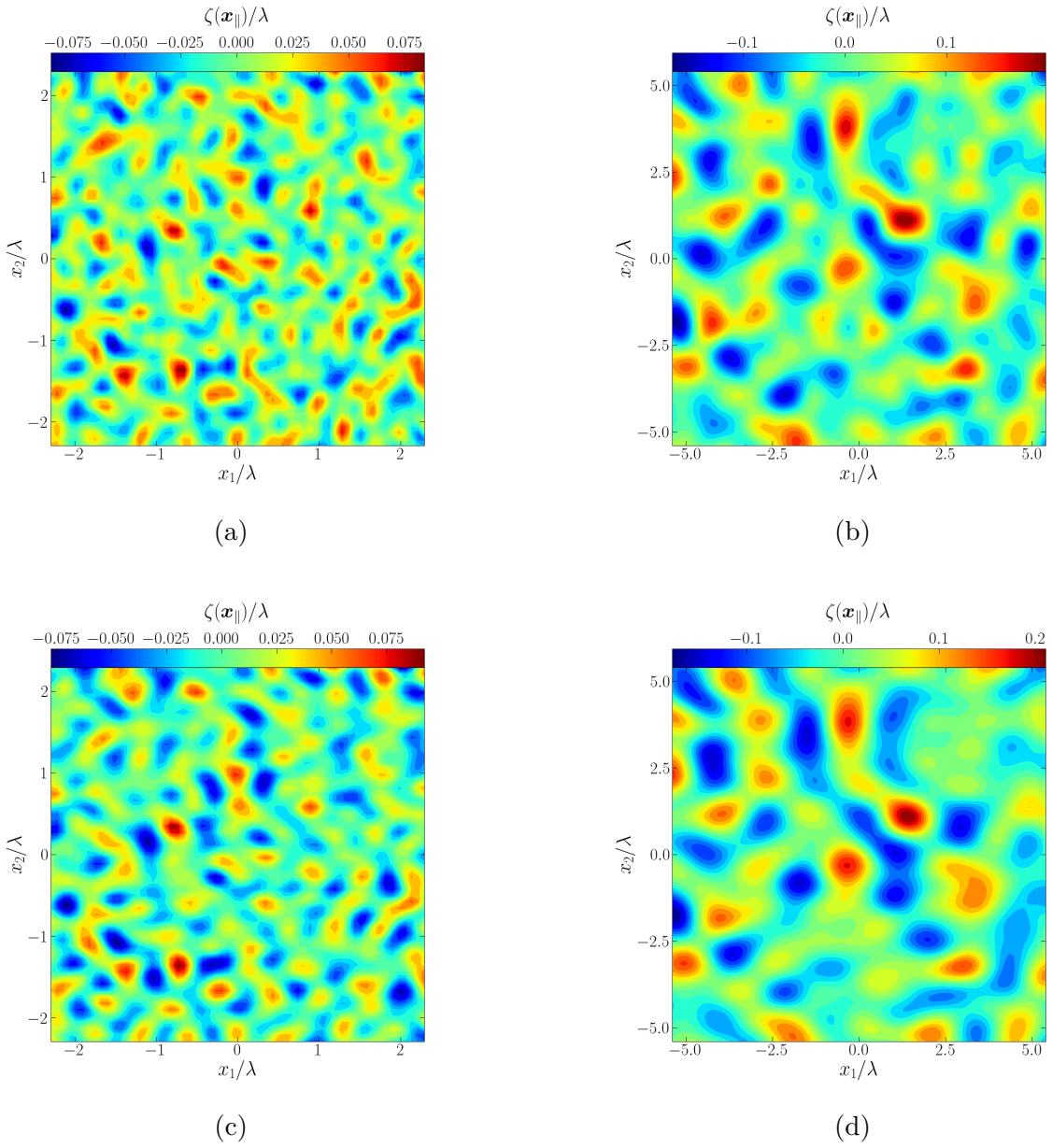

Figure 17: Square segments of numerically generated realizations of the surface profile functions $\zeta(\boldsymbol{x}_\parallel)$ for four different surfaces. All four surfaces are characterized by a Gaussian-cosine correlation function (19), and have the following surface parameters: (a) $a_1 = a_2 = \lambda/4$, $b = a/2$, $\delta = \lambda/40$; (b) $a_1 = a_2 = \lambda$, $b = a/2$, $\delta = \lambda/20$; (c) $a_1 = \lambda/4$, $a_2 = \lambda/2$, $b = a/2$, $\delta = \lambda/40$; (d) $a_1 = \lambda$, $a_2 = 2\lambda$, $b = a/2$, $\delta = \lambda/20$; where a_1 and a_2 are the correlation lengths in the x_1 and x_2 directions, respectively. Furthermore, the root mean square height of the surfaces is denoted by δ and λ is the wavelength of the light incident on the surfaces. The surface realizations were generated with the same uncorrelated random numbers to highlight the differences between isotropic and anisotropic correlation.

4.2.1 The mean differential reflection coefficient

The incoherent component of the MDRC was calculated for both Gaussian-cosine correlated systems using the same methods as before. To be able to compare these results with the ones obtained for the Gaussian-correlated surfaces, the results are presented for the same angles of incidence as used in Sec.4.1.

The in-plane cuts ($\phi_s = \phi_0$) of the MDRC for System 1 are shown in Fig. 18 for normal incidence $(\theta_0, \phi_0) = (0.0°, 0.0°)$, and in Fig. 19 for $(\theta_0, \phi_0) = (34.05°, 0.0°)$.

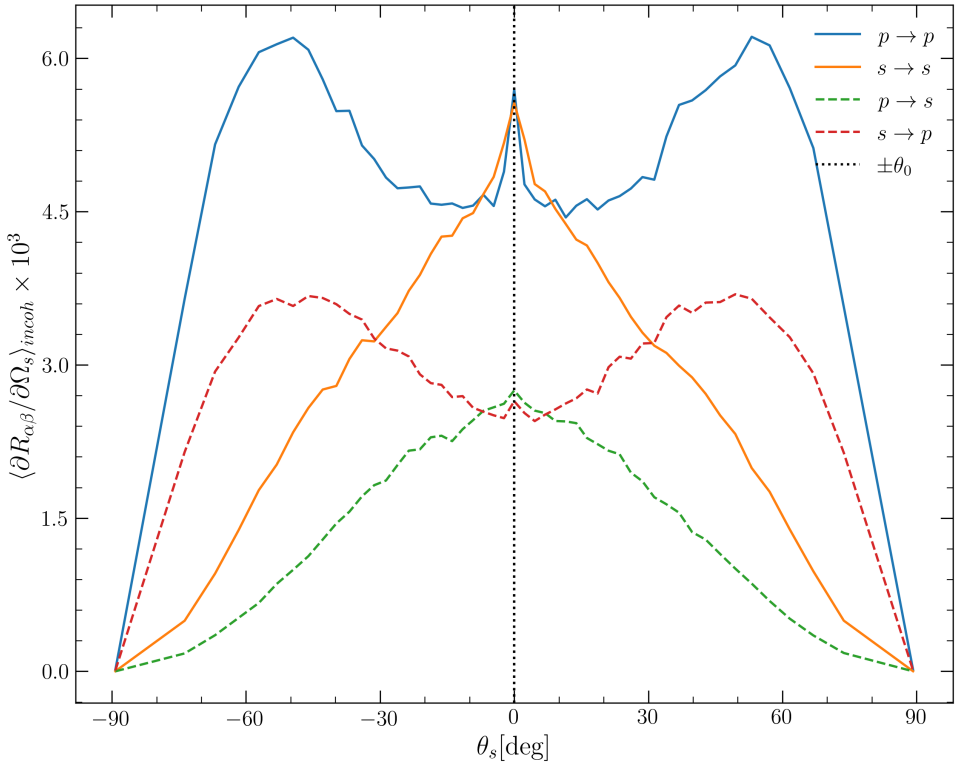

Figure 18: The incoherent component of the MDRC (Eq. (42)) for in-plane scattering from a randomly rough interface between vacuum and silver as a function of the scattering angle θ_s. The wavelength of the incident light (in vacuum) was $\lambda = 632.8\,\text{nm}$ and the polar angle of incidence was $\theta_s = 0.0°$, the dielectric function of silver at this wavelength is $\varepsilon_2(\omega) = -16.0 + i1.088$. The surface realizations were limited to the area $L \times L$, with $L = 25\lambda$ and discretized on a grid of 321×321 points. Each surface realization was characterized by the Gaussian-cosine correlation function (18) with the correlation lengths $a = \lambda/4$ and $b = a/2$, the RMS height was $\delta = \lambda/40$. The MDRC was averaged over an ensemble of $N_s = 5000$ surface realizations. Here $\alpha \to \beta$ denotes β-polarized incident light scattered into α-polarized light. The vertical dashed lines denote the angle of specular and retro-specular direction of scattering, $\pm\theta_0$, respectively.

The in-plane cuts show a strong presence of cross polarized scattering, which was much weaker in the MDRC for the Gaussian-correlated silver surface presented in Sec. 4.1.1. As mentioned when discussing the MDRC of Gaussian-correlated surfaces, the presence of cross-polarized in-plane scattering is caused by multiple-scattering; the same is true for out-of-plane ($\phi_s = \phi_0 + 90°$) co-polarized scattering. For the weakly rough metal surfaces discussed in this work, multiple-scattering is dominated by surface plasmon polaritons

(SPPs) excited by the incident light. For p-polarized incident light we can see that the scattering is suppressed in the vicinity of the normal angle of scattering $\theta_s = 0.0°$, for both co- and cross-polarization. Furthermore, the suppressed area is flanked by two peaks of higher intensity, forming a valley shape. The $\beta \to p$ scattering is observed to be much stronger than $\beta \to s$, which was also true to a lesser extent for the Gaussian-correlated silver surface.

For increasingly higher polar angles of incidence, the incoherent scattering for p-polarized incident light, is progressively more co-polarized. In addition, it is observed that the peak located in the forward scattering direction decreases, while the peak in the backward scattering direction increases. The intensity is greatly enhanced for $p \to p$ polarization, while the other scattering contributions remain almost unchanged. For s-polarized incident light, the distributions are closer in resemblance to the Gaussian co-polarized cases in Sec. 4.1.1. For larger polar angles of incidence the $s \to s$ distribution is slightly more enhanced in the backwards scattering direction ($q_1 < 0$).

The valley structure along with the strong presence of multiple-scattering, was not present in the MDRC for the Gaussian-correlated silver surface presented in Fig. 4, which had the same correlation length and RMS-height as the surface of System 1. Furthermore, for non-normal incidence the $p \to p$ scattering is observed to dominate over the other in-plane scattering distributions to a much greater extent than what was seen for the Gaussian-correlated silver surface. Therefore, it can be concluded that these effects are purely caused by the Gaussian-cosine correlation function of the surface; this will be discussed further in the end of this section where the shape of the Gaussian-cosine power spectrum is discussed.

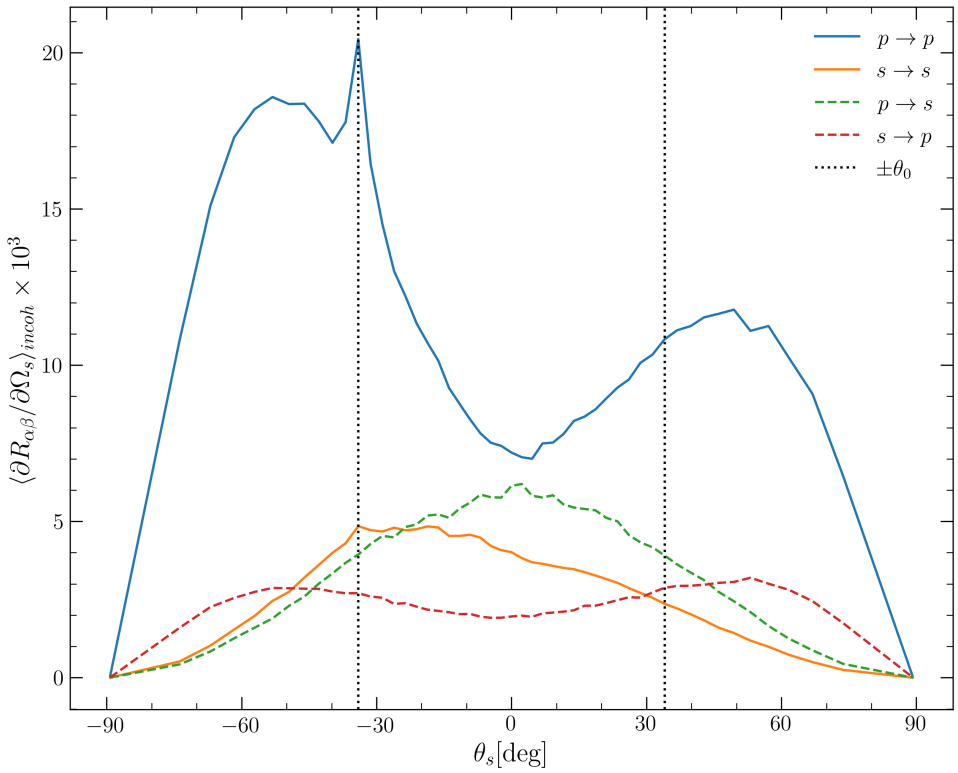

Figure 19: The same as in Fig. 18, except for the polar angle of incidence being $\theta_0 = 34.05°$

In Figs. 18 and 19, enhanced backscattering peaks can be seen in the retro-reflection

direction ($\theta_s = -\theta_0$) for the co-polarized scattered light, for all angles of incidence. Small peaks are also observed for the cross-polarized light for normal incidence, however, they are not visible for other polar angles of incidence. The enhanced backscattering peak was also present in the scattering for the Gaussian-correlated silver surface; therefore, it was expected to be present for Gaussian-cosine correlated silver surfaces as well. The phenomenon was not observed in the MDRC of the vacuum-glass system studied in Sec. 4.1.1, since SPPs require a dielectric-metal interface to be exited. In Fig. 40 the in-plane MDRC of a Gaussian-cosine correlated glass surface is shown; the enhanced backscattering peak is not present there either. The difference in intensity between $s \to s$ and $p \to s$ is not as vast as observed for System 1, which along with the weak enhanced backscattering peak suggest that the coupling to SPPs is weak for this surface.

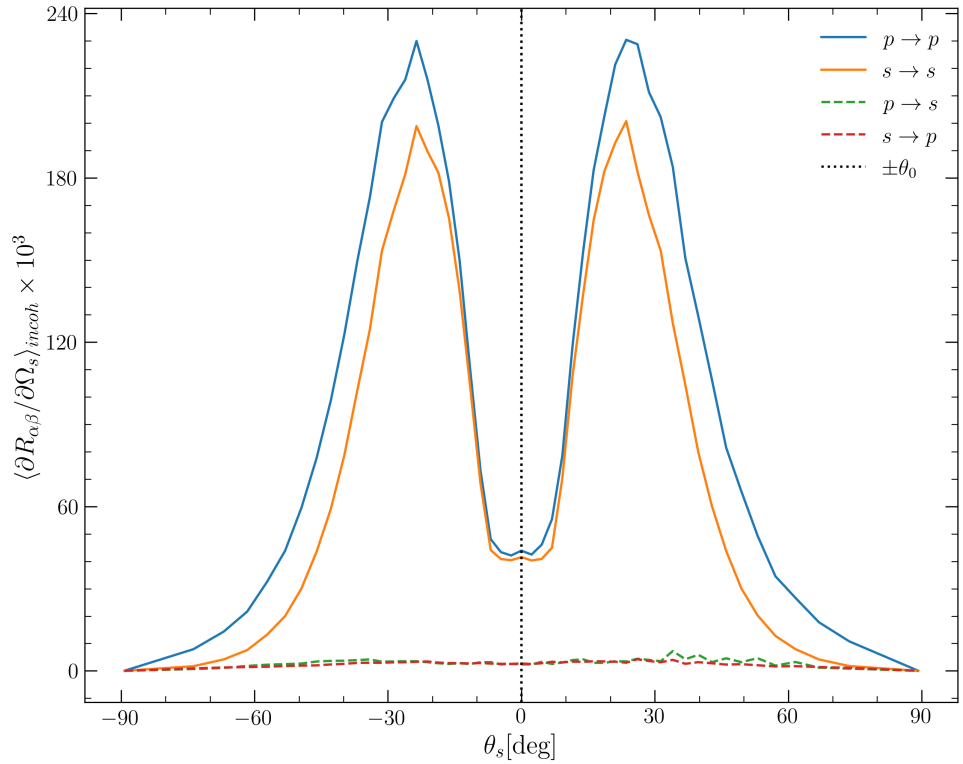

Figure 20: The same as in Fig. 18, except for the correlation length and RMS height being $a = \lambda$ and $\delta = \lambda/20$, respectively.

For some polar angles of incidence, small peaks are discernible in the specular direction of the MDRC for $p \to p$-polarized light, which could be manifestations of another multiple-scattering phenomenon, namely *the enhanced forward scattering peak* [3, pp. 61–67]. The origin of enhanced forward scattering peak lies in quadruple scattering processes, and require a power spectrum, $g(|\boldsymbol{k}_\parallel|)$, which supports counter-propagating SPPs. This is only possible if the length of the SPP wave vector, k_{spp}, and the power spectrum satisfies $g(2\,|k_{spp}|) \neq 0$ at the frequency, ω, of the incident light [3, pp. 61–67]. For a vacuum-silver interface, using Eq. (11) yields $k_{spp} \approx (1.033 + i0.002)\omega/c$ at the wavelength $\lambda = 632.8\,\text{nm}$; this gives $g(2\,|k_{spp}|) \approx 1.316$, which makes System 1 susceptible for this phenomenon. If these peaks are indeed forward scattering peaks, then the contribution is weak enough to be almost entirely masked by other scattering processes.

The in-plane cut of the MDRC for System 2 is shown in Figs. 20, 21 for the angles of

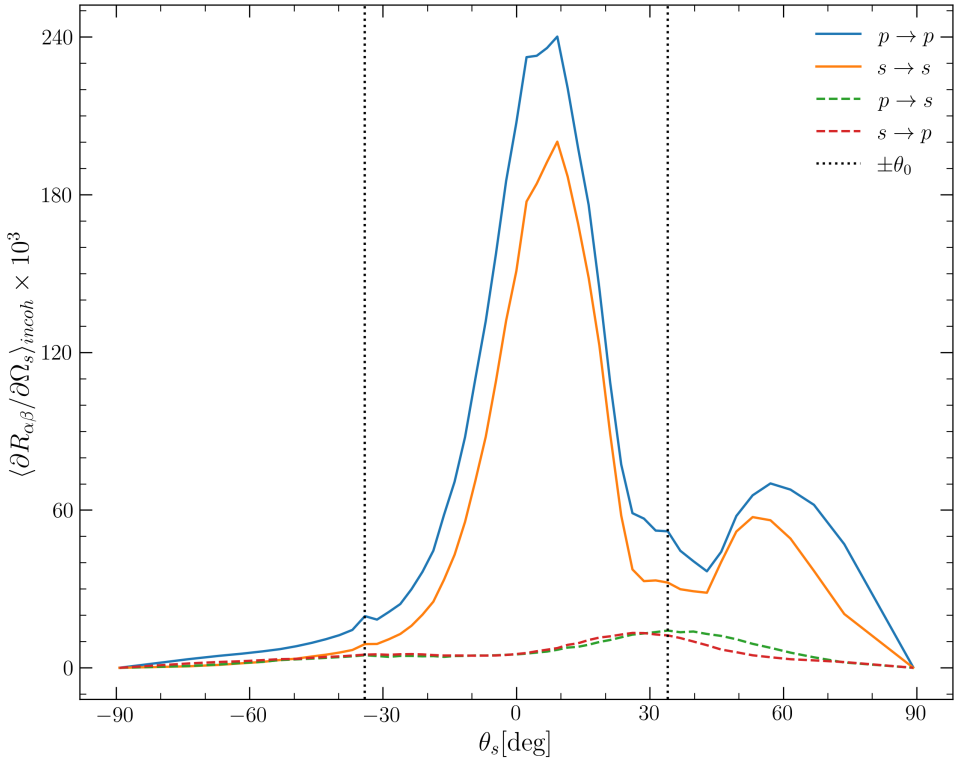

Figure 21: The same as in Fig. 20, except for the polar angle of incidence being $\theta_0 = 34.05°$.

incidence $(\theta_0, \phi_0) = (0.0°, 0.0°)$ and $(\theta_0, \phi_0) = (34.05°, 0.0°)$, respectively. Similar trends are observed here as for System 1, such as a central area where the scattering is suppressed and an enhanced backscattering peak. For System 1 the suppressed area was located around the normal angle of scattering for all polar angles of incidence, while for System 2 the valley structure is much deeper relative to the surrounding peaks and it is observed that the structure is centered around the specular direction of scattering. In contrast to System 1, the cross-polarization contributes significantly less to the in-plane scattering in the MDRC of System 2. For normal incidence the cross-polarized scattering is negligible, while for non-normal incidence there are noticeable contributions located around the specular direction. The enhanced backscattering peak is observed again, however, it is much less pronounced here in comparison to the MDRC for System 1.

Just as for System 1, small peaks are visible in the specular direction for some angles of incidence for co-polarized scattering in the MDRC of System 2. One of the aforementioned peaks can be seen in Fig. 21, where the polar angle of incidence was 34.05°. The observed peak was first assumed to be an enhanced forward scattering peak, however, in this case k_{spp} yields $g(2\,|k_{spp}|) \approx 0$. Therefore, it can be concluded that this peak is unlikely to have originated from the enhanced forward scattering phenomenon. It is possible that another multiple-scattering process could have caused these peaks; however, statistical fluctuations and numerical artifacts are not ruled out either.

The full angular distributions of the incoherent component of the MDRC as a function of the lateral wave vector $\boldsymbol{q}_{\parallel}$ can be seen in Figs. 22 and 23 for System 1. The Figures and labels are organized in the same manner as described earlier in Sec.4.1.1 concerning the MDRC of Gaussian-correlated surfaces.

The MDRC of System 1 under normal incidence, Fig. 22, has many of the patterns

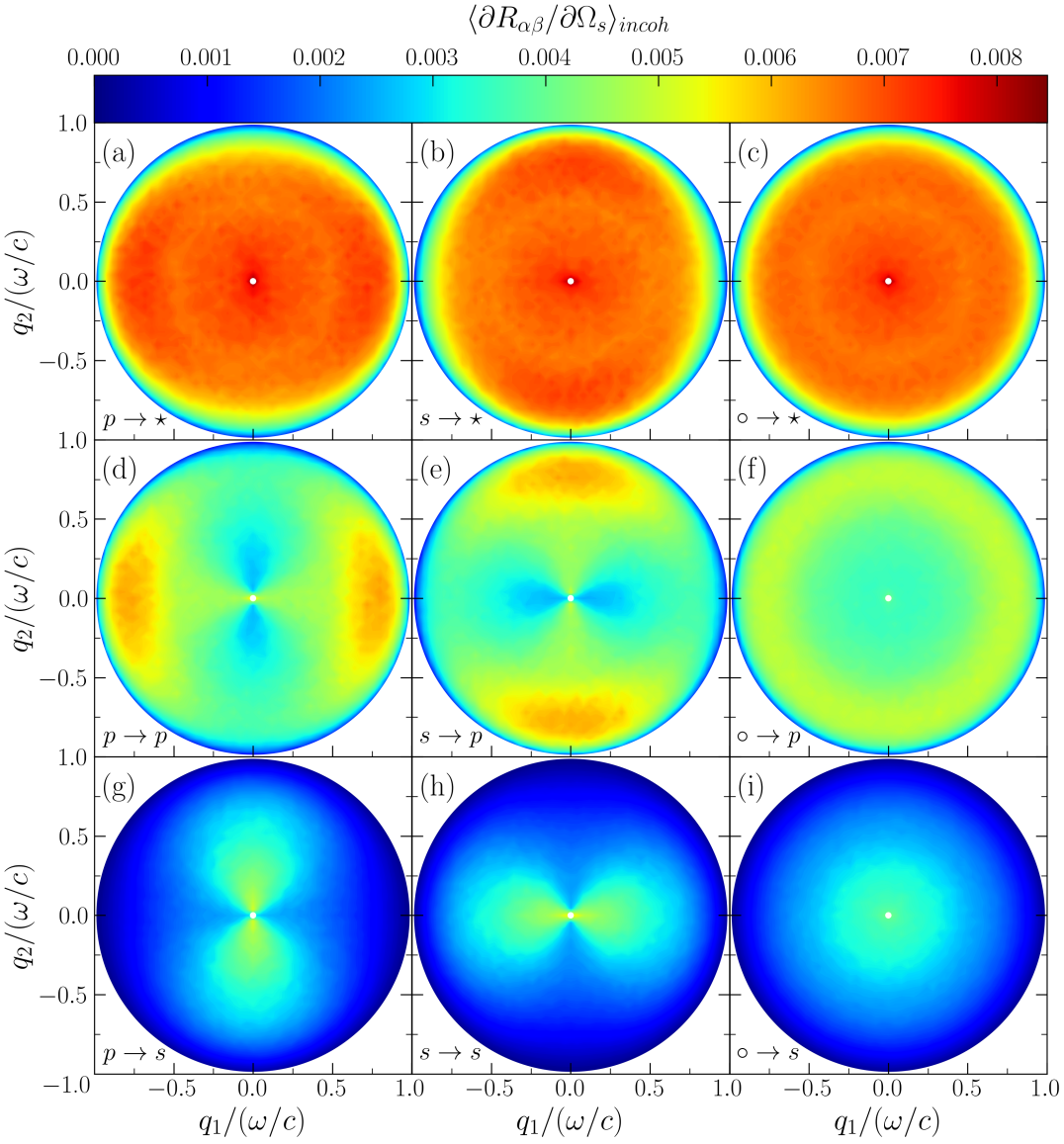

Figure 22: The full angular distribution of the incoherent component of the MDRC (42), for light scattering from a rough interface between vacuum and silver, as a function of the lateral wave vector $\boldsymbol{q}_{\parallel}$. The angles of incidence were $(\theta_0, \phi_0) = (0.0°, 0.0°)$. The parameters are the same as for Fig 18. In panels (c),(f) and (i) the " $\circ$" denotes that the incident light is unpolarized, while " $\star$" in panels (a)–(c) denotes that the polarization of the scattered light was not recorded.

which were observed in the angular distribution of the MDRC for the Gaussian-correlated silver surface, see Fig. 7. The dipole-like structure can again be seen for the co- and cross-polarized light (Figs. 22(d),(e),(g),(h)). However, the structures differ vastly between p- and s-polarized scattered light. In the case of p-polarized scattered light, the light is distributed over a much wider range of angles than $\beta \to s$ scattering and what was previously observed with Gaussian correlation. It is again observed that the intensity is strongest parallel and perpendicular to the plane of incidence for co- and cross-polarized light, respectively. It is observed that the s-polarized scattered light is concentrated around the origin; while p-polarized scattered light is stronger away from the origin, where the

polar angles of scattering are higher. Comparing the second and third row from the top, it is clearly seen that p-polarized incident light is scattered more by the surface than s-polarized incident light. For the Gaussian-correlated surfaces the differences between the polarizations of the scattered light in the angular distributions of the incoherent MDRC were marginal, while for the Gaussian-cosine correlated surface of System 1 there is a striking contrast.

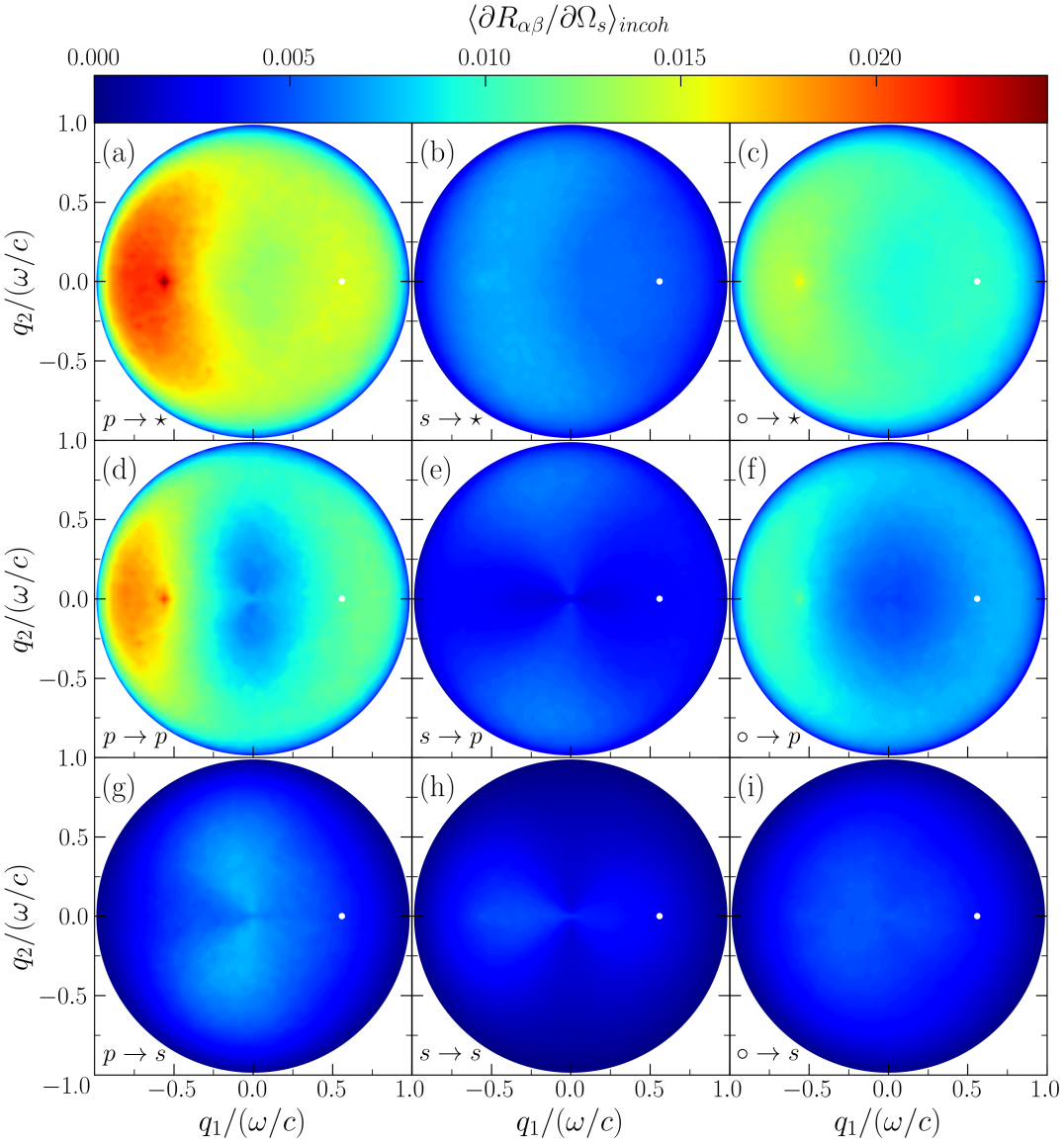

Figure 23: The same as in Fig. 18, except for the polar angle of incidence being $\theta_0 = 34.05°$.

The full angular distribution of the incoherent MDRC of System 1 can be seen in Fig. 23 for $(\theta_0, \phi_0) = (34.05°, 0.0°)$. Here it is readily seen that the co-polarized scattering for p-polarized incident light dominates the scattering from the surface. The enhanced backscattering peak is clearly distinguishable in the anti-specular direction. Furthermore, the dip in intensity around the origin, which was observed in the in-plane cut for p-polarized scattered light, is clearly seen in the second row from the top. The strong presence of multiple-scattering, along with the prominent enhanced backscattering peak and the bias towards p-polarized scattering, shows that the surface of System 1 has a

strong ability to support the excitations of SPPs.

When the polar angle of incidence is increased from normal incidence, several trends are observed. The contribution from s-polarized incident light diminishes, while it is enhanced in the p-polarized case. The dipole pattern observed for normal incidence vanishes and is only weakly noticeable in the $s \to s$ and $s \to p$ scattering. The p-polarized scattered light concentrates in the backward scattering direction. Generally, the contrasts between what was observed for the Gaussian-correlated surfaces and the results from System 1, broaden for increasingly non-normal incidence.

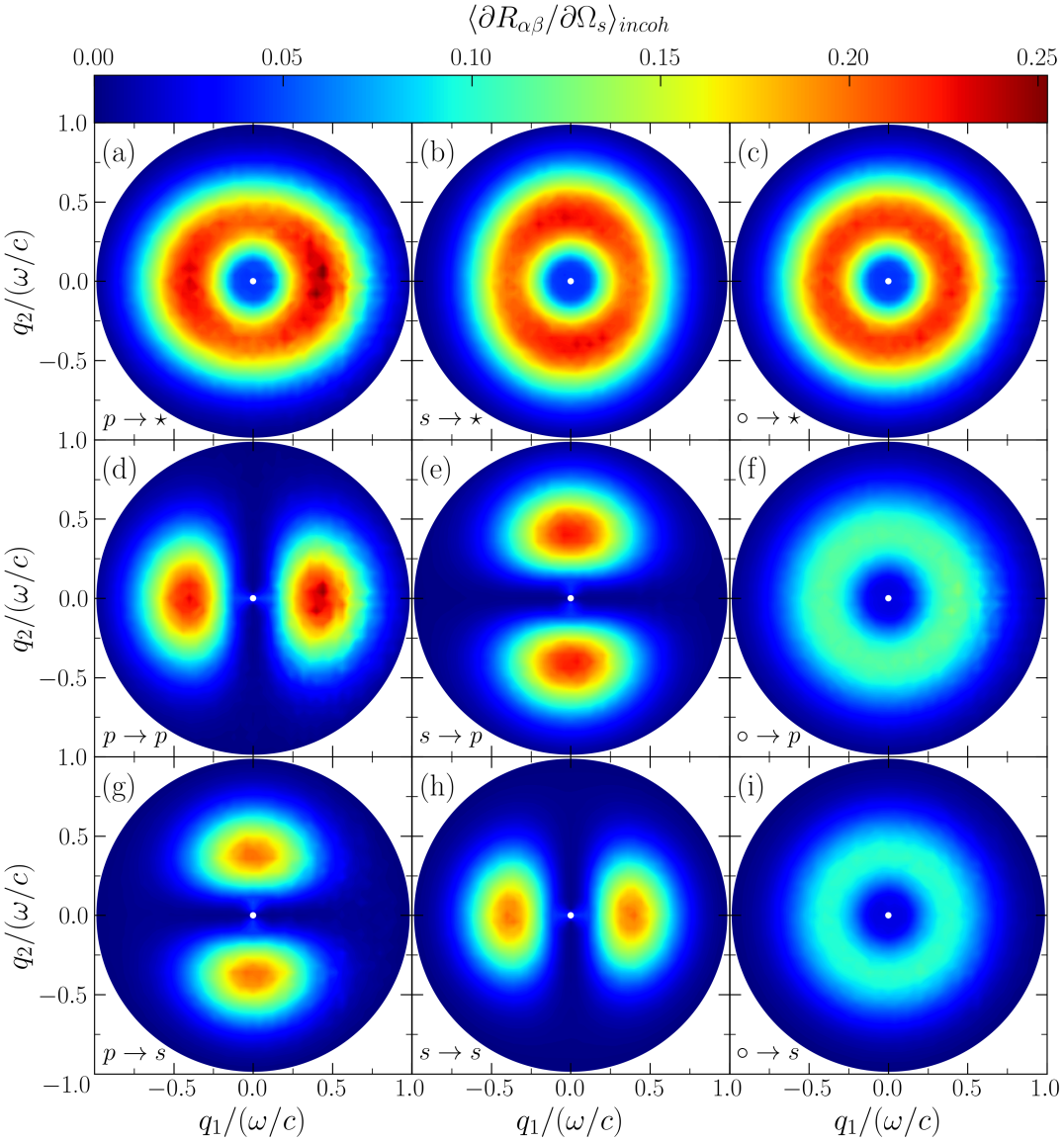

Figure 24: The same as in Fig. 22, except for the correlation length and RMS height being $a = \lambda$ and $\delta = \lambda/20$, respectively.

The full angular distribution of the incoherent component of the MDRC for System 2 as a function of $\boldsymbol{q}_{\parallel}$, can be seen in Figs. 24 and 25 for the spherical angles of incidence $(\theta_0, \phi_0) = (0.0, 0.0)$ and $(\theta_0, \phi_0) = (34.05, 0.0)$, respectively. Here it is observed that the distributions share many similarities with the results obtained for the Gaussian-correlated surfaces, except for a strong suppression of scattering modes around the specular direction

of reflection. This specular suppression effect was also present in results for Gaussian-cosine correlated vacuum-glass interfaces in Ref. [8], where the scattering results were obtained with a approach based on the Kirchhoff approximation [41].

The MDRC for normal incidence, shown in Fig. 24, is the most similar to the results for the Gaussian-correlated case seen in Fig. 7. The symmetries and patterns are almost identical, except for the reduced scattering near the specular direction. The dipole pattern is observed for the co- and cross-polarized scattered light. However, because of the scattering suppression around the origin, the two dipole branches are split in half. The two halves lie symmetrically about the q_1q_3- and q_2q_3-plane for cross and co-polarized light, respectively. The anisotropy in $\beta \to \star$ contour plots, is observed here as well. The lack of contribution in the q_1q_3- and q_2q_3-plane for cross- and co-polarized light shows that there is very little multiple-scattering present in System 2; this suggests that the coupling to SPPs is relatively weak.

The MDRC for non-normal incidence, which can be seen in Fig. 25, shows trends similar to the ones observed for normal incidence. The contour plots are similar to the Gaussian-correlated case, except for a suppression of scattering encompassing the specular direction. However, the dipole pattern in the $p \to p$ scattering is concentrated in the forward scattering direction ($q_1 > 0$), which is the opposite of what was observed for the Gaussian-correlated silver surface. There, it was found that the $p \to p$ scattered light was concentrated in the backwards scattering direction, the same is observed for System 1 in Fig. 23. Therefore, the cause of the effect observed here is assumed to partly lie in either the correlation length or the RMS-height of the system.

The suppression effect observed for the Gaussian-cosine correlated surfaces, could be of interest to the solar cell industry. Simplified, a photovoltaic (PV) cell consists of three layers: the anti-reflection coating (ARC), which transmits the incident light into the cell; a base, which absorbs the light and generates the current; and a back reflector, which reflects any unabsorbed light back through the base. The efficiency of thin PV-cells can be increased by introducing roughness to the interfaces between the layers [11].

A back reflector with a roughness designed to scatter the incident light above the critical angle of the ARC-base interface, or the ambient-ARC interface, ensures total internal reflection; this would effectively trap any unabsorbed light in the active region of the cell. This is most often achieved by covering the back reflector with a periodic grid of pyramid structures [42], which reflect the light at polar angles high enough to trap the light. However, In ultra thin PV-cells these pyramid structures are more difficult to incorporate, and a rough surface with similar reflective properties is more feasible.

For normal incidence, the in-plane cut of System 2 shown in Fig. 20 shows that the incoherent scattering is strongly suppressed for polar angles in the range $\theta_s \approx [-10°, 10°]$. If the critical angle for the ARC-base interface of a PV-cell was $\theta_c = 10°$ or lower, then System 2 would be a good candidate for a back reflector surface. However, for higher critical angles the angular area of suppression needs to be enlarged; the radius would have to correspond to the critical angle or above for light to be trapped in the PV-cell. Short simulation tests have show that the radius can be controlled by adjusting the b parameter in the Gaussian-cosine auto-correlation function, this is further supported by the shape of the power spectrum when b is adjusted, which is discussed later in this section.

For the surface to have a relevant impact on the performance of the PV-cell, it also requires the percentage of the incident light reflected incoherently by the surface to be

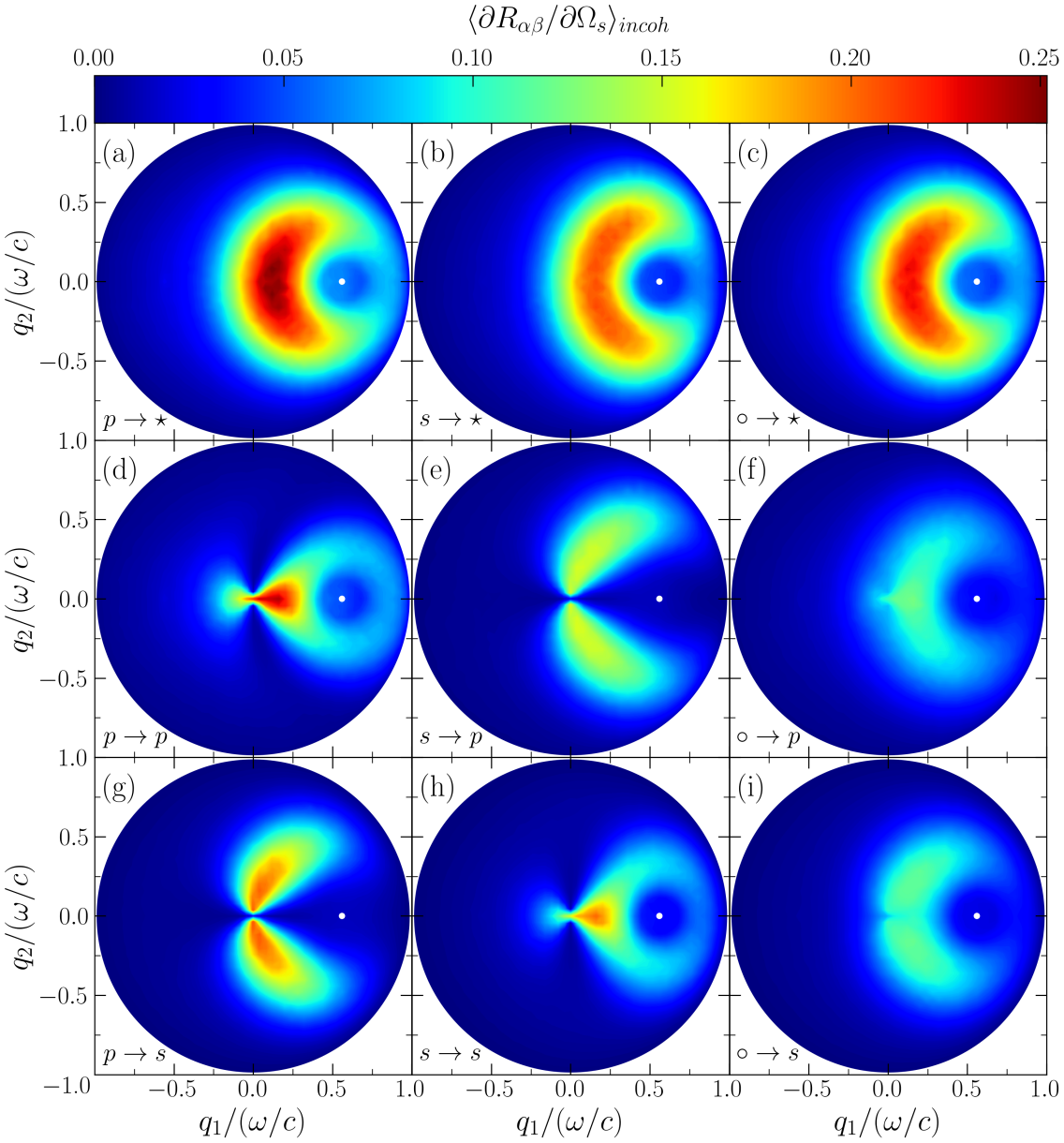

Figure 25: The same as in Fig. 20, except for the polar angle of incidence being $\theta_0 = 34.05°$.

quite high. The incoherent reflectance of the Gaussian-cosine correlated surfaces for normal incidence were $\mathscr{R}_{incoh}(\theta_0) \approx 0.029$ and $\mathscr{R}_{incoh}(\theta_0) \approx 0.341$ for System 1 and System 2 respectively. This shows that the surface of System 2 is quite promising as a back reflector in a PV-cell, as it reflects a high percentage of the light diffusely and suppresses near-normal scattering. However, more numerical studies are required, using relevant materials and wavelengths, to find the optimal surface parameters for solar cell applications. In addition, the development of reliable methods for the manufacturing of Gaussian-cosine correlated surfaces is required, followed by experimental verification of the numerically observed properties.

To get a further understanding of the structures observed in the MDRC, e.g., the near specular suppression in System 2, we will study the power spectra of all the systems shown so far. In Fig. 26, the power spectra for both the isotropic Gaussian and Gaussian-

cosine correlated surfaces are displayed as functions of $q_{\parallel}$. The power spectra have been normalized with respect to their maxima, which is denoted by $G(q_{\parallel})$, to highlight the differences in their shapes. To show what happens when the parameter b is slight adjusted, a power spectrum with $b = a/3$ is displayed, with the same correlation length as System 2.

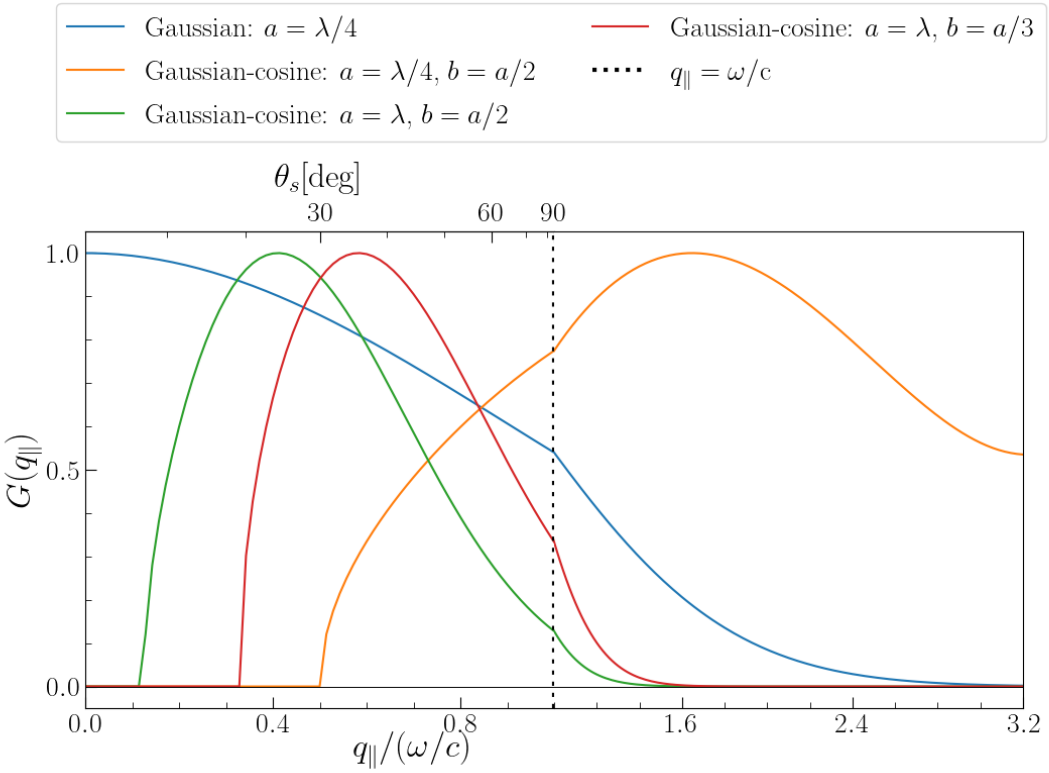

Figure 26: The power spectra of isotropic Gaussian, and Gaussian-cosine correlated surfaces, normalized with respect to their maxima, as functions of $q_{\parallel}$. The dashed line denotes the border between propagating modes ($q_{\parallel} \leq \sqrt{\varepsilon_1(\omega)}\omega/c$ and non-propagating (evanescent) modes, the axis has been scaled down in this region to save space and highlight the propagating region. The polar scattering angles corresponding to the propagating modes, are shown on the top.

From small-amplitude perturbation theory (SAPT) it can be shown that the single-scattering contribution to the incoherent MDRC is proportional to the power spectrum [3, pp. 31–34], i.e.,

$$\left\langle \frac{\partial R^{(1)}_{\alpha\beta}(\boldsymbol{q}_{\parallel}|\boldsymbol{k}_{\parallel})}{\partial \Omega_s} \right\rangle \propto g(\boldsymbol{k}_{sc}), \tag{107}$$

where $\boldsymbol{k}_{sc} = \boldsymbol{q}_{\parallel} - \boldsymbol{k}_{\parallel}$ is the transfer wave vector of the single-scattering event. A know consequence from Eq. (107) is that when $g(\boldsymbol{k}_{sc}) = 0$, single-scattering events from $\boldsymbol{k}_{\parallel}$ to $\boldsymbol{q}_{\parallel}$ are forbidden.

The isotropic Gaussian-cosine power spectra shown in Fig. 26 are all zero in circular regions centered around the origin, where the radii dependent on the correlation length and the value of the b parameter. For scattering events $\boldsymbol{k}_{sc}$ in these regions, the single-scattering term in SAPT will be zero, which means that single-scattering events do not contribute to the MDRC. Consequently, the scattering is suppressed where $g(k_{sc}) = 0$

and the contribution to the MDRC near $\boldsymbol{k}_{sc} = \mathbf{0}$ mainly comes from multiple-scattering processes. This is why we observe the valley structures in the MDRC of Gaussian-cosine correlated surfaces around the specular direction.

Since the surfaces in this section are only moderately rough, multiple-scattering is dominated by interactions with SPPs. For a vacuum-silver interface, when $\lambda = 0.6328\,\mu\text{m}$ the length of the SPP wavevector is $|k_{spp}| = 1.0326$. For System 1, we see that in the non-zero part of $G(q_{\parallel})$ there is a maxima near k_{spp}. Because multiple-scattering terms in SAPT also depend on the magnitude of the power spectrum, the contribution from multiple-scattering is affected by the magnitude of the power spectrum; this could partly explain the large contribution from multiple-scattering observed in the MDRC of System 1. The power spectrum of System 2 is very weak in most of the evanescent region relative to the propagating region, which suggest that there is little contribution from multiple-scattering relative to single-scattering; this is especially seen in the lack of cross-polarization in the in-plane scattering seen in Fig. 20. The Gaussian power spectrum has a substantial contribution from the evanescent region. However, it is weaker relative to the propagating region, which might be the reason why the contribution from multiple-scattering is not as prominent for the Gaussian-correlated silver surface compared to System 1. The observations made here indicate that the weak contribution from multiple-scattering for System 2 and the Gaussian-correlated silver surface, does not necessarily lie in a weak coupling to SPPs; to the contrary, it could just be that the single-scattering contribution overshadows and masks the multiple-scattering contribution for these surfaces. Consequently, the single-scattering contribution in System 1 is only weak enough to not mask the SPP mediated scattering contribution, which is not necessarily stronger than for the other systems.

In Fig. 26 it is also displayed what happens when the parameter b is decreased; It is observed that the radius of the region where the power spectrum is zero increases by a substantial amount. For System 2 the radius of this region is the same as the radius of the near specular suppression seen in the MDRC. The radius of System 2 corresponds to the polar angle of scattering $\theta_s \approx 8°$, by adjusting b to from $a/2$ to $a/3$ the radius has been increased to $\theta_s \approx 20°$.

To show that the multiple-scattering in weakly rough surfaces is predominantly caused by the excitation of SPPs and is not an effect of the Gaussian-cosine power spectrum, the in-plane cut of the incoherent component of the MDRC of a Gaussian-cosine correlated glass surface is presented as a function of the polar angle of scattering in Fig. 27. Since glass does not support the excitation of SPPs, the contribution from them is eliminated.

In Fig. 27 the roughness parameters were the same as for System 1, the polar angle of incidence was $\theta_0 = 0°$ in Fig. 40(a) and $\theta_0 = 34.05°$ in Fig. 40(b). Comparing this with the results for a silver surface, seen in Fig. 18, shows the strong effect the excitation of SPPs can have on the scattering. As expected, there is almost no cross-polarization, except for a negligible amount. The enhanced backscattering peak observed in the retro-specular direction is no longer present. The valley is deeper and the suppressed region has the same radius as the power spectrum. The shape of the MDRC resembles the one for System 2 more than the MDRC of System 1; this is more clearly seen in the full angular distribution shown in Appendix C.

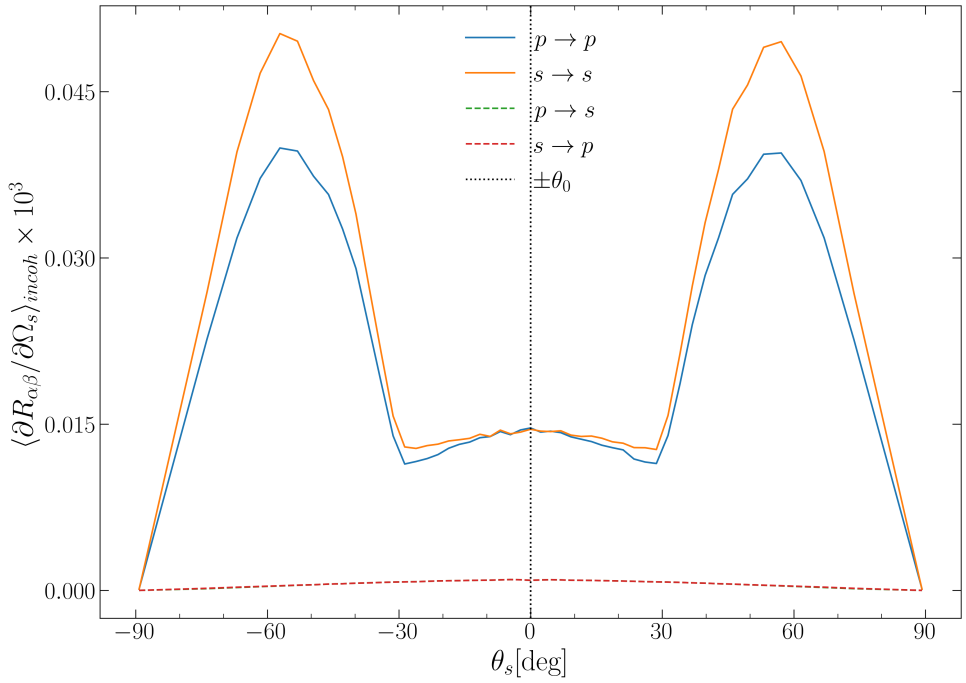

(a) $\theta_0 = 0°$

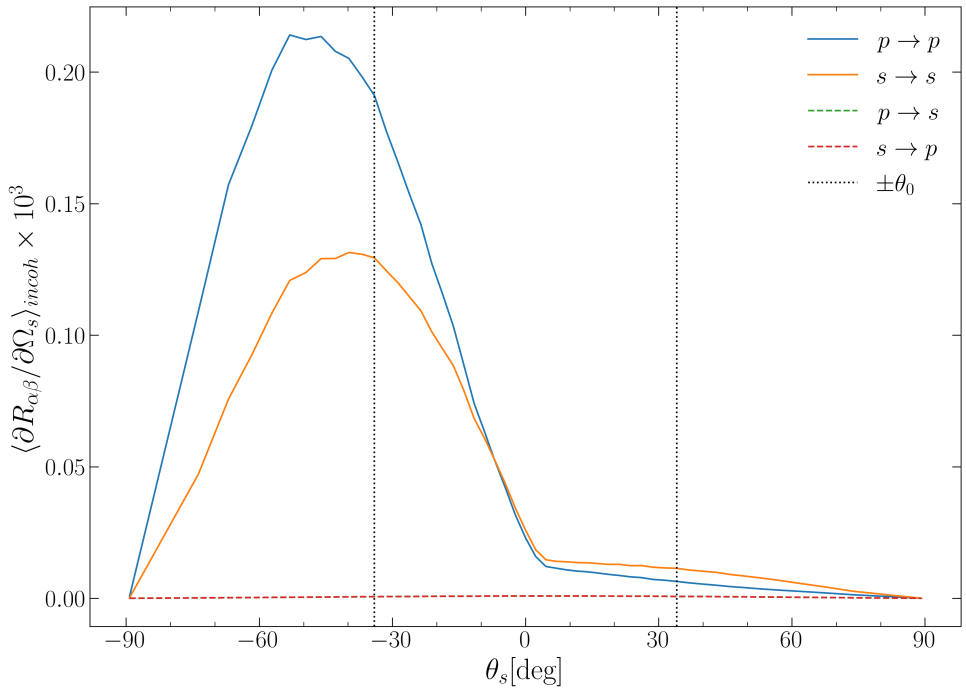

(b) $\theta_0 = 34.05°$

Figure 27: The in-plane cut of the incoherent component of the MDRC for a rough glass surface as a function of the polar angle of incidence. The surface realizations had an RMS height of $\delta = \lambda/40$ and were characterized by the Gaussian-cosine correlation function (18) with the correlation length $a = \lambda/4$ and $b = a/2$. The wavelength of the incident light was $\lambda = 0.6328\,\mu$m, and the refractive index of glass at this wavelength was assumed to be $n = 1.5$. The surface realizations used in the simulations were spatially limited to the quadratic area $25\lambda \times 25\lambda$, and discretized on a grid of 321×321 points. The results were averaged over an ensemble of 7269 surface realization.

4.2.2 The Mueller matrix

The incoherent elements of the Mueller matrix as functions of $\boldsymbol{q}_{\parallel}$, were calculated for System 1 and System 2. The elements are normalized with respect to the first element, to emphasize the polarization behavior of the Gaussian-cosine correlated surfaces.

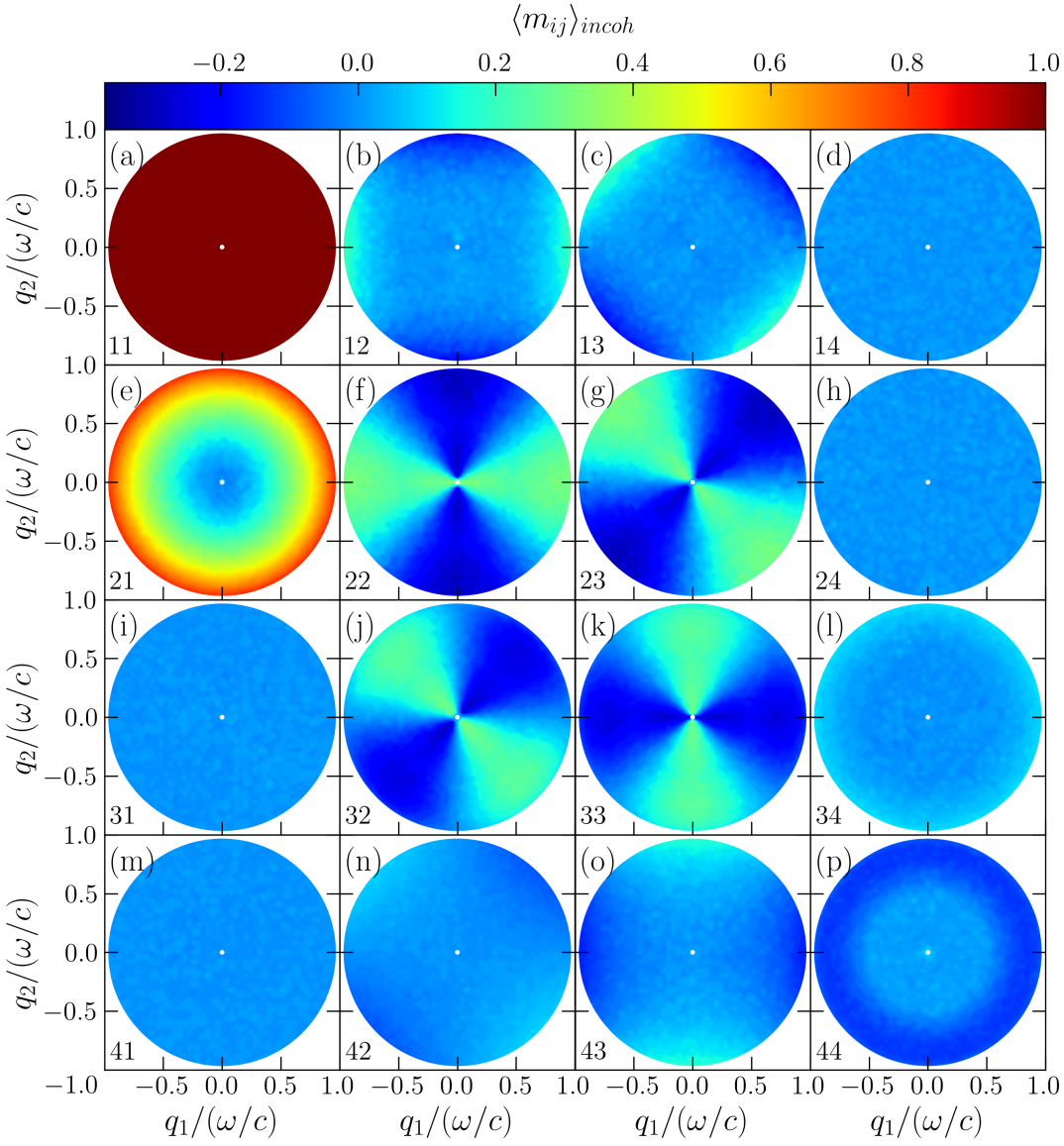

Figure 28: The full angular distribution of the 16 elements of the Mueller matrix (44) from light scattered incoherently by a randomly rough silver surface as a functions of q_1 and q_2. The angles of incidence were $(\theta_0, \phi_0) = (0.0°, 0.0°)$. The parameters are the same as for Fig. 18. The elements $\langle m_{ij}\rangle$ (i,j = 1,2,3,4) are organized as a matrix, where i and j denote row numbered from the top and the column numbered from the left, respectively. The elements are normalized with respect to the first element, i.e., $\langle m_{ij}\rangle = \langle M_{ij}\rangle/\langle M_{11}\rangle$. The white spots indicate the specular direction of reflection.

The results for System 1 are presented for normal and non-normal incidence in Figs. 28 and 29, respectively. Both have a lot more noise compared to the results for the Gaussian-correlated surfaces, however, some information is still present which shows trends similar

to the Gaussian ones. The symmetries predicted for normal incidence are observed again. The contribution from m_{21} is very similar to the one observed for Gaussian-correlated silver surface. This element can be understood from observing the MDRC, since m_{21} is proportional to the difference between $\circ \to p$ and $\circ \to s$. Thus, m_{21} describes that the light scattered from the surface of System 1 is increasingly dominated by p-polarized light for higher angles of scattering.

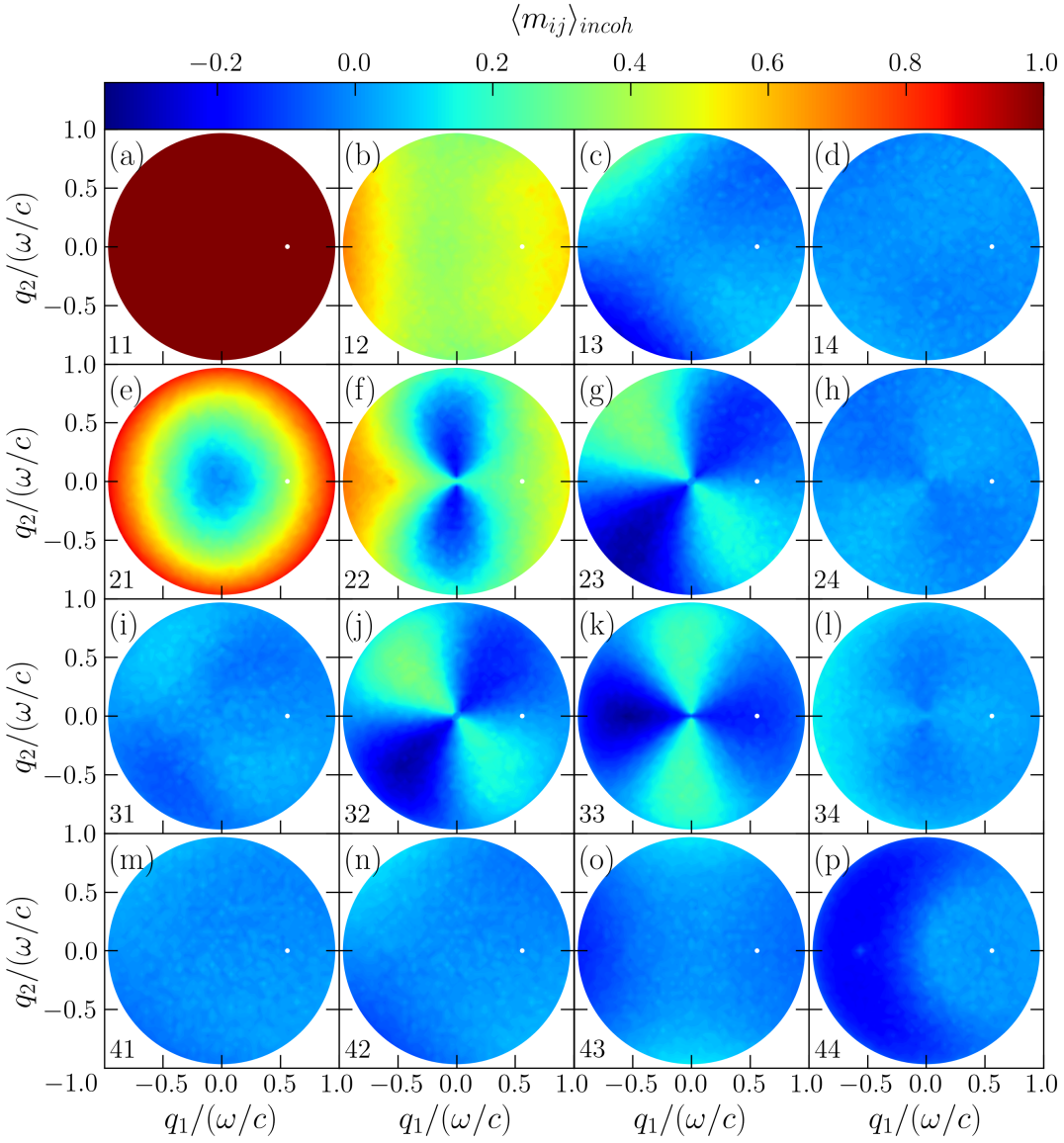

Figure 29: The same as in Fig. 28, except that the polar angle of incidence is $\theta_0 = 34.05°$.

For non-normal incidence, seen in Fig.29, the symmetries observed between the second and third column are no longer present. The upper left block of the matrix, which is related *diattenuation* [36, pp. 165–166], has a strong contribution compared to the rest of the matrix. By studying the effect on the stokes vector, it can be seen that this block affects vertically and horizontally polarized light. The strong contribution in this block is not surprising as the incoherently scattered light was observed to be mainly p-polarized in the MDRC of system 1. Here $m_{2,3}, m_{32}$ and m_{33} remain almost unchanged, while the m_{22} element has a quite distinct distribution compared to normal incidence. Negative values

of m_{22} denote that the scattering is mostly cross-polarized, conversely, positive values indicate that co-polarization dominates. We can see here that co-polarization dominates in most direction, while cross-polarization contributes the most near the out-of-plane direction (q_2q_3-plane). In the m_{22} element of the Gaussian-correlated surfaces, the contribution from cross- and co-polarization was separated into more distinct sections and the contrast between the sections was more pronounced.

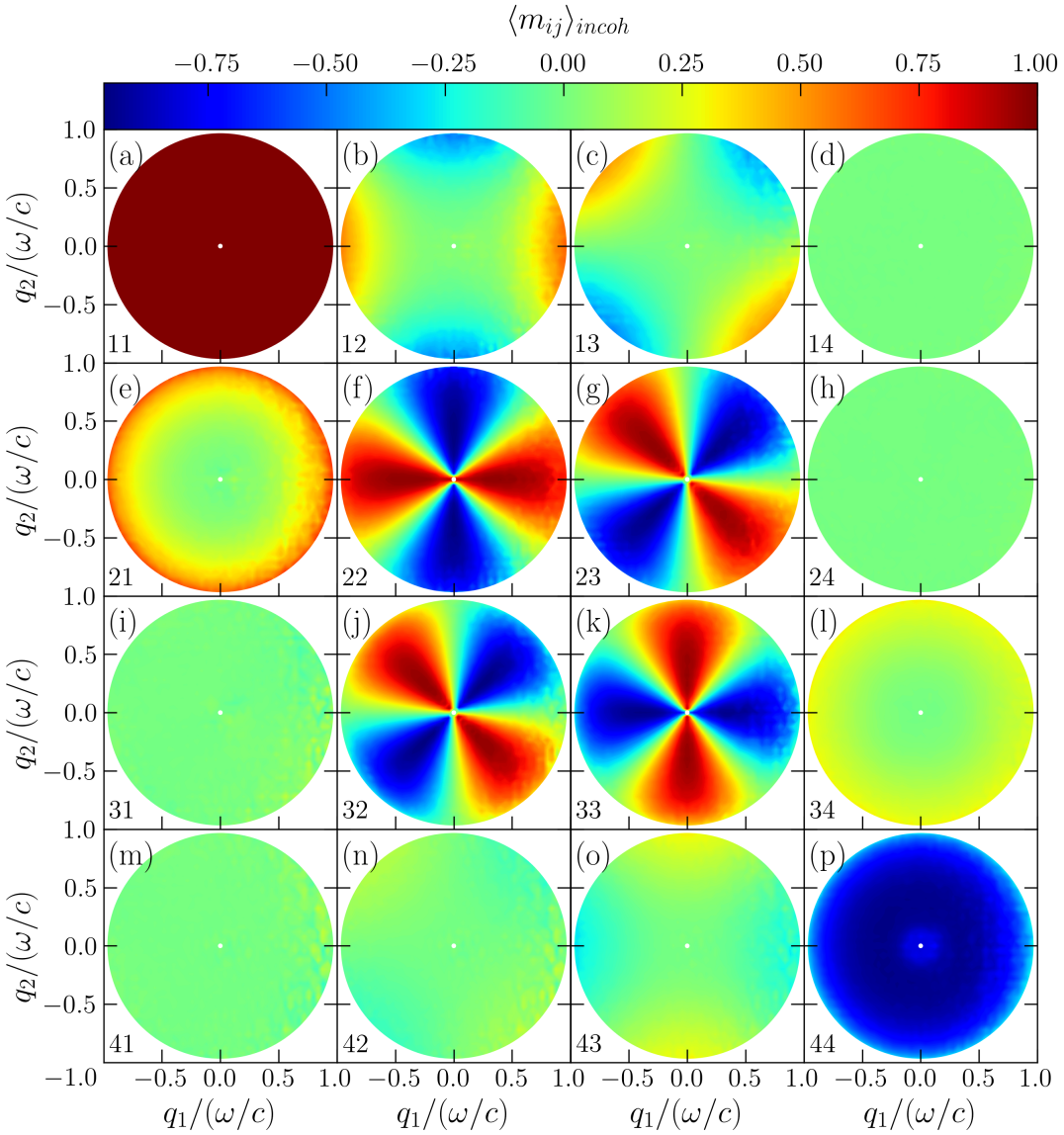

Figure 30: The full angular distribution of the 16 elements of the Mueller matrix (44) from light scattered incoherently by a randomly rough silver surface as a functions of q_1 and q_2. The angles of incidence were $(\theta_0, \phi_0) = (0.0°, 0.0°)$. The parameters are the same as for Fig. 20. The elements $\langle m_{ij}\rangle$ (i,j = 1,2,3,4) are organized as a matrix, where i and j denote row numbered from the top and the column numbered from the left, respectively. The elements are normalized with respect to the first element, i.e., $\langle m_{ij}\rangle = \langle M_{ij}\rangle/\langle M_{11}\rangle$. The white spots indicate the specular direction of reflection.

The Mueller matrix elements for System 2 are presented for normal and non-normal incidence in Figs. 30 and 31, respectively. Compared to System 1 there is much more

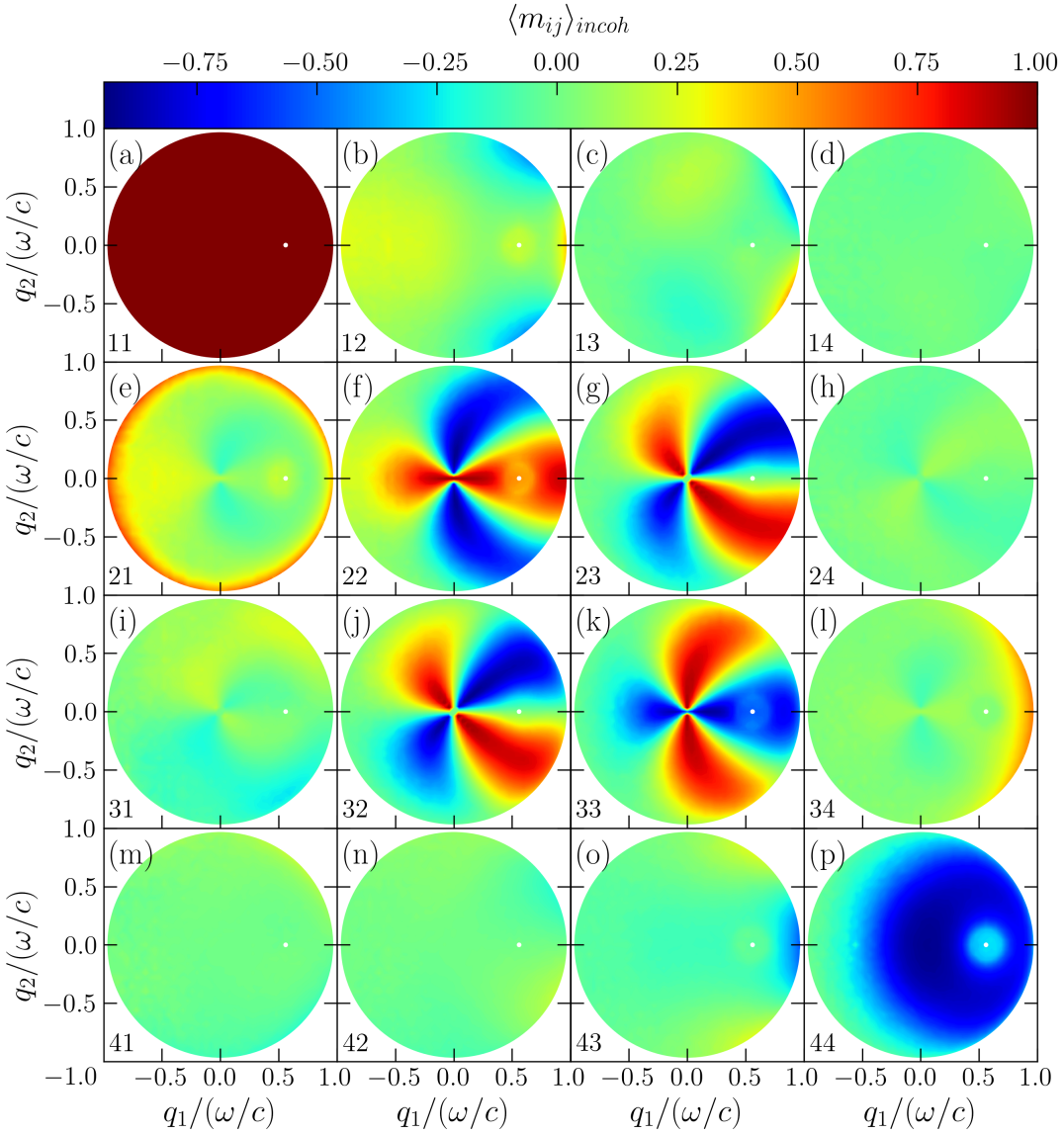

Figure 31: The same as in Fig. 30, except that the polar angle of incidence is $\theta_0 = 34.05°$.

structure and less noise in the angular distributions. For normal incidence the expected symmetries are observed. The elements are almost identical to the ones for Gaussian-correlated silver surface. The scattering suppression observed in the MDRC has a visible effect in the origin of the m_{44} element.

For non-normal incidence the near specular intensity dip observed in the MDRC has visible influence on more elements. In the m_{33} and m_{44} elements, where the contribution is negative near the specular direction, the dip is replaced by a local maximum instead of a minimum. The strong similarities with the Gaussian-correlated silver surface are still present in most elements. It is again observed that the rotational symmetries in the second and third column disappear, yet the equality under change of sign of the m_{22} and m_{33} elements remains, along with $m_{23} \approx m_{32}$.

The m_{12} and m_{13} elements have a weaker contribution located mostly in the forward scattering direction, while for the Gaussian-correlated silver surface the contribution was stronger and located in the backwards scattering direction. The central block elements

appear to be warped towards the specular direction, which was also observed in the Gaussian case. The last element m_{44} has a noticeably weaker contribution in the backwards scattering direction along with the area near the specular direction. Moreover, a much stronger contribution is observed in the forward scattering direction of the m_{34} and m_{43} elements, which was only present in m_{43} in the Gaussian case.

4.3 Anisotropic Gaussian-cosine correlated surfaces

Simulations were performed for two anisotropic Gaussian-cosine correlated surfaces (19), where the correlation lengths were doubled along the q_2-axis, i.e., $a_2 = 2a_1 = 2a$ with $b = a/2$. Otherwise, parameters were the same for the two anisotropic systems as System 1 and System 2 in Sec.4.2. Examples of the resulting generated surfaces for the anisotropic counterparts of System 1 and 2 can be seen as color contour plots in Figs. 17(c) and 17(d), respectively. The same uncorrelated random numbers were used for the isotropic case, which can be seen in Figs. 17(a) and 17(b). By comparing the isotropic and anisotropic cases, it is possible to discern some of the same patterns. It can be seen that some peaks and low points in the isotropic surface have melded together or been stretched when the surface is anisotropic.

Since the surfaces have different properties in different directions, two simulations were performed for $\phi_0 = 0.0°$ and $\phi_0 = 90.0°$, for both anisotropic versions of System 1 and 2. The same numerical parameters were used as for the isotropic results. In summary, the length and the number of discretization points was $L = 25\lambda$ and $N_x = 321$ along each axis, respectively; the dielectric constant of silver at the wavelength $\lambda = 632.8\,\text{nm}$ was set to $\varepsilon_2(\omega) = -16.0 + i1.088$.

For the purpose of testing the energy conservation of the scattering process, a test simulation with fewer surface realizations was performed for each surface, where "non-absorbing" silver was used as a substrate instead, i.e. $\varepsilon_2(\omega) = -16$. Using Eq. (77) the total energy was found to be from $1 - 4\%$ higher than unity, depending on the surface and the angles of incidence. It is not fully understood why the anisotropic simulations were less stable than the isotropic ones. The cause of this deviation is suspected to lie in the software implementation of the numerical power spectra, which might have caused too steep surface slopes when anisotropic Gaussian-cosine correlation were used. Since the results with absorbing silver appeared to be reasonable with respect to the isotropic ones and $|\mathcal{U} - 1| < 0$, the deviations from unity observed in the test were considered acceptable.

4.3.1 Mean differential reflection coefficient

The incoherent mean differential reflection coefficient of the anisotropic Gaussian-cosine correlated surfaces were calculated in the same manner as the isotropic ones. The results for the anisotropic version of System 1 can be seen in Figs. 32 and 33 for $\theta_0 = 0.0°$ and $\theta_0 = 34.05°$, respectively. The same can be seen for the anisotropic System 2 in Figs. 24 and 25. To display the directional differences in the scattering from these surfaces, the results for $\phi_0 = 0.0°$ and $\phi_0 = 90.0°$ are shown side by side. The layout of the plots is the same as before, except that the results for unpolarized incident light are not shown. To highlight the differences between isotropic and anisotropic Gaussian-cosine surfaces, the results obtained for System 1 and 2 in Sec. 4.2.1 will be used for comparison with the anisotropic systems.

For the anisotropic System 1, when the light is incident in the q_1q_3-plane ($\phi_0 = 0.0°$), where the correlation length was unchanged, many of the trends observed for the isotropic case are still present. For normal incidence seen in Fig. 32(a), the contour plots are similar to the isotropic case when the incident light is p-polarized. When the incident light is s-polarized the shape of the distribution is also similar the isotropic one, however, the intensities are much stronger relative to the distributions with p-polarized incident light.

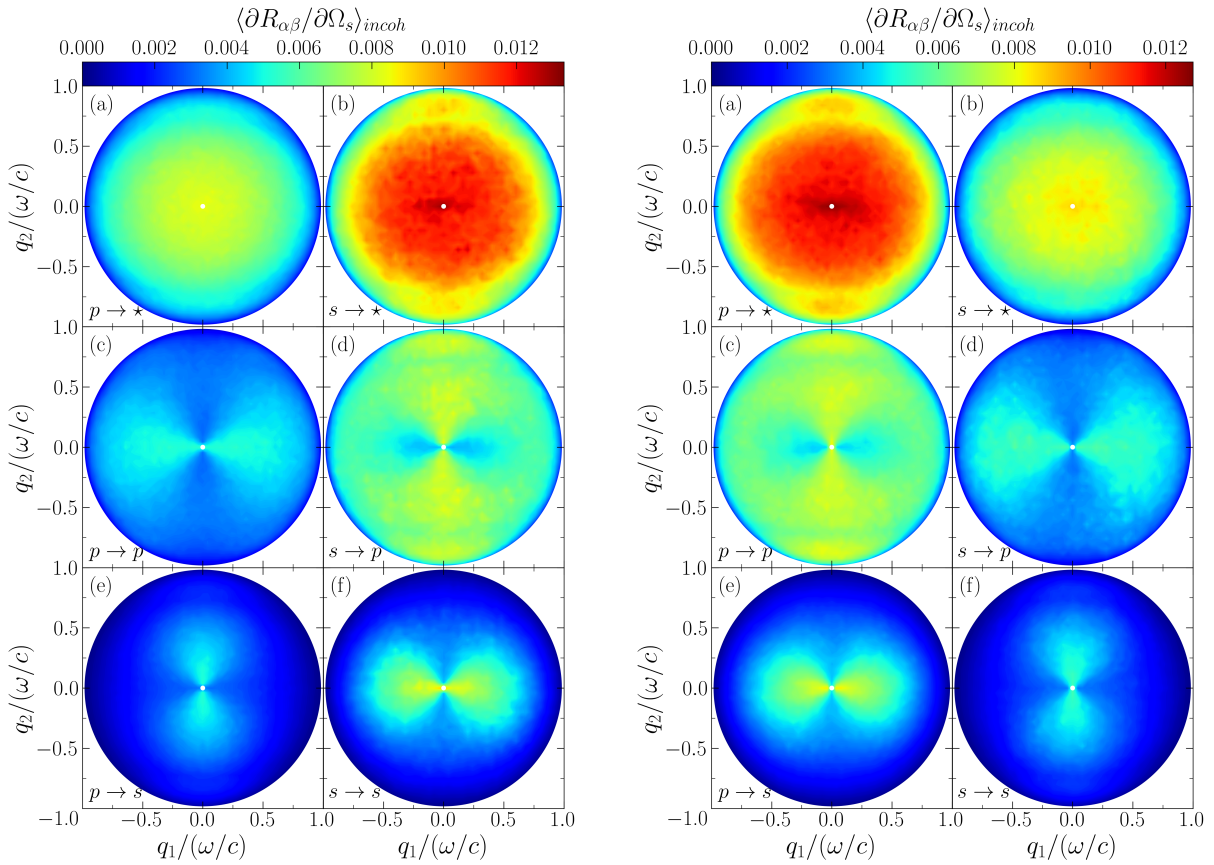

(a) $\phi_0 = 0°$ (b) $\phi_0 = 90°$

Figure 32: The full angular distribution of the incoherent component of the MDRC (Eq. (42)) for light scattering from a randomly rough interface separating vacuum and silver as a function of the lateral wave vector $\boldsymbol{q}_\parallel$. The interface is characterized by an anisotropic Gaussian-cosine auto-correlation function. The correlation lengths of the surface are $a_x = \lambda/4$ and $a_y = \lambda/2$, with $b = a_x/\lambda$; the RMS height is $\delta = \lambda/40$. To highlight the effect of the surface anisotropy, the MDRC is shown for light incident from two different azimuthal angles of incidence: $\phi_0 = 0.0°$ in panel (a); $\phi_0 = 90.0°$ in panel (b). The polar angle of incidence is $\theta_0 = 0.0°$ for both panel (a) and (b). The wavelength of the incident light (in vacuum) was $\lambda = 632.8\,\text{nm}$, the dielectric function of silver at this wavelength is $\varepsilon_2(\omega) = -16.0 + i1.088$. The surface realizations were limited to an area of $25\lambda \times 25\lambda$ and discretized on a grid of 321×321 points. The MDRC was averaged over an ensemble of $N_s = 5000$ surface realizations. Here $\alpha \to \beta$ denotes β-polarized incident light scattered into α-polarized light, where " $\circ$ " indicates that the incident light was unpolarized, and " $\star$ " that the polarization of the scattered light was not recorded.

For non-normal incidence seen in Fig 33(b), the differences between the isotropic and anisotropic surfaces seems substantial at first glance. However, by comparing the amplitudes of the two cases, it is observed that the maximum amplitude is lower for the anisotropic surface. Therefore, the lower intensities are enhanced here, resulting in the distribution to appear to be quite different, when they are in reality very close in resemblance. The enhanced backscattering peak is again observed, along with the intensity dip in the around the origin for $p \to p$ polarized light. In addition, $p \to p$ polarized

scattered light is again more concentrated in the backwards scattering direction, and s-polarized incident light is observed to scatter more weakly relative to p-polarized light.

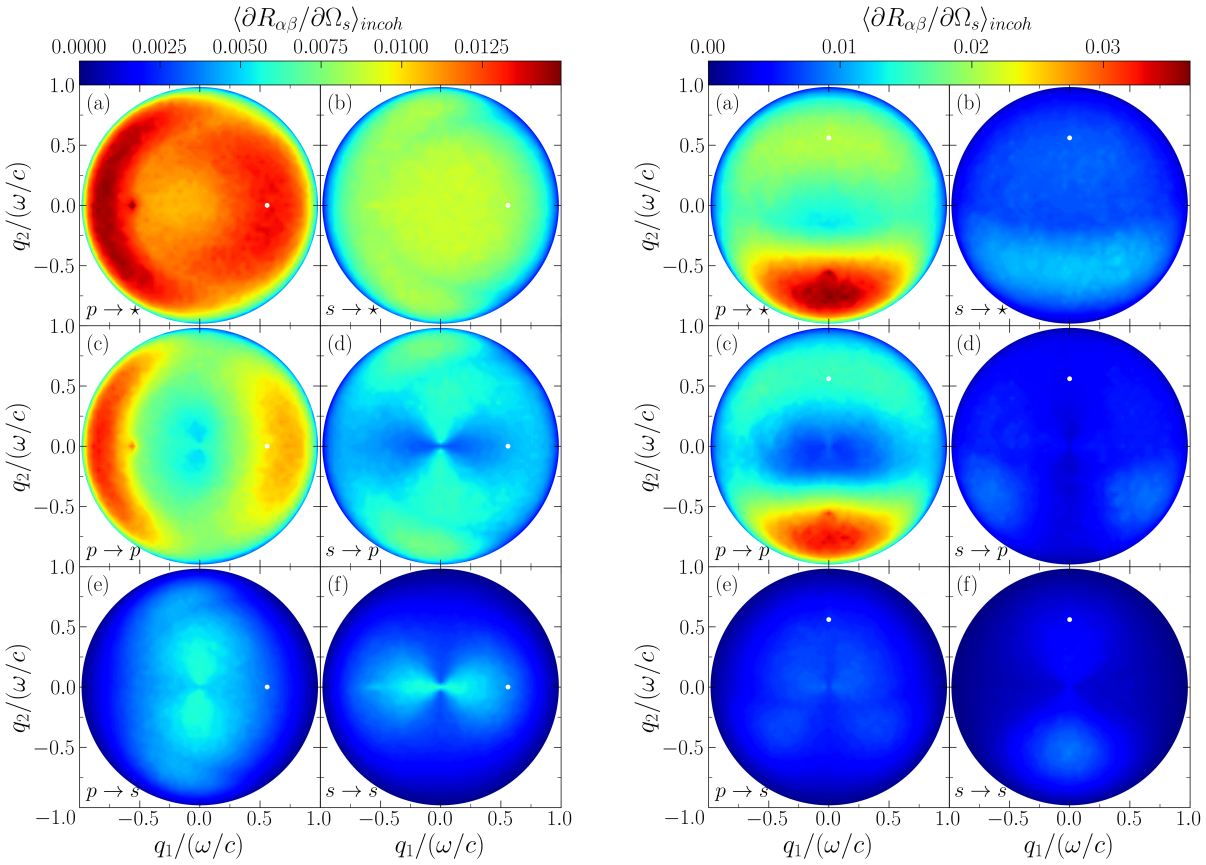

(a) $\phi_0 = 0°$ (b) $\phi_0 = 90°$

Figure 33: The same as in Fig. 32, except for $\theta_0 = 34.05°$.

When the light is incident in the q_2q_3-plane ($\phi_0 = 90.0°$), where the correlation length was doubled, the similarities to the isotropic results are still present. For normal incidence seen in Fig. 32(b), the distributions are very similar to the ones obtained for $\phi_0 = 0°$, except for that some of the distributions have more noise and the result for p and s-polarized incident appear to be very similar to the ones for s and p-polarized incident light when $\phi_0 = 0°$, respectively. If the surface was isotropic the contour plots would be identical, except for a 90° rotation of the plane of incidence. Therefore, this is considered to be a direct effect of the anisotropy.

For non-normal incidence seen in 33(b), the results are very similar to the isotropic case, except for the rotated plane of incidence. It is observed that the strongest contribution to the scattering comes from co-polarized $p \to p$ scattering, while all distributions involving s-polarization contribute weakly in comparison. When $\phi_0 = 0°$ the scattering goes from being stronger for s-polarized incident light under normal incidence, to the scattering dominating for p-polarized incident light under non-normal incidence. For $\phi_0 = 90°$ this change is not observed and the angular distributions are the strongest for p-polarized incident light for all polar angles of incidence.

The MDRC of the anisotropic counterpart to System 2, when the light is incident in the q_1q_3-plane, is quite similar to the results for the isotropic surface. For normal incidence,

which can be seen in Fig. 34(a), the distributions still have the angular suppression around the specular direction of scattering. The distributions have a higher intensity for cross-polarized scattered light, compared to the ones for the isotropic surface. Furthermore, the distributions appear to be overall smaller in shape, and are wider in the q_1 direction relative to the q_2 direction.

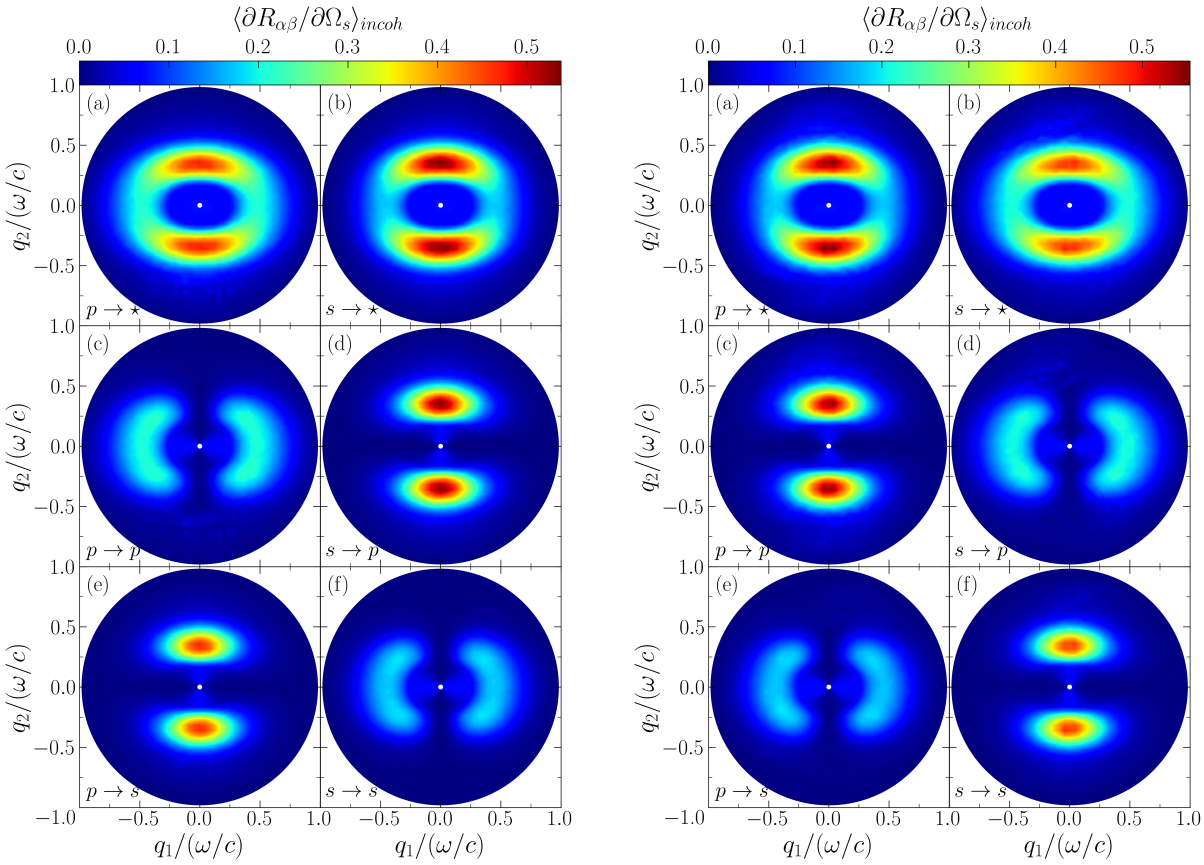

(a) $\phi_0 = 0°$ (b) $\phi_0 = 90°$

Figure 34: The same as in Fig. 32, except that the correlation lengths of the surface are $a_x = \lambda$ and $a_y = 2\lambda$, with $b = a_x/\lambda$; the RMS height is $\delta = \lambda/20$.

For non-normal incidence, displayed in Fig. 35(a), the shape of the distribution is still similar to the isotropic case. The trends observed for normal incidence, such as the near specular suppression and widening along the q_1 axis, are still present, except for the cross-polarized intensity enhancement. When the polarization is not recorded ($\beta \to \star$), the intensity is the highest above and below the specular direction, where for the isotropic case it was located to the left.

When the light is incident in the q_2q_3-plane, see Fig. 34(b), the angular distribution of the incoherent MDRC still has similarities with the isotropic case. For normal incidence the contour plots are identical to the $\phi_0 = 0°$ case, except that the co-polarized distributions appear to have swapped places with the cross-polarized distributions, as observed for anisotropic System 1 in Fig. 32. The surface displays a stronger ability to scatter light along the q_2 direction than the q_1 direction, for both polarizations of the incident light.

For non-normal incidence, seen in Fig. 35(b), the distributions are localized in the forward scattering direction around the specular direction, with the peak of intensity

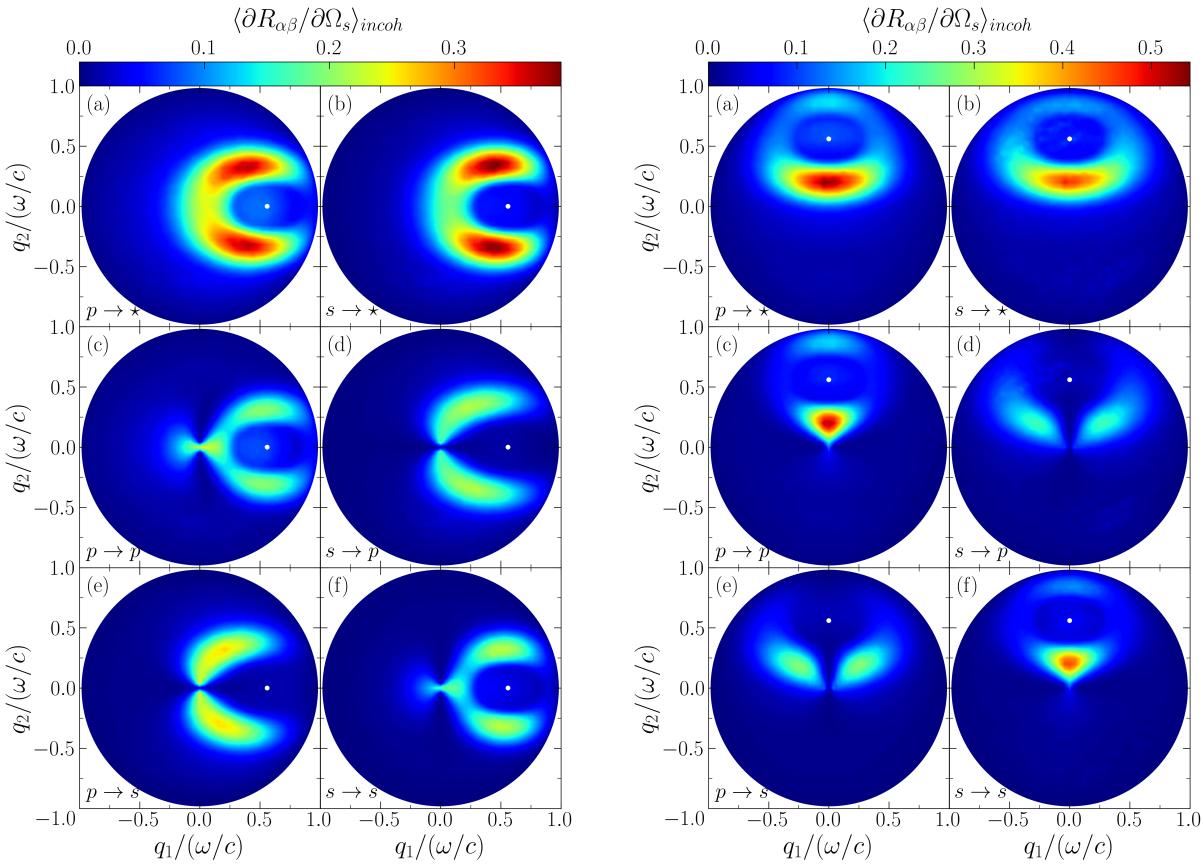

(a) $\phi_0 = 0°$ (b) $\phi_0 = 90°$

Figure 35: The same as in Fig. 34, except for $\theta_0 = 34.05°$.

nearest to the origin. The behavior is very different compared to what was observed when $\phi_0 = 0°$, clearly displaying a change in scattering behavior when the light is incident onto the surface from another azimuthal direction. The regions of the distribution which show the highest intensity of scattered light, are most intense for p-polarized incident light, while the opposite is observed for $\phi_0 = 0°$. This is also observed for normal incidence. There appears to be a slight bias in the scattering intensity towards incident light polarized along the q_2 direction.

5 Summary & conclusion

In this work, the light scattering properties of two-dimensional randomly rough surfaces, were studied through rigorous computer simulations. The approach is non-perturbative and is based on numerically solving the reduced Rayleigh equation for reflection for a given surface. The surfaces studied were characterized by various isotropic or anisotropic power spectra $g(\boldsymbol{q}_{\parallel})$ and complex dielectric functions $\varepsilon_2(\omega)$. The results display the different effects surface roughness can give rise to in the scattering of electromagnetic waves. These effects have been observed in both the intensity distribution and the polarimetric properties of the light scattered from the surfaces.

Simulations were performed for 2D Gaussian-correlated surfaces separating vacuum from glass, with the goal to calculate the reflectance for diffuse illumination. This was achieved by first obtaining the reflectance for directional illumination, multiplying it with a weight function for Lambertian illumination and integrating over all polar angles of incidence. Numerical results for the reflectance of 2D rough glass surfaces under diffuse illumination were presented here for the first time and compared to what has previously been found for 1D surfaces [7]. It was found that depending on the polarization of the incident light and the correlation length of the surfaces, the reflectance can decrease or increase when the degree of surface roughness was systematically increased. In contrast to what was observed for 1D surfaces, it was found that for 2D surfaces the reflectance increased when the correlation lengths were greater than the wavelength of the incident light. Additionally, the reflectance was observed to decrease for s-polarized incident light and increase when the light was p-polarized for correlation lengths less than or equal to the wavelength. Moreover, the dependence of the reflectance on the surface roughness was found to increase with the correlation length, which was in agreement with what was found for 1D surfaces.

The method used to obtain the scattering results was found to be limited in the range of roughness's the simulations could be performed for. Because of limitations in computational resources, the surface lengths which were possible, only allowed for short correlation lengths to be used in the analysis. The achievable degree of roughness, which the method and software could produce reliable results for, was also restricted. Further research is required, using other methods and approaches, to obtain the diffuse-diffuse reflectance for surfaces defined by more extreme roughness parameters. Additionally, the diffuse-diffuse reflectance should be investigated for more materials, relevant to specific applications.

The mean differential reflection coefficient and the 16 elements of the Mueller matrix were obtained for light incident from vacuum and scattered by silver surfaces characterized by the Gaussian-cosine auto-correlation function. To emphasize the new scattering properties of these surfaces, the same quantities were presented for the Gaussian-correlated glass and silver surfaces to serve as a reference. The scattering patterns were observed to be quite different from the patterns obtained when light is scattered from a Gaussian-correlated surface. The surfaces showed many interesting scattering properties, such as a suppression in near specular scattering and enhancement of p-polarized scattered light. These properties were found to depend strongly on the shape of the Gaussian-power spectrum, which was controlled by several surface parameters, and the presence of surface plasmon polaritons. Simulations were performed for anisotropic Gaussian-cosine surfaces as well, which as expected showed interesting scattering patterns and behaviors which

depended strongly with the azimuthal angle of incidence. The enhanced backscattering peak was observed to be either strongly or weakly present in the different Gaussian-cosine surfaces.

The Gaussian-cosine surfaces which showed a circular suppression of the scattering amplitude around the specular direction, were found to have a high reflectance. These two properties, along with the possibility to adjust the radius of the suppression area, makes Gaussian-cosine correlated surfaces a promising candidates as light trapping interfaces in ultra thin photo voltaic cells. However, to be able to make any conclusive statements, similar studies are required using relevant materials followed by experimental verification.

References

[1] M. Själander, M. Jahre, G. Tufte, and N. Reissmann, *EPIC: An energy-efficient, high-performance GPGPU computing research infrastructure*, 2019. arXiv: 1912.05848 [cs.DC].

[2] I. Simonsen, A. Maradudin, and T. Leskova, "The scattering of electromagnetic waves from two-dimensional randomly rough perfectly conducting surfaces: The full angular intensity distribution," *Physical Review A*, vol. 81, Oct. 2009.

[3] I. Simonsen, "Optics of surface disordered systems. a random walk through rough surface scattering phenomena," *European Physical Journal Special Topics*, vol. 181, pp. 1–103, Jun. 2010.

[4] T. A. Leskova, P. A. Letnes, A. A. Maradudin, T. Nordam, and I. Simonsen, "The scattering of light from two-dimensional randomly rough surfaces," in *Optical Complex Systems: OCS11*, G. Berginc, Ed., International Society for Optics and Photonics, vol. 8172, SPIE, 2011, pp. 63–82.

[5] A. R. Mcgurn and A. A. Maradudin, "Perturbation theory results for the diffuse scattering of light from two-dimensional randomly rough metal surfaces," *Waves in Random Media*, vol. 6, no. 3, pp. 251–267, 1996.

[6] T. Nordam, P. Letnes, and I. Simonsen, "Numerical simulations of scattering of light from two-dimensional surfaces using the reduced rayleigh equation," *Frontiers in Physics*, vol. 1, Apr. 2012.

[7] A. Gonzalez-Alcalde, E. Méndez, E. Terán, F. Cuppo, J. A. Olivares, and A. García-Valenzuela, "Reflection of diffuse light from dielectric one-dimensional rough surfaces," *Journal of the Optical Society of America A*, vol. 33, p. 373, Mar. 2016.

[8] V. P. Simonsen, D. Bedeaux, and I. Simonsen, "Non-parametric reconstruction of the statistical properties of penetrable, isotropic randomly rough surfaces from in-plane, co-polarized light scattering data: Application to computer generated and experimental scattering data," 2021. arXiv: 2105.02745 [physics.optics].

[9] G. Rasigni, F. Varnier, M. Rasigni, J. P. Palmari, and A. Llebaria, "Autocovariance functions for polished optical surfaces," *Journal of the Optical Society of America*, vol. 73, p. 222, 2 1983.

[10] J. L. Saunderson, "Calculation of the color of pigmented plastics," *Journal of the Optical Society of America*, vol. 32, p. 727, 12 1942.

[11] P. Kowalczewski, A. Bozzola, M. Liscidini, and L. Claudio Andreani, "Light trapping and electrical transport in thin-film solar cells with randomly rough textures," *Journal of Applied Physics*, vol. 115, p. 194 504, 19 2014.

[12] D. J. Griffiths, *Introduction to Electrodynamics*, 4th ed. Pearson Education, 2012, ch. 9.

[13] J. D. Jackson, *Classical electrodynamics*, 3rd ed. Wiley, 1999.

[14] P. L. Pedrotti F.L., *Introduction to Optics*, 2nd ed. Prentice Hall, 1993.

[15] J. W. Goodman, *Statistical Optics*, Wiley classics library ed, ser. Wiley classics library. Wiley, 2000, pp. 39–40.

[16] I. Simonsen, A. Larsen, E. Andreassen, E. Ommundsen, and K. Nord-Varhaug, "Haze of surface random systems: An approximate analytic approach," *Physical Review A*, vol. 79, Apr. 2009.

[17] M. Zamani, F. Shafiei, S. Fazeli, M. Downer, and G. Jafari, "Analytic height correlation function of rough surfaces derived from light scattering," *Physical Review E*, vol. 94, Jul. 2015.

[18] E. Parzen, *Stochastic processes*, ser. Classics in applied mathematics 24. Society for Industrial and Applied Mathematics, 1999, pp. 71–74.

[19] A. G. Voronovich, *"Rayleigh hypothesis," in Light Scattering and Nanoscale Surface Roughness*, 1st ed., ser. Nanostructure Science and Technology. Springer US, 2007, pp. 93–106.

[20] J. W. Strutt, "On the dynamical theory of gratings," *Proceedings of the Royal Society of London. Series A, Containing Papers of a Mathematical and Physical Character*, vol. 79, no. 532, pp. 399–416, 1907.

[21] R. F. Millar, "On the rayleigh assumption in scattering by a periodic surface," *Mathematical Proceedings of the Cambridge Philosophical Society*, vol. 65, no. 3, pp. 773–791, 1969.

[22] T. Nordam, P. A. Letnes, and I. Simonsen, "Validity of the rayleigh hypothesis for two-dimensional randomly rough metal surfaces," *Journal of Physics: Conference Series*, vol. 454, p. 012 033, Aug. 2013.

[23] D. Pattanayak and E. Wolf, "General form and a new interpretation of the ewald-oseen extinction theorem," *Optics Communications*, vol. 6, no. 3, pp. 217–220, 1972.

[24] G. Brown, V. Celli, M. Haller, and A. Marvin, "Vector theory of light scattering from a rough surface: Unitary and reciprocal expansions," *Surface Science*, vol. 136, no. 2, pp. 381–397, 1984.

[25] Ø. S. Hetland, A. A. Maradudin, T. Nordam, P. A. Letnes, and I. Simonsen, "Numerical studies of the transmission of light through a two-dimensional randomly rough interface," *Phys. Rev. A*, vol. 95, p. 043 808, 4 Apr. 2017.

[26] N. C. Bruce, "Calculations of the mueller matrix for scattering of light from two-dimensional surfaces," *Waves in Random Media*, vol. 8, pp. 15–28, 1 1998.

[27] D. S. Flynn and C. Alexander, "Polarized surface scattering expressed in terms of a bidirectional reflectance distribution function matrix," *Optical Engineering*, vol. 34, no. 6, pp. 1646–1650, 1995.

[28] V. F. E. K. A. Maradudin, "Coherent scattering enhancement in systems bounded by rough surfaces," *Physics Reports*, vol. 288, pp. 127–204, 1-6 1997.

[29] A. Madrazo and A. Maradudin, "Numerical solutions of the reduced rayleigh equation for the scattering of electromagnetic waves from rough dielectric films on perfectly conducting substrates," *Optics Communications*, vol. 134, no. 1, pp. 251–263, 1997.

[30] I. Simonsen and A. A. Maradudin, "Numerical simulation of electromagnetic wave scattering from planar dielectric films deposited on rough perfectly conducting substrates," *Optics Communications*, vol. 162, no. 1, pp. 99–111, 1999.

[31] P. W.H., T. S.A., V. W.T., and F. B.P., *Numerical recipes in C: the art of scientific computing*, 2nd ed. Cambridge University Press, 1997, pp. 500–504.

[32] T. Sauer, *Numerical Analysis*, 3rd ed. Pearson, 2017, ch. 2.4, pp. 99–106.

[33] R. W. Johnson P. B.; Christy, "Optical constants of the noble metals," *Physical Review B*, vol. 6, pp. 4370–4379, 12 1972.

[34] A. R. McGurn, A. A. Maradudin, and V. Celli, "Localization effects in the scattering of light from a randomly rough grating," *Phys. Rev. B*, vol. 31, pp. 4866–4871, 8 Apr. 1985.

[35] K. A. O'Donnell and E. R. Mendez, "Experimental study of scattering from characterized random surfaces," *J. Opt. Soc. Am. A*, vol. 4, no. 7, pp. 1194–1205, Jul. 1987.

[36] H. Arwin, *Thin Film Optics and Polarized Light*, Edition 6, the viridis edition. Hans Arwin, 2016, pp. 94–96.

[37] C. R. and H. A., "Construction of fully symmetric cubature formulae of degree 4k-3 for fully symmetric planar regions," no. Report TW 71, 1985.

[38] J. Walsh, "The reflection factor of a polished glass surface for diffused light," *Illum. Res. Tech. Pap.*, vol. 2, p. 10, 1926.

[39] P. D. G. K. (auth.), *Reflectance Spectroscopy: Principles, Methods, Applications*, 1st ed. Springer-Verlag Berlin Heidelberg, 1969, p. 12.

[40] "The optimum addition of points to quadrature formulae," *Math. Comp.*, vol. 22, pp. 847–856, 1968.

[41] A. G. Voronovich, "The kirchhoff and related approximations," in *Light Scattering and Nanoscale Surface Roughness*, A. A. Maradudin, Ed. Springer US, 2007, pp. 35–60.

[42] T. Aho, M. Guina, F. Elsehrawy, F. Cappelluti, M. Raappana, A. Tukiainen, A. B. M. K. Alam, I. Vartiainen, M. Kuittinen, and T. Niemi, "Comparison of metal/polymer back reflectors with half-sphere, blazed, and pyramid gratings for light trapping in iii-v solar cells," *Optics Express*, vol. 26, A331, 6 2018.

A The arctan2(y, x) function and the angular distribution of the $M'(\theta)$ matrix

The arctan $2(y, x)$ function is defined as

$$\text{arctan2}(y,x) = \begin{cases} \arctan\left(\frac{y}{x}\right) & \text{if } x > 0 \\ \arctan\left(\frac{y}{x}\right) + \pi & \text{if } x < 0 \text{ and } y \geq 0, \\ \arctan\left(\frac{y}{x}\right) - \pi & \text{if } x < 0 \text{ and } y < 0, \\ +\frac{\pi}{2} & \text{if } x = 0 \text{ and } y > 0, \\ -\frac{\pi}{2} & \text{if } x = 0 \text{ and } y < 0, \\ \text{undefined} & \text{if } x = 0 \text{ and } y = 0. \end{cases} \tag{108}$$

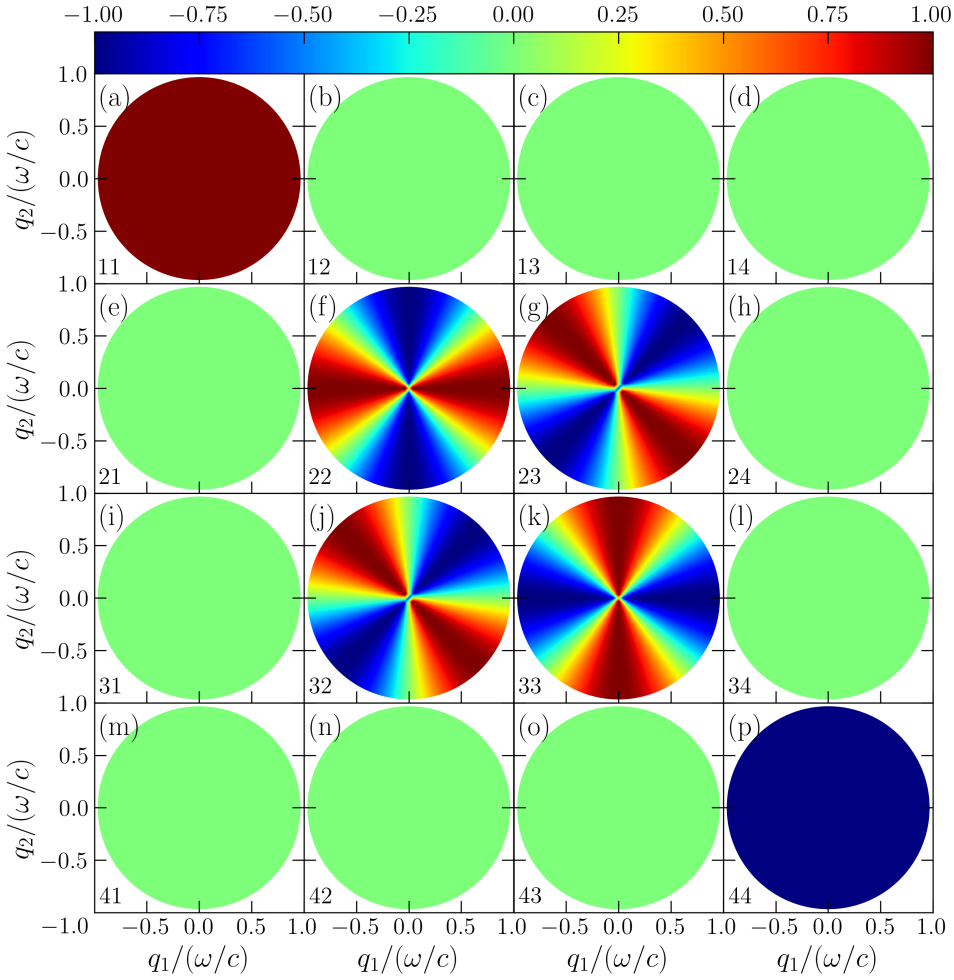

Figure 36: A plot of the Mueller matrix given by Eq. (105) as a function of q_1 and q_2. The calculation was performed by using $\theta = \text{arctan2}(q_2, q_1)$, where arctan2$(y, x)$ is given by Eq. (108).

B The reflectance of a moderately rough surface

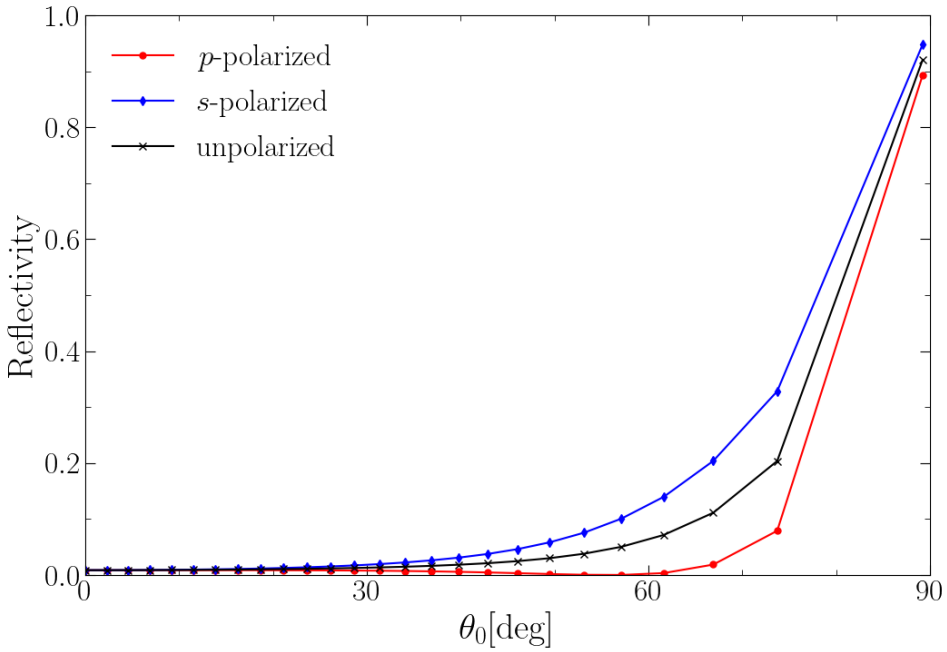

Figure 37: The reflectivity (62) for a randomly rough vacuum-glass interface under directional plane wave illumination as a function of the polar angle of incidence. The surface was characterized by a Gaussian power spectrum with the correlation length $a = 2\lambda$, where $\lambda = 0.6328\,\mu\text{m}$ is the wavelength of the incident light. The RMS height of the surface was $\delta = \lambda/10$. The refractive index of glass was assumed to be $n = 1.5$ for this wavelength. The reflectance was calculated from simulation results averaged over an ensemble of 500 surface realizations. Each surface realizations was limited to an area of $25\lambda \times 25\lambda$ and discretized onto a grid of 321×321 points. The energy was found to be conserved within 1%.

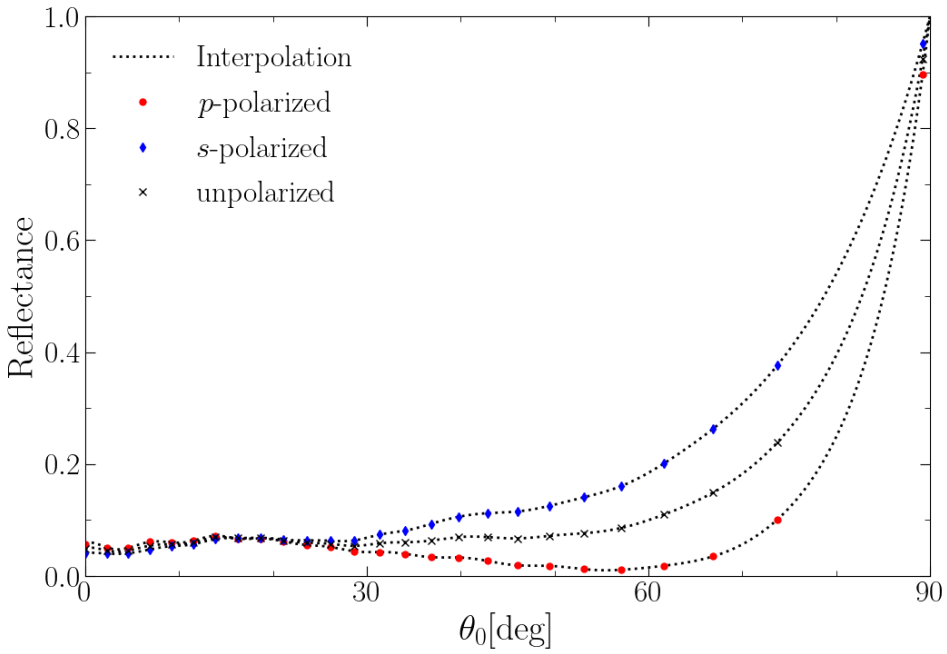

Figure 38: The reflectance (62) for a randomly rough vacuum-glass interface under directional plane wave illumination as a function of the polar angle of incidence. The parameters were the same as for Fig. 37.

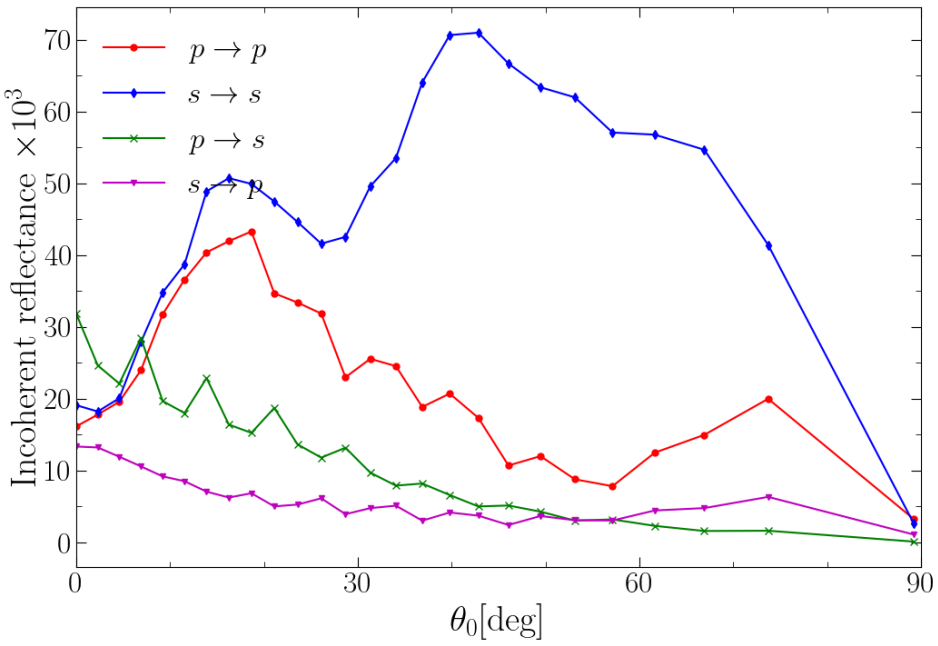

Figure 39: The incoherent component of the reflectance (62) for a randomly rough vacuum-glass interface under directional plane wave illumination as a function of the polar angle of incidence. The parameters were the same as for Fig. 37.

C The MDRC of a Gaussian-cosine correlated glass surface

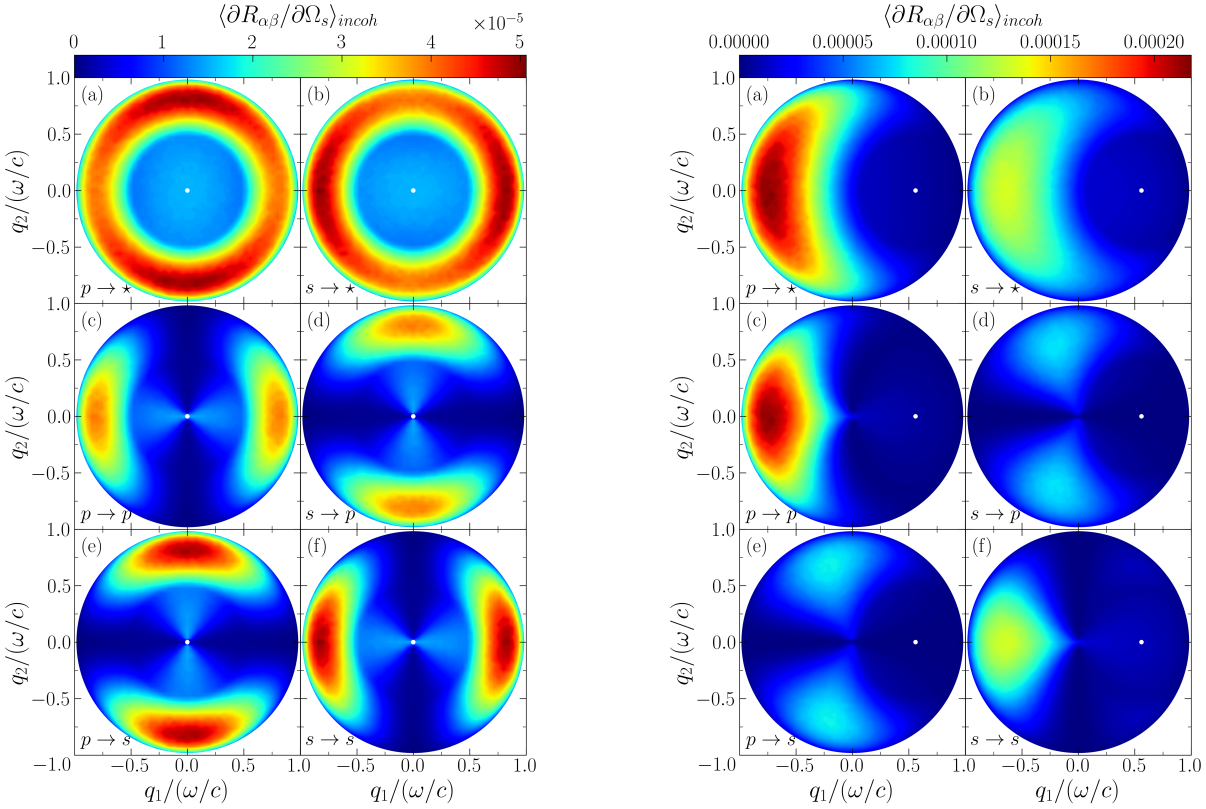

(a) $\theta_0 = 0.0°$ (b) $\theta_0 = 34.05°$

Figure 40: The full angular distribution of the incoherent component of the MDRC (42) for light scattering from a randomly rough interface separating vacuum and glass as a function of the lateral wave vector $\boldsymbol{q}_{\parallel}$. The polar angle of incidence was in panel (a) $\theta_0 = 0.0°$; in panel (b) $\theta_0 = 34.05°$. The surface was characterized by an isotropic Gaussian-cosine correlation function with the correlation length $a = \lambda/4$, with $b = a/2$; the RMS height was $\delta = \lambda/40$. The wavelength of the incident light was $\lambda = 0.6328\,\mu\text{m}$, and the refractive index of glass at this wavelength was assumed to be $n = 1.5$ at this wavelength. The surfaces realizations used in the simulations were spatially limited to the quadratic area $25\lambda \times 25\lambda$, and discretized on a grid of 321×321 points. The results were averaged over an ensemble of 7269 surface realization.